X-RAY–HEATED CORONAE AND WINDS FROM ACCRETION DISKS: TIME-DEPENDENT TWO-DIMENSIONAL HYDRODYNAMICS WITH ADAPTIVE MESH REFINEMENT

D. TOD WOODS,[1,2,3] RICHARD I. KLEIN,[3,4] JOHN I. CASTOR,[1] CHRISTOPHER F. MCKEE,[3,5]
AND JOHN B. BELL[6]

ABSTRACT

We perform for the first time time-dependent, two-dimensional, axisymmetric hydrodynamic simulations using local adaptive mesh refinement of thermally driven rotating winds from X-ray–irradiated accretion disks. The disk is assumed to flare in height with radius allowing direct exposure from the central X-ray source. The heating and cooling are treated strictly in the optically thin approximation. We adopt two spectra characteristic of active galactic nuclei (AGNs) which have Compton temperatures of $T_{\rm IC} \approx 1.3 \times 10^7$ K and 10^8 K. We have computed a number of models which cover a large range in luminosity ($0.002 \leq L/L_{\rm Eddington} \leq 1$) and radius ($\lesssim 20$ Compton radii).

Our models enable us to extend and improve on the analytic predictions of Begelman, McKee, & Shields (BMS) for Compton-heated winds by including non-Compton processes such as photoionization heating and line cooling, typical of X-ray–heated winds. These non-Compton processes can be dominant at low temperatures ($\lesssim 10^7$ K), thus being important in the wind regions of AGNs. Our results agree well with a number of predictions given by BMS, even when non-Compton processes dominate, suggesting that their analytic approximations of the hydrodynamics of disk winds are applicable to the more general area of X-ray–heated winds. In the regime in which Compton processes dominate (i.e., $T_{\rm IC} = 10^8$ K spectrum), we have used our results to improve the analytic predictions of BMS, providing a new expression for the mass-loss rate and a modified view of the wind solution topology.

We find that beginning from a basically static state, the time-dependent flow which develops eventually settles into a *steady* wind, without any evidence of hydrodynamic instabilities. The solution topology consists of a corona with an exponentially truncated wind at small radii, and a vigorous wind at large radii which can be impeded by gravity for small luminosities. We have constructed radius-luminosity parameter space plots of our numerical results in analogy to BMS for both the high and low $T_{\rm IC}$ cases, depicting the range of solutions. The plots are strikingly similar to the analytic predictions, especially for high $T_{\rm IC}$. We find the radial extent of the corona to be independent of luminosity, as predicted by BMS, extending out to about $0.25 R_{\rm IC}$; this is a direct consequence of Compton heating. The transition from an isothermal to nonisothermal corona occurs at a luminosity within about a factor of 2 of the critical luminosity ($L_{\rm cr} \approx 0.03 T_{\rm IC8}^{-1/2} L_{\rm E}$) predicted by BMS. The mass flux density in the corona shows an exponential rise, peaking at around $0.2 R_{\rm IC}$ nearly independent of luminosity. The wind solutions can be characterized mainly by steadily heated, free winds (region B in BMS) and gravity-inhibited winds (region C in BMS). Nearly isothermal winds with temperatures of the order $T_{\rm IC}$ also exist (region A in BMS) but require higher luminosities than was first estimated by BMS. A necessary condition for the winds to approach isothermality is that the luminosity exceed the critical luminosity.

The change in wind solutions from regions B and C is characterized by a nearly discontinuous change in the sonic point location from large heights in region C to small heights in region B. The mass-loss rate, however, appears continuous across this boundary. For a streamline leaving the disk surface at a radius R_0, the sonic point distance along the streamline, $s_{\rm sonic}$, is such that $s_{\rm sonic}/R_0 \approx 0.6$ in region B and $s_{\rm sonic}/R_0 \gg 1$ in region C.

An unexpected conclusion from our numerical results is that the area of a flow tube can actually be smaller at the sonic point than at the disk surface. This is because of the presence of an unbalanced radial pressure gradient of the flow at low heights upon being heated. Incorporating this effect into the simple analytical formulae for the mass-loss rate given by BMS yields results which are typically within about a factor of 2 (3) of our numerical results over a wide range of luminosities and radii for the high (low) Compton temperature models.

We provide fitting formulae of our numerical results which give the mass flux density as a function of radius and luminosity. We also discuss briefly the implications of our results for the prediction of Fe Kα lines which have recently been observed in AGNs.

Subject headings: accretion, accretion disks — galaxies: active — hydrodynamics — stars: coronae —
X-rays: galaxies — X-rays: stars

[1] Lawrence Livermore National Laboratory, L-15, P.O. Box 808, Livermore, CA 94550; tod@eaglevail.llnl.gov, castor1@llnl.gov.
[2] Space Sciences Laboratory, University of California, Berkeley, CA 94720.
[3] Department of Astronomy, 601 Campbell Hall, Univeristy of California, Berkeley, CA 94720; klein@radhydro.berkeley.edu, cmckee@mckee.berkeley.edu.
[4] Lawrence Livermore National Laboratory, L-23, P.O. Box 808, Livermore, CA 94550.
[5] Department of Physics, University of California, Berkeley, CA 94720.
[6] Lawrence Livermore National Laboratory, L-316, P.O. Box 808, Livermore, CA 94550.

1. INTRODUCTION

Accretion disks are thought to exist in a variety of systems ranging from stellar mass type objects such as in X-ray binaries, cataclysmic variables (CVs), and protostars, to active galactic nuclei (AGNs) with a supermassive black hole of the order of 10^8–10^9 $M_\odot$. The collapse of material onto a compact object produces X-rays which can then irradiate and heat the accretion disk (assuming the disk flares with radius; Shakura & Sunyaev 1973), which can lead to the existence of a corona and/or wind. Simply put, the X-ray illumination results in a gradual rise in temperature with height where photoionization heating is balanced primarily by collisional losses and recombination. Depending on the details of the spectrum, this may continue up to a critical temperature ($T_{c,\max}$) above which the equilibrium becomes thermally unstable; at this point, the temperature rises quickly to the Compton temperature (T_{IC}), where there is a balance between heating from Compton scattering and inverse Compton cooling (e.g., Krolik, McKee, & Tarter 1981). If the coronal temperature attained is large in comparison with the escape temperature from the disk, we can expect a vigorous wind to form.

The effects of X-ray heating on the structure of accretion disks is a subject of increasing popularity given the desire to accurately predict spectra from these disks and their surrounding corona and/or wind. This is necessary in order to determine whether the observed emission lines can be explained through X-ray illumination, or whether some other heating mechanism, such as viscosity (e.g., Shaviv & Wehrse 1986; Czerny & King 1989a, b), is necessary. Much of the theory of Compton-heated coronae and winds for accretion disks has been worked out in Belgelman, McKee, & Shields (1983, hereafter BMS) and Begelman & McKee (1983). More recently, detailed models of the vertical structure of X-ray–irradiated accretion disks have been developed for X-ray binaries (e.g., Hubeny 1990; Tuchman, Mineshige, & Wheeler 1990; Ko & Kallman 1991; Raymond 1993) and AGNs (Collin-Souffrin 1987; Collin-Souffrin & Dumont 1990; Dumont & Collin-Souffrin 1990a, b; Mobasher & Raine 1990; Shimura & Takahara 1993). Typically, treatment of this inherently two-dimensional problem is reduced to one dimension by solving the vertical structure on cylinders at different radii, thus ignoring the effects of radiative transfer in the corona. The effects of scattering from the corona have been discussed by Begelman & McKee (1983). Ostriker, McKee, & Klein (1991) have calculated the flux incident at the base of the corona for an isothermal Compton-heated corona above an accretion disk in the single-scattering limit, while Murray et al. (1994) have solved the same problem using a two-dimensional flux-limited radiative diffusion technique. Vrtilek, Soker, & Raymond (1993) have performed two-dimensional Monte Carlo simulations for the radiative transfer to predict the iron K-shell feature for X-ray binaries.

The modeling of winds from accretion disks is still somewhat in its infancy. The modeling has followed one of two paths, one-dimensional analyses which presuppose a flow geometry, and, more recently, fully two-dimensional calculations. BMS assume a flow geometry based on simple physical arguments and parameterize it in such a way to allow a comprehensive analytic treatment given the simple form of the heating and cooling. The result was a prediction

of the mass flux density coming off the disk as a function of luminosity and radius which they found to be relatively insensitive to the details of the assumed flow geometry; that is, the mass flux density is rather robust. Czerny & King (1989a) have made estimates of the mass-loss rate when an α model for the viscosity is extended up into the wind region, but their analysis was more approximate than that of BMS. Fukue (1989) and Takahara, Rosner, & Kusunose (1989) considered the behavior of polytropic winds from accretion disks for a prescribed flow geometry. Vitello & Shlosman (1988, 1993) and Shlosman & Vitello (1993) have considered the effects of winds in CVs. Given the lower temperature of these winds, thermal driving is insufficient to accelerate the winds to observed velocities. As such, the work of Vitello & Shlosman focuses on radiation pressure–driven winds from line absorption of the continuum from the region near the compact central object. Again, the treatment is reduced to a one-dimensional treatment by presupposing a geometry of the outflowing wind.

Although two- and three-dimensional simulations of accretion disks have been performed for a number of years, usually looking at the question of stability (e.g., Eggum, Coroniti, & Katz 1987; Sawada, Matsuda, & Hachisu 1986a, b, 1987; Kaisig 1989a, b; Kley 1989, 1991; Kley & Lin 1992), little attention has been paid to the multidimensional modeling of the wind until recently (Melia, Zylstra, & Fryxell 1991; Melia & Zylstra 1992; Balsara & Krolik 1993). Melia et al. have concentrated on modeling the inner region (i.e., $r \leq 5 \times 10^8$ cm) of low-mass X-ray binaries. These calculations couple the equations of hydrodynamics and flux-limited radiative diffusion, and they show considerable time variability which the authors then try to relate to observed X-ray bursts. However, this work suffers from the use of an unrealistic boundary condition at the disk interface, resulting in material being injected at highly supersonic velocities (∼Mach 30) at small radii where one would normally expect the flow to be very subsonic (Basko et al. 1977; London & Flannery 1982; BMS; Tavani & London 1993) owing to gravitational deceleration (see § 6.2). The consequences of such highly supersonic inflow are physically unrealistic solutions. Balsara & Krolik (1993) have focused on the problem of predicting the wind from a torus surrounding a supermassive black hole in an AGN. The torus model is based upon a compilation of observations, the most compelling of which is the determination that the nuclear region of some Seyfert 2 galaxies has a spectrum similar to a Seyfert 1 when viewed in its polarized light (Antonucci & Miller 1985; Miller & Goodrich 1990). The work of Balsara & Krolik focuses on predicting the structure of the wind produced from direct illumination of the inner face of the torus at 1 pc from the central object in the unphysical limit when the material has no angular momentum. As such, this work is not directly comparable to our models because of the differences in assumed geometry and dynamics.

In this work we calculate, for what we believe to be the first time, the two-dimensional structure of a thermally driven wind from an accretion disk heated by X-rays from a central source. There are several important features to our simulations. First of all, we include part of the disk in the calculation so that we may provide the correct boundary condition. Melia et al. (as well as Balsara & Krolik 1993) do not include any of the disk (or torus) in the computational domain; instead they treat it as a boundary condition for

which they *specify* the velocity normal to the boundary. In both cases, the prescribed inflow is supersonic. Thus, although their solution procedure is valid, their solutions are dependent upon their assumed injection velocity. Instead, we adopt the usual stellar wind condition that the lower boundary is in the subsonic region so that the normal velocity at the boundary is determined by the interior wind solution. The result is that our boundary condition will not affect our solution. Another important feature of our calculations is that we include a full array of heating and cooling mechanisms thought to be important in the photosphere and corona of an illuminated disk. That is, we include not only the high-temperature mechanisms (i.e., Compton heating and cooling, bremsstrahlung), but also the processes (i.e., photoionization heating, collisional and recombination cooling) necessary to provide the stable equilibrium at low temperatures ($\sim$few $\times 10^4$ K). We emphasize, however, that the heating and cooling are calculated in the optically thin limit. We discuss this limitation in greater detail in § 6.3. Finally, our hydrodynamics incorporates local adaptive mesh refinement (AMR; Berger & Colella 1989, Klein, McKee, & Colella 1990, 1994, also see Appendix A1). This procedure allows us to dynamically rezone those regions which require the highest spatial resolution. This is important not only at small radii where quantities are changing rapidly, but also along the disk interface where the density can change by orders of magnitude in going from the disk temperature to the coronal temperature.

Our goal in this work is to understand the types of wind solutions available for different luminosities and Compton temperatures. Our models allow us not only to compare with the analytic treatment of BMS, but also to extend it to temperatures and radii for which BMS is not valid. As such, the disks in our models extend out to large radii (possibly larger than what may exist in observed systems), so that we may identify the full range of wind solutions and be able to compare them to BMS (who also determined the solutions out to arbitrarily large radii). Another reason for comparing our results with BMS is to allow us to understand to what degree the approximations used therein can be applied to the wider range of problems in astrophysical gasdynamics. We do not attempt to model precisely any individual object in this work. Such a quantitative comparison between theory and observation will be dealt with in a later paper (Murray et al. 1995).

The outline of this paper is as follows: in § 2 we present the model equations solved, as well as a discussion of the heating and cooling mechanisms included. The numerical method is described in § 3 along with the geometrical setup of the problem and the boundary and initial conditions. In § 4 we review briefly some of the highlights of the theory developed by BMS. The results, as well as a comparison with BMS, are described in § 5. A discussion of the effects of spatial resolution, as well as the validity of the optically thin approximation and the implications for Fe Kα lines, is given in § 6. Our conclusions are summarized in § 7.

2. MODEL EQUATIONS

2.1. *Conservation Equations*

In this paper we model the two-dimensional evolution of a wind from an accretion disk surrounding a compact central object (e.g., a black hole, neutron star, etc.) in the plane perpendicular to the disk, assuming rotational sym-

metry. The wind is thermally driven by the X-ray heating from the central source due to the gravitational capture of accretion disk material by the central object. The length scale of the disk on which we model the wind is much larger than the radius of the central object or the event horizon of the black hole,[7] so the luminosity emanating from the central object will simply be a parameter to our problem. The mass of the central object is also a parameter, but it can be eliminated when producing a dimensionless form of the equations (§ 2.3). The conservation equations for mass, momentum, and energy in vector form are simply

$$\frac{\partial \rho}{\partial t} + \nabla \cdot (\rho v) = 0 , \qquad (2.1)$$

$$\frac{\partial}{\partial t}(\rho v) + \nabla \cdot (\rho v v) + \nabla p = \rho g , \qquad (2.2)$$

$$\frac{\partial}{\partial t}(\rho \epsilon') + \nabla \cdot [(\rho \epsilon' + p)v] = \rho v \cdot g + H , \qquad (2.3)$$

where ρ is the total mass density, $v = (v_R, v_Z, v_\phi)$ is the velocity, p is the total gas pressure, and $\rho \epsilon'$ is the sum of internal $p/(\gamma - 1)$ and flow $\frac{1}{2}\rho v^2$ energy densities. The net heating rate per unit volume is H, and because of our optically thin approximation, it is strictly a local function. We neglect the gravity from the disk and wind, so that the gravitational acceleration can be given by the gradient of a scalar potential, $g = -\nabla \Phi$, which is stationary in time. Thus, the energy equation (2.3) can be rewritten as

$$\frac{\partial}{\partial t}(\rho \epsilon) + \nabla \cdot [(\rho \epsilon + p)v] = H , \qquad (2.3a)$$

where

$$\rho \epsilon = \tfrac{3}{2}p + \tfrac{1}{2}\rho v^2 + \rho \Phi \qquad (2.3b)$$

is now the total energy density, and we have assumed that the gas has an adiabatic index $\gamma = 5/3$.

2.2. *Heating and Cooling*

The regions of interest in our simulations are nearly fully ionized so that the equation of state $p = \rho k T/\mu$ is applicable, with the mean mass per particle $\mu \approx 0.61 m_H$. The net heating rate per unit volume, $H(\rho, T, F)$, is computed using G. Ferland's photoionization code CLOUDY (Ferland 1991). CLOUDY is a multipurpose code designed to handle photoionized plasmas in optically thick media (using escape probabilities). However, we utilize it in the optically thin, low-density regime to compute the total heating $n^2\Gamma(\Xi, T)$ and cooling $n^2\Lambda(\Xi, T)$ rate per unit volume, where $\Xi = F/cp$ is the pressure ionization parameter, F is the radiative flux, and c is the speed of light. Included in the total heating is Compton scattering and photoionization heating of all the ionization stages of hydrogen, helium, and several trace metals (the most important of which are C, N, O, Si, S, and Fe). The total cooling includes collisional excitation of the most important lines from all the species listed above, as well as recombination cooling, Compton cooling, collisional ionization cooling, and free-free losses. The gas is assumed to be free of dust.

---

[7] In fact, the compact object producing the X-rays is actually located outside our computational domain. See § 3.

TABLE 1

CONTINUUM SPECTRA[a]

v_i (ryd)[b]	SPECTRUM 1		SPECTRUM 2	
	$\log(f_{0i})$	s_i	$\log(f_{0i})$	s_i
1.00 (−5)......	−3.388	+2.5	−3.388	+2.5
9.12 (−3)......	4.0115	−1.00	4.0115	−1.00
0.206...........	2.6576	−0.50	2.6576	−0.50
1.743...........	2.194	−1.00	2.194	−1.00
4.130...........	1.819	−3.00	1.819	−3.00
26.84...........	−0.6192	−0.70	−0.6192	−0.19
7.35 (+3)......	−2.326	−1.67	−1.080	−2.08
7.40 (+6)......	−7.34	...	−7.34	...

[a] $L_v = L f_{0i}(v/v_i)^{s_i}$.
[b] $a(b) = a \times 10^b$.

We have chosen two spectra for our models which yield Compton temperatures of the order 10^7 and 10^8 K. These spectra are given as piecewise-continuous power laws with luminosity $L_v = L f_{0i}(v/v_i)^{s_i}$, where L is the total luminosity, v_i ($i = 1, \ldots, N$) are the frequency intervals of the different power-law (s_i) fits, and the f_{0i} values are defined so that the luminosity per frequency interval is continuous and $L = \int_{v_1}^{v_N} L_v \, dv$. The broken power-law fits are shown in Table 1. Spectrum 1 is CLOUDY's standard AGN spectrum. It is similar to that described by Mathews & Ferland (1987), with the exception that there is a submillimeter break at 10 μm below which (in frequency) the spectrum has a power law indicative of self-absorbed synchrotron emission (i.e., $+2.5$; Rybicki & Lightman 1979). This spectrum yields a Compton temperature,

$$T_{IC} \equiv \frac{1}{4kL} \int_{v_1}^{v_N} hvL_v \, dv \, , \qquad (2.4)$$

of $T_{IC} \approx 1.3 \times 10^7$ K. Equation (2.4) is inaccurate for photon energies above $m_e c^2$, but this is only a small correction for the adopted spectrum. We note that even though this spectrum is based upon observations of AGNs, it may not be appropriate to attribute the entire spectrum to the central source. Spectrum 2 in Table 1 is basically the same as spectrum 1, only the slope between 26.8 ryd and 7350 ryd has been reduced (arbitrarily) to provide a larger number of high-energy photons. The Compton temperature for this spectrum is 1.0×10^8 K.

In Figure 1 the relative contributions of the heating (Γ) and cooling (Λ) are plotted as a function of temperature for several values of the ionization parameter Ξ for spectrum 1. Figure 2 shows the thermal equilibrium curve for the two spectra. At low temperatures, there is near balance between photoionization heating and cooling due to line excitation and recombination. At large temperatures, the equilibrium arises from a balance of Compton heating and cooling. The solutions with positive slope, i.e., $dT/d\Xi > 0$, are thermally stable, whereas those with negative slope are thermally unstable. Following the notation of BMS, we label the critical ionization parameter $\Xi_{c,max}$ ($\Xi_{h,min}$) to be the maximum (minimum) ionization parameter in the cold (hot) phase for which a stable equilibrium can exist. For these particular spectra, there is also a small range of ionization parameters ($\Xi_1 \leq \Xi \leq \Xi_2$) for which there exist stable solutions at intermediate temperatures ($T \sim 10^6$ K). This state can cause slight problems for the adaptive mesh refinement (see Appendix).
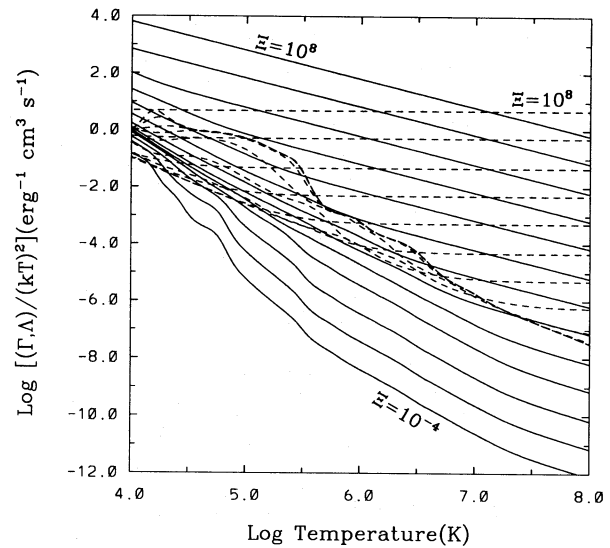

FIG. 1.—Log of the heating ($\Gamma/[kT]^2$; *solid curve*) and cooling ($\Lambda/[kT]^2$; *dashed curve*) functions as a function of temperature for different ionization parameters ($\Xi = F/cp$). Each curve represents a decade in ionization parameter. The results were obtained from CLOUDY in the optically thin, low-density limit.

2.3. Dimensionless Form of the Equations

BMS showed that the steady state wind equations can be written in a dimensionless form which eliminates the mass of the central object as a parameter. With some care, we can also accomplish this for the time-dependent equations. We define a length scale, the Compton radius (R_{IC}), to be the distance at which the escape velocity equals the isothermal sound speed at the Compton temperature, i.e.,

$$R_{IC} \equiv \frac{G_0 M_c \mu}{k T_{IC}} = \frac{9.8 \times 10^{17}}{T_{IC8}} M_{c8} \text{ cm} \, , \qquad (2.5)$$

where M_{c8} is the mass of the central object in units of 10^8 $M_\odot$, and $T_{IC8} = T_{IC}/10^8$. The velocity is scaled by the Keplerian rotation velocity at the Compton radius, so

$$v_C \equiv (G_0 M_c/R_{IC})^{1/2} = 1.165 \times 10^3 T_{IC8}^{1/2} \text{ km s}^{-1} \, , \qquad (2.6)$$

where the second equality arises from the use of equation (2.5). (We have used the subscript "IC" for the Compton temperature and radius to be consistent with BMS, but for the remaining characteristic Compton parameters we simply use the subscript "C.") The timescale can then be defined as

$$t_C \equiv R_{IC}/v_C = 8.4 \times 10^9 T_{IC8}^{-3/2} M_{c8} \text{ s} \, , \qquad (2.7)$$

so that $2\pi t_C$ is the rotation period at the Compton radius. Alternatively, t_C can be thought of as the time it takes to traverse R_{IC} traveling at the isothermal sound speed for $T = T_{IC}$. A characteristic pressure can be defined as the pressure at the Compton radius which a gas in thermal equilibrium would have at its maximum temperature in the cool stable phase. Thus, we write

$$p_C \equiv \frac{L/(4\pi R_{IC}^2)}{c \Xi_{c,max}} = 1.1 \times 10^{-3} \frac{L}{L_E} M_{c8}^{-1} T_{IC8}^2 \left(\frac{\Xi_{c,max}}{40}\right)^{-1}$$

$$\times \text{ ergs cm}^{-3} \, , \qquad (2.8)$$

where the Eddington luminosity is

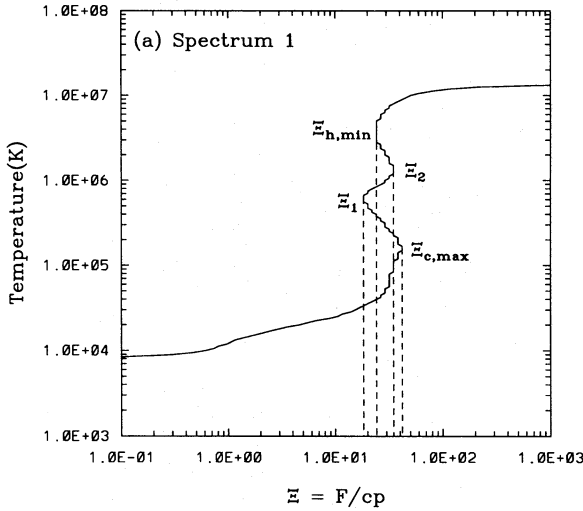$$L_E = 1.5 \times 10^{46} M_{c8} \text{ ergs s}^{-1} \, . \qquad (2.9)$$
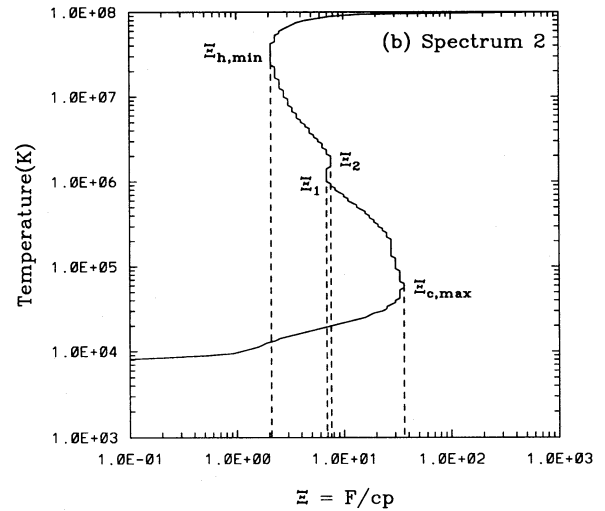
FIG. 2.—(a) Thermal equilibrium curve for spectrum 1 in Table 1 which has a Compton temperature of 1.33×10^7 K. $\Xi_{c,max}$ is the maximum ionization parameter in the cool stable phase; $\Xi_{h,min}$ is the minimum ionization parameter in the hot stable phase. There is an intermediate temperature solution around $T \approx 10^6$ K for which a stable equilibrium can also exist ($\Xi_1 \leq \Xi \leq \Xi_2$). (b) Same as (a), except that spectrum 2 in Table 1 is used which has a Compton temperature of 10^8 K.

Given the pressure, we can define a density from the equation of state

$$\rho_C \equiv \frac{\mu p_C}{k T_{IC}} = 8.1 \times 10^{-20} \frac{L}{L_E} M_{c8}^{-1} T_{IC8} \left(\frac{\Xi_{c,max}}{40}\right)^{-1}$$
$$\times \text{ g cm}^{-3} . \quad (2.10)$$

We can also define a characteristic gravitational potential,

$$\Phi_C \equiv G_0 M_c / R_{IC} = 1.35 \times 10^{16} T_{IC8} \text{ ergs g}^{-1} , \quad (2.11)$$

where G_0 is the gravitational constant. Finally, writing the characteristic heating rate as p_C / t_C, we can define

$$\Gamma_C \equiv \frac{p_C}{t_C (\rho_C/\mu)^2} = 2.1 \times 10^{-23} T_{IC8}^{3/2} \left(\frac{\Xi_{c,max}}{40}\right) \left(\frac{L}{L_E}\right)^{-1}$$
$$\times \text{ ergs cm}^3 \text{ s}^{-1} . \quad (2.12)$$

Using these scaling parameters, we can define the following dimensionless quantities:

$$\rho^* \equiv \frac{\rho}{\rho_C} , \quad (v_R^*, v_Z^*, v_\phi^*) \equiv \frac{(v_R, v_Z, v_\phi)}{v_C} ,$$

$$(R^*, Z^*) \equiv \frac{(R, Z)}{R_{IC}} , \quad t^* \equiv \frac{t}{t_C} , \quad p^* \equiv \frac{p}{p_C} ,$$

$$\Phi^* \equiv \frac{\Phi}{\Phi_C} , \quad \rho^* \epsilon^* \equiv \frac{\rho \epsilon}{p_C} , \quad T^* \equiv \frac{T}{T_{IC}} ,$$

$$\Xi^* \equiv \frac{\Xi}{\Xi_{c,max}} , \quad (\Gamma^*, \Lambda^*) \equiv \frac{(\Gamma, \Lambda)}{\Gamma_C} . \quad (2.13)$$

(In these units, the radial variable ζ used by BMS is R_0^*, where R_0^* is the dimensionless radius at the footpoint of a flow tube.) Given these definitions, we can write the conservation equations (eqs. [2.1], [2.2], [2.3a]–[2.3b]) in cylindrical geometry, assuming axisymmetry, as

$$\frac{\partial \rho^*}{\partial t^*} + \frac{1}{R^*} \frac{\partial}{\partial R^*} (R^* \rho^* v_R^*) + \frac{\partial}{\partial Z^*} (\rho^* v_Z^*) = 0 , \quad (2.14)$$

$$\frac{\partial}{\partial t^*} (\rho^* v_R^*) + \frac{1}{R^*} \frac{\partial}{\partial R^*} (R^* \rho^* v_R^{*2})$$
$$+ \frac{\partial}{\partial Z^*} (\rho^* v_R^* v_Z^*) + \frac{\partial p^*}{\partial R^*} = \frac{\rho^* v_\phi^{*2}}{R^*} - \rho^* \frac{\partial \Phi^*}{\partial R^*} , \quad (2.15)$$

$$\frac{\partial}{\partial t^*} (\rho^* v_Z^*) + \frac{1}{R^*} \frac{\partial}{\partial R^*} (R^* \rho^* v_R^* v_Z^*)$$
$$+ \frac{\partial}{\partial Z^*} (\rho^* v_Z^{*2}) + \frac{\partial p^*}{\partial Z^*} = -\rho^* \frac{\partial \Phi^*}{\partial Z^*} , \quad (2.16)$$

$$\frac{\partial}{\partial t^*} (\rho^* v_\phi^*) + \frac{1}{R^*} \frac{\partial}{\partial R^*} (R^* \rho^* v_R^* v_\phi^*)$$
$$+ \frac{\partial}{\partial Z^*} (\rho^* v_\phi^* v_Z^*) = \frac{-\rho^* v_R^*, v_\phi^*}{R^*} , \quad (2.17)$$

$$\frac{\partial}{\partial t^*} (\rho^* \epsilon^*) + \frac{1}{R^*} \frac{\partial}{\partial R^*} (R^* \rho^* \epsilon^* v_R^*)$$
$$+ \frac{\partial}{\partial Z^*} (\rho^* \epsilon^* v_Z^*) + \frac{1}{R^*} \frac{\partial}{\partial R^*} (R^* p^* v_R^*) + \frac{\partial}{\partial Z^*} (p^* v_Z^*)$$
$$= \rho^{*2} [\Gamma^*(\Xi^*, T^*) - \Lambda^*(\Xi^*, T^*)] , \quad (2.18)$$

where

$$\epsilon^* = \frac{3}{2} \frac{p^*}{\rho^*} + \frac{1}{2} (v_R^{*2} + v_Z^{*2} + v_\phi^{*2}) + \Phi^* , \quad (2.19)$$

and the equation of state is now

$$p^* = \rho^* T^* . \quad (2.20)$$

In deriving these equations, we have made use of the definition of t_C (eq. [2.7]) and the relations $p_C/\rho_C v_C^2 = 1 = \Phi_C/v_C^2$. Equations (2.14)–(2.20) do not explicitly involve the compact object mass M_c, provided the functions Φ^*, Γ^*, and Λ^* are also independent of M_c. The heating/cooling functions Γ and Λ are pretabulated functions of Ξ and T.

Therefore, Γ^* and Λ^* are independent of M_c since Γ_C (eq. [2.12]) is independent of M_c, and $\Xi_{c,\mathrm{max}}$ and T_{IC} are parameters determined by the shape of the spectrum. Finally, the gravitational potential has the modified form

$$\Phi^* = \{R^{*2} + [Z^* + Z^*_{\mathrm{disk}}(R^*)]^2 + R^{*2}_{\mathrm{sp}}\}^{-1/2}, \quad (2.21)$$

where R^*_{sp} is a softening radius of the potential in units of the Compton radius, and $Z^*_{\mathrm{disk}}(R^*)$ is a vertical offset (in units of R_{IC}) which is a function of radius. The necessity for and description of these two terms is given in § 3. The important point is that equation (2.21) is also independent of M_c. Therefore, once a spectrum has been selected, there is only one free parameter, namely, L/L_E (see also BMS). Consequently, our discussion will focus on the behavior of our wind solutions as a function of luminosity.

3. PROBLEM SETUP AND COMPUTATIONAL METHOD

We begin by defining our computational domain. Our calculations are performed in $R-Z$ geometry, with the Z-axis coincident with the rotation axis; however, the R-axis is *not* coincident with the disk midplane. We take the R-axis to represent a surface approximately one-half a pressure scale height below the disk/corona interface. Thus, there is an offset as a function of radius, $Z_{\mathrm{disk}}(R)$, which gives the height of our R-axis above the disk midplane. A schematic representation of this is shown in Figure 3. There are several reasons for adopting this offset. First of all, we do not wish to model the entire disk given the uncertainties of the physics (i.e., viscosity) associated with α disk models, and given the need to include radiative transfer effects. Second, it was desirable to remove the origin from the computational domain because of its singular nature in providing the radiative flux and gravitational attraction for our model. Finally, even with the advantage of adaptive mesh refinement (see below and Appendix) and the softening radius on the gravitational potential (eq. [2.21]), it was necessary to drop the disk out of the computational domain at small radii to avoid having to resolve small gravitational scale heights in the cool disk. Therefore, we have adopted an offset which is approximately the height of an α disk model (Shakura & Sunyaev 1973):

$$\frac{Z_{\mathrm{disk}}(R)}{R_{IC}} = \begin{cases} 0.02(R/R_{IC})^{1.125} & R \geq R_{\mathrm{hot}}, \\ 0.02(R_{\mathrm{hot}}/R_{IC})^{1.125} & R \leq R_{\mathrm{hot}}. \end{cases} \quad (3.1)$$
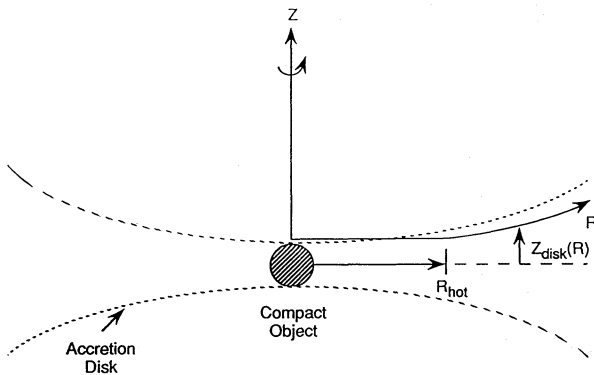

FIG. 3.—Schematic diagram depicting the computational domain (R- and Z-axes) in real space. $Z_{\mathrm{disk}}(R)$ gives the offset of the R-axis of the computational domain from the disk midplane. The R-axis for $R > R_{\mathrm{hot}}$ is prescribed as being one-half of a pressure scale height below the disk surface. Diagram is not to scale.

Inside R_{hot}, the offset is constant and the cool disk material can drop out of the computational domain; only hot coronal material is found at $R < R_{\mathrm{hot}}$. Typically, we take $R_{\mathrm{hot}} \leq R_{\mathrm{sp}}$. Our computational domain in real space is not orthogonal (Fig. 3), but we approximate it as such in the computational domain because the offset represented by the alpha disk is small. The offset is used in only two places in the calculations: (1) computation of the gravitational potential (eq. [2.21]) and (2) computation of the radiative flux used in the heating and cooling. Given the small magnitude of the offset, it tends to have a minimal effect in calculating the gravitational potential because typically $Z_{\mathrm{disk}}(R) \ll \mathrm{max}(R_{\mathrm{sp}}, R)$. The offset at small radii is at most the size of a computational cell in our most highly resolved calculations. Therefore, it will affect the computation of the radiative flux in only a few zones near the origin.

We solve equations (2.14)–(2.21) using a two-dimensional second-order Godunov method based on the method of Colella & Woodward (1984). To this two-dimensional hydro scheme, we have added the effects of rotation, gravity, and heating and cooling represented by the terms on the right-hand side of equations (2.15)–(2.18). We have devoted considerable time and energy in the pursuit of an acceptable means of including these terms in a Godunov method. We give in the Appendix a brief summary of the algorithm of the hydrodynamics and our conclusions for including the source terms, as well as a description of some test problems to which it has been applied. Our hydrodynamics is supplemented by local adaptive mesh refinement (Berger & Colella 1989; Klein et al. 1994), which allows us to select and refine an arbitrary region of the computational domain. By tying in the generation of refined grids with an automatic estimate of the local truncation error, we can obtain the desired resolution at the necessary locations in space and time. Consequently, the number of unnecessary cells, and therefore the computer memory and time requirements, can be kept to a minimum. Even still, it was not uncommon for a highly resolved calculation to take over 100 hr of CPU time on a Cray YMP.

The boundary conditions (BCs) are as follows. The Z-axis (rotation axis) is treated as a line of symmetry. That is, the scalar (ρ and $\rho\epsilon$) and tangential vector (ρv_Z) quantities are continuous at the boundary, while the vector quantities normal to the rotation axis (ρv_R and ρv_ϕ) go to zero at the boundary. The goal for the outer surface (i.e., top and right-hand) BCs is that they have as little effect on the interior solution as possible. In general, we take these BCs as free flowing, i.e., all the quantities are continuous across the boundary. Such simple BCs will be acceptable provided the flow is supersonic before passing through the boundary, since the interior solution will be independent of the BCs because the $v - c_s$ characteristic speed is positive, i.e., the characteristics transmit information only out of the grid (here c_s is the adiabatic sound speed). Thus, in choosing our computational grid it is necessary to include a large enough domain to guarantee that the velocities have become supersonic before reaching the outer boundaries. Implementation of these BCs shows that they work well with two caveats. The first caveat is that our calculations start from a static state (except for rotation), so the BCs are not valid until the wind has developed. This seems to pose a problem only for low-luminosity models in which a significant amount of matter may enter from the outer boundaries. Consequently, we extrapolate BCs which preserve steady momentum con-
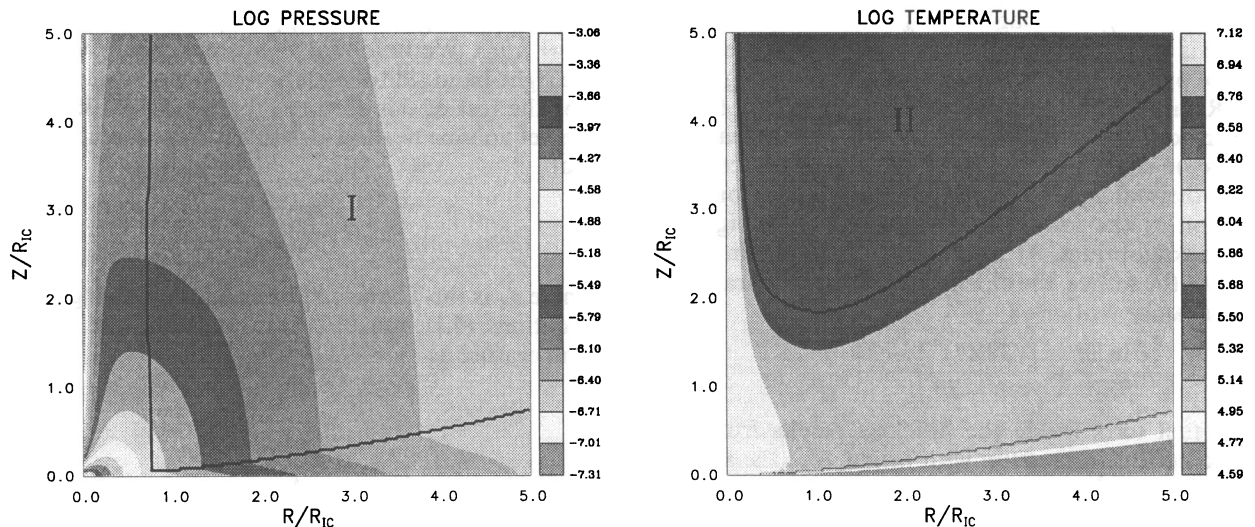
FIG. 4.—Initial pressure and temperature configuration. In region I, radial momentum balance is not satisfied initially. In region II, thermal equilibrium dictates that the temperature should drop back down to the cool phase. However, we have artificially set the temperature in this region to be $T_{h,\min}$ to start. See text for further details.

servation normal to the boundaries using the nearest interior solution. This procedure prevents the inflow from gravitational attraction and appears to provide a smooth transition to flow-dominated regimes as the wind forms. The second caveat is that even after the development of the wind, the flow exiting the right-hand boundary is not supersonic at low heights. Therefore, we must be mindful of the fact that the solution at large radii and low heights may be affected by our outer BCs. Indeed, we sometimes see some fluctuation in this region (see § 5). However, we find the effects to propagate inward only minimally. Also, we can assess the influence of the boundary conditions by comparing the results to a problem calculated on a larger domain. In general, we find the results to be similar, so that the effect of the BCs appears to be minimal.

Finally, as stated above, the R-axis is treated as a surface located one-half of a pressure scale height below the disk/corona interface (except for radii inside R_{hot}). The BCs are presumed to be appropriate for vertical subsonic inflow. That is, we specify all but the normal momentum component (ρv_Z). We define the disk/corona or disk/wind interface to be the surface on which $\Xi^* = \Xi/\Xi_{c,\max} = 1$.[8] Therefore, the thermal pressure along the bottom boundary can be specified by $p^*(R^*, Z^* = 0) = \exp (0.5)/[R^{*2} + Z^{*2}_{\mathrm{disk}}(R^*)]$. The temperature along the boundary is obtained by solving the thermal equilibrium equations with an ionization parameter $\Xi^* = \exp (-0.5)$. The density is obtained from the equation of state, and the radial velocity is set to zero. The rotational velocity is determined by requiring radial momentum balance, i.e., the centrifugal force along the R-axis is computed from the difference between the inward gravitational attraction and the

outward pressure gradient. Inside the disk, this results in the rotational velocity being nearly Keplerian because the pressure gradient is small owing to the low temperature of the disk. Finally, the Z component of the momentum at the boundary is extrapolated from the solution in the computational domain. Note that we are allowed to extrapolate one boundary condition in the case of subsonic inflow because there is one characteristic ($v - c_s$) that is directed from the computational domain back onto the boundary. This extrapolation is essential to guarantee that the solution we obtain is not a result of the velocity BC. If we had placed our boundary above the disk interface, our assumptions of thermal equilibrium and subsonic inflow at the boundary would be less certain.[9] This procedure is different from previous investigations (e.g., Melia et al. 1991; Balsara & Krolik 1993) in which the material is injected at supersonic velocities. As such, their wind solutions are determined by the prescription of the inflow velocity boundary condition, rather than being a natural consequence of the computed solution (see § 6.2).

The initial condition for our calculations is that the gas is static (except for rotation) and in thermal equilibrium. We assume in our calculations that the disk spans the computational grid in radius. That is, we do not consider the case in which the disk is truncated at a given radius. Such models are considered by Murray et al. (1995). Our procedure for calculating the initial state is to set $v_{R,Z} = 0$ and integrate the vertical (Z-direction) hydrostatic and thermal equilibrium equations together simultaneously, starting from the base. Once this is performed for the entire grid, we can then calculate the radial pressure gradient from centered finite difference expressions and thus solve for the rotational velocity satisfying radial momentum balance. There are two exceptions to this procedure. The first is that it can be impossible for the corona to be in radial momentum balance with $v_R = 0$ if the gas is in the thermal equilibrium. That is, for $R^* \gtrsim 1$ the outward pressure gradient in the corona can be larger than the inward gravitational attrac-

---

[8] In reality, this is not true for the disk/corona interface. Begelman & McKee (1990) and McKee & Begelman (1990) have shown that in the corona, where winds are weak, thermal conduction dictates that $\Xi_{h,\min}$ may be the more appropriate ionization parameter. For spectrum 1, there is little difference between $\Xi_{c,\max}$ and $\Xi_{h,\min}$, so this effect should be minimal. The effect is more pronounced for spectrum 2. This deficiency can be eliminated by including thermal conduction, but this is beyond the scope of our paper. In the wind region, however, the temperature gradient is often small enough that thermal conduction is relatively unimportant, and our assumption that the surface of the disk is at $\Xi_{c,\max}$ is valid.

[9] This is not a problem inside R_{hot} where, although the boundary material is coronal, the velocities are decidedly subsonic and structure is nearly hydrostatic.

tion, thus requiring an imaginary v_ϕ. An example of this initial state is shown in Figure 4, (*left panel*), where we show contours of pressure for the case of $L/L_E = 0.1$ using spectrum 1. Region I outlines the domain in which the R momentum equation cannot be satisfied. In this domain we set v_ϕ to some small positive value. The second exception deals with thermal equilibrium at high altitudes. Consider the variation of the ionization parameter with height in hydrostatic equilibrium. At heights that are large in comparison with the radius, the change in ionization parameter with height can be written as

$$\frac{\partial \ln \Xi^*}{\partial Z^*} \approx \frac{[(T^* Z^*)^{-1} - 2]}{Z^*} , \qquad (3.2)$$

where the first term inside the brackets results from the hydrostatic decline in pressure with height, and the second term is from the r^{-2} dependence of the optically thin radiative flux. From equation (3.2), we see that when Z^* is large, the ionization parameter can decline with height. If the ionization parameter drops below the minimum value possible in the stable hot phase ($\Xi_{h,min}$), thermal equilibrium dictates that the temperature must drop down to the cold phase. This region of cold material has an upper limit in height because once it drops back to the cold phase, the gravitational scale height becomes smaller, thus enabling the pressure to once again decline faster than the effects of geometrical dilution. This eventually leads back to $\Xi = \Xi_{c,max}$, and thermal equilibrium dictates the temperature should jump back up to coronal temperatures. We have performed simulations with this pocket of cool material at high altitudes (Fig. 4, *right panel*). We find that as the wind starts to form, both Rayleigh-Taylor and Kelvin-Helmholtz instabilities can be induced in and around this pocket. But inevitably this cold material is pushed out of the grid by the wind. This behavior is a transient response to our initial conditions and serves only to slow down the calculations, so we have decided to remove this feature by setting the temperature to $T_{h,min}$ initially.

4. ANALYTIC THEORY OF BMS

We review briefly some of the characteristics of optically thin, Compton-heated winds as described in BMS. In particular, we focus here on the prediction of the mass-loss rate per unit area as a function of radius. We describe also some simple improvements in the theory based upon our numerical results.

As described earlier, the Compton radius defines the radius at which the isothermal sound speed is equal to the escape velocity from the system for material which is heated to the Compton temperature. We define R_0 to be the radius in the disk midplane from which a given streamline arises. We expect that for $\xi \equiv R_0/R_{IC} \ll 1$ there will be a nearly hydrostatic corona with a small mass flux density, while for large radii ($\xi \gtrsim 1$), a vigorous wind may develop.

Let us consider for a moment the behavior in the wind region. The magnitude of the wind will depend on the luminosity, and in particular on the ratio of the heating timescale to gravitational timescale. Because of the finite heating time, one can define a characteristic temperature to which a parcel of gas can be heated in a time required to rise a height R_0 above the disk, namely,

$$k T_{ch} = \frac{H(\rho, T_{ch}, L/4\pi R_0^2)}{(\rho/\mu_e)(c_{ch}/R_0)} , \qquad (4.1)$$

volume heating rate, and $\mu_e \approx 2\mu$ is the mass per electron ($n_e = \rho/\mu_e$). We note that this is an implicit relation, since the right-hand side of equation (4.1) is also a function of T_{ch}. For the rest of this section only, we follow BMS and take the net volume heating rate to be Compton heating only, so that

$$H \approx \frac{\rho}{\mu_e} \frac{k T_{IC} \sigma_T L}{m_e c^2 \pi R_0^2} , \qquad (4.2)$$

where σ_T is the Thomson cross section. Solving for T_{ch} using equations (4.1) and (4.2), we can write the characteristic temperature as

$$\frac{T_{ch}}{T_{IC}} = \left(\frac{L}{L_{cr}}\right)^{2/3} \xi^{-2/3} , \qquad (4.3)$$

where the critical luminosity is

$$L_{cr} \equiv \frac{1}{8} \left(\frac{m_e}{\mu}\right)^{1/2} \left(\frac{m_e c^2}{k T_{IC}}\right)^{1/2} L_E$$
$$\approx 2.88 \times 10^{-2} T_{IC8}^{-1/2} L_E . \qquad (4.4)$$

Note that for spectrum 1, $L_{cr} = 0.080 L_E$. Using this temperature, we can then define a heating timescale

$$t_h \equiv k T_{ch}/(\mu_e H/\rho) = R_0/c_{ch} ; \qquad (4.5)$$

with the normalization introduced in § 2, this corresponds to $t_h^* \equiv t_h/t_C = (L/L_{cr})^{-1/3} \xi^{4/3}$. Similarly, a gravitational timescale can also be defined as

$$t_g \equiv R_0/v_g = R_0^{3/2}/(G_0 M_c)^{1/2} , \qquad (4.6)$$

where $v_g = (GM_c/R_0)^{1/2}$ is the Keplerian velocity at R_0; the normalized value is $t_g^* \equiv t_g/t_C = \xi^{3/2}$. Using these definitions, we can write the ratio of the gravitational timescale to heating timescale as

$$\frac{t_g}{t_h} = \left(\frac{T_{ch}}{T_g}\right)^{1/2} = \left(\frac{L}{L_{cr}}\right)^{1/3} \xi^{1/6} , \qquad (4.7)$$

where the gravitational temperature is $T_g \equiv G_0 M_c \mu/(R_0 k)$. From equation (4.7), we can see that the critical luminosity can be interpreted as being the luminosity required for the heating and gravitational times to be equal for flow emanating from the Compton radius. When heating takes place on a short timescale compared with gravitational deceleration, the wind can heat to escape temperatures quickly without feeling the effects of gravity, and the wind should be vigorous. Similarly, when the gravitational timescale is short compared with the heating timescale, gravity can impede the wind significantly, even at $R_0 > R_{IC}$. We note also that equation (4.3) implies that a wind region exists in which $T_{ch} > T_{IC}$ for $L > L_{cr}$. Clearly this is incorrect because of our neglect of Compton cooling, which will tend to regulate the temperature at T_{IC}. Thus, we can identify another region [i.e., $1 \lesssim \xi \lesssim (L/L_{cr})^2$] for which we expect the heating to be rapid enough that the wind is nearly isothermal at T_{IC}.

We can now identify the various solution regimes as a function of disk radius for different luminosities. Following BMS, these regions have been identified as A–E in Figure 5. The solutions are separated into wind solutions for $R_0 > 0.1 R_{IC}$ and gravitationally bound coronae with weak winds for $R_0 < 0.1 R_{IC}$ independent of luminosity. The transition is independent of luminosity due to the Compton temperature
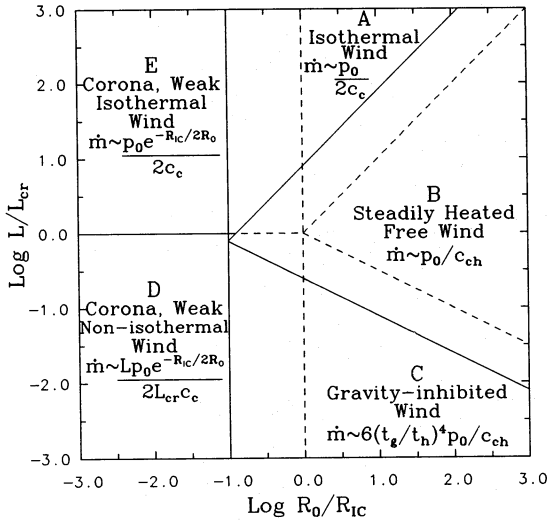
Fig. 5.—Radius-luminosity parameter space plot for the Compton-heated wind theory of BMS. The dashed line represents the theory as presented originally by BMS, while the solid line is a slightly modified form of the theory inspired by our numerical results. Throughout the text, this is the assumed form of the BMS theory. See text for details.

being determined by the hardness of the spectrum and not by the magnitude of the luminosity. We note that the exact locations of the regions in this figure are slightly different from that in BMS (dashed line in Fig. 5), and we discuss the reasons for the modifications shortly. But first, we summarize some of the characteristics of the different regimes, including the mass-loss rate per unit area ($\dot{m} = \rho v$, where v is the velocity along the flow tube). Results that are simply quoted without justification are described in more detail in BMS.

Region A represents the nearly isothermal wind regime in which $T_g \lesssim T_{IC} \lesssim T_{ch}$ for $\xi > 0.1$. In this region, the heating time is short so that $T \approx T_{IC}$ at low heights. The rapid heating also produces large acceleration which results in the flow passing through the isothermal sonic point at low heights. At heights $\sim R_0$, the flow goes through the adiabatic sonic point, and adiabatic losses cause departures from isothermality. Gravity is unimportant in this region, and the pressure at the isothermal sonic point assuming nearly vertical flow is $\approx 0.5 p_0$, where $p_0 \equiv L/(4\pi R_0^2 c \Xi_{c,max})$ is the critical pressure of the cool phase at a radius R_0. Therefore, the mass flux per unit area in this regime is given approximately by $\dot{m} \approx 0.5 p_0/(kT_{IC}/\mu)^{1/2}$, so $\dot{m} \propto R_0^{-2}$.

Region B is a steadily heated, free wind in which $T_g \lesssim T_{ch} \lesssim T_{IC}$ and $\xi > 0.1$. The heating time is still small in comparison with the gravitational time, but the heating is not rapid enough to allow the temperature to reach the Compton temperature. Instead, $T \sim T_{ch}$ at a height $\sim R_0$. The flow passes through the adiabatic sonic point at this height, and the flow pattern has become spherically diverging. In the supersonic regime at larger heights, the flow velocity becomes nearly constant, and the temperature declines inversely with distance due to adiabatic losses. Since the temperature at the sonic point is $\sim T_{ch}$ and the pressure is $\sim p_0$ due to the negligible effect of gravity, the mass flux is estimated to be $\dot{m} \approx p_0/c_{ch}$. From equation (4.3), we see that $T_{ch} \propto R_0^{-2/3}$, so that $\dot{m} \propto R_0^{-5/3}$.

In region C, a gravity-inhibited wind, we have $T_{ch} \lesssim T_g \lesssim T_{IC}$ for $\xi > 0.1$. The heating timescales are now long compared with the gravitational timescales. Gravity

decreases the flow velocity, which allows the gas to be heated over longer times. This results in the temperature $T \sim T_g > T_{ch}$ at a height of $\sim R_0$. (Our numerical results show that in fact the maximum temperature is typically only $\sim 0.1 T_g$.) At these heights, the flow velocity approaches a constant, and it goes through an adiabatic sonic point only at large distances because of the decline in temperature from adiabatic losses. Gravity greatly reduces the pressure at the sonic point so that the mass flux in this region is also greatly reduced; BMS estimate $\dot{m} \approx 6(T_{ch}/T_g)^2 p_0/c_{ch}$. Using equations (4.3) and (4.7), we see that $\dot{m} \propto R_0^{-1}$.

In region D ($\xi < 0.1$ and $L < L_{cr}$), the mass flux in the wind is small because gravity is strong and heating is weak. As in the case of region C, the sonic point occurs at large heights [$\sim (T_g/T_{ch})^3 R_0$], and the resulting mass flux is small due to the exponential decline of the pressure at low heights where the atmosphere is nearly hydrostatic. Under the assumption that the flow is nearly vertical in this inner region, $\dot{m} \approx 0.5(L/L_{cr})[p_0/(kT_{IC}/\mu)^{1/2}] \exp(-0.5\xi^{-1}) \propto R_0^{-2} \exp(-0.5 R_{IC}/R_0)$. (Note that the numerical expressions of BMS assumed a spherically diverging outflow, which is appropriate for a truncated disk. For an infinite disk, such as we consider here, vertical outflow is a better approximation.)

In region E ($\xi < 0.1$ and $L > L_{cr}$), both the heating and gravity are strong. The isothermal sonic point occurs at large heights, but the heating is strong enough to maintain $T \approx T_{IC}$. Assuming the flow is nearly vertical, we find the mass flux density to be $\dot{m} \approx 0.5[p_0/(kT_{IC}/\mu)^{1/2}] \exp(-0.5\xi^{-1})$. Thus, $\dot{m} \propto R_0^{-2} \exp(-0.5 R_{IC}/R_0)$ has the same radial dependence as in region D but differs by the ratio L/L_{cr}. Comparison of this expression with that for region A shows that the wind is strong by the time it reaches $\xi \approx 0.1$. Indeed, Shields et al. (1986) found that $\dot{m}$ peaks near $\xi \simeq 0.15$.

As mentioned earlier, Figure 5 differs from the equivalent figure in BMS (Fig. 1 in BMS). First of all, the corona/wind boundary has been moved in R_{IC} to $0.1 R_{IC}$. The primary reason for doing this is that the analytic expressions for the mass flux density indicate that the wind is strong outside of this radius. In BMS, they noted that their solutions were most uncertain in the range $0.1 R_{IC} \lesssim R_0 \lesssim R_{IC}$. In fact, BMS decided it was best to extrapolate the wind solutions inward from R_{IC} down to $0.1 R_{IC}$. We endorse this policy by moving corona/wind interface to this same location. In addition, the boundaries between the wind regions A, B, and C in Figure 5 are also slightly different from those in BMS. In BMS, the division between regions A and B was defined by $T_{ch} = T_{IC}$, and the division between regions B and C was defined by $t_g = t_h$. Although such a division makes sense on physical grounds, a consequence of these definitions is that the mass flux density is discontinuous at region interfaces. Instead, we define the wind boundaries by requiring that the mass flux density be continuous. The mass flux density for the three wind regions[10] are $\dot{m}_A^* = 0.5(L/L_{cr}/\xi)^{1/3}$, $\dot{m}_B^* = 1$, and $\dot{m}_C^* = 6.4[\xi(L/L_{cr})^2]^{2/3}$, where $\dot{m}^* = \dot{m}/\dot{m}_{ch}$ and $\dot{m}_{ch} = p_0/c_{ch}$. Thus, the A–B boundary is given by $\xi_{AB} = 0.125 L/L_{cr}$, and the B–C boundary is given by $\xi_{BC} = (6.4)^{-3/2}(L/L_{cr})^{-2}$. Notice that a consequence of moving the corona/wind interface to $0.1 R_{IC}$ is that the new

---

[10] In BMS $\dot{m}_B^* \approx 1.2 \pm 0.2$, with uncertainties associated with the position of the sonic point and the flow tube geometry. Based upon our numerical results, we find the lower limit to be more applicable.

A-B and B-C boundaries meet near $L \approx L_{cr}$ at the corona/wind interface, just as in BMS.

There can also be a discontinuity in the mass flux formulae between the coronal region and the wind region. This is because the rates derived by BMS are correct only in the extreme limits of each region. BMS estimate that their formulae are inappropriate in the range $0.1 \lesssim \xi \lesssim 1$. Shields et al. (1986) have produced formulae for the mass flux density which analytically connect the mass flux density between the different regimes. We also provide such a formula given by

$$\dot{m} = \dot{m}_{ch} \left\{ \frac{1 + [(0.125L/L_{cr} + 0.00382)/\xi]^2}{1 + [(L/L_{cr})^4(1 + 262\xi^2)]^{-2}} \right\}^{1/6}$$
$$\times \exp\left\{-[1 - (1 + 0.25\xi^{-2})^{-1/2}]^2/2\xi\right\} . \quad (4.8)$$

This formula provides the correct asymptotic dependence for each of the regions A–E. In the wind regime, equation (4.8) provide rapid transition between the different wind solutions at the interfaces ξ_{AB} and ξ_{BC}, being in error by at most $\approx 10\%$ at these boundaries. As an example, we have plotted in Figure 6 the predicted mass flux density as a function of radius for different luminosities assuming a Compton temperature of 1.3×10^7 K ($L_{cr} = 0.08L_E$) and a mass of the central object of $10^8 M_\odot$. To summarize, then, our expression for the theoretical mass flux density (eq. [4.8]) differs from that of Shields et al. in three respects: (1) since our models focus on disk radii that are much larger than the coronal region, the coronal mass flux density is altered because the flow is nearly columnar rather than spherically diverging; (2) the interfaces between the three wind regions are based on the condition that mass flux density be continuous; and (3) $\dot{m}_B^* = 1.0$ rather than 1.2 (see footnote 10). Throughout this paper, when presenting the results of BMS we use this formula to represent the predicted mass flux density.

Our numerical work generalizes the results of BMS in two important respects: first, we include a full treatment of optically thin X-ray heating and radiative cooling, whereas BMS consider only Compton heating and cooling. Second,

we give a self-consistent treatment of the structure of the upper layer of the disk (in the optically thin approximation), whereas BMS assumed that the disk was geometrically thin. The approximations made by BMS are quite good for the case of high Compton temperature that they focused on ($T_{IC} \sim 10^8$ K), but these approximations restrict significantly the range of validity of the solutions for the softer spectrum characteristic of AGNs ($T_{IC} \approx 1.3 \times 10^7$ K; spectrum 1).

We can estimate the restriction placed on the BMS solutions by their assumption that the heating and cooling are primarily caused by Compton scattering as follows. Inspection of our numerical results for spectrum 1 shows that, as a rule of thumb, Compton processes exceed non-Compton processes for $T \gtrsim 4 \times 10^5$ K. This is not a problem in regions A and E, since Compton processes dominate by definition (so long as $T_{IC} \gg 4 \times 10^5$ K). Next, consider region B, in which BMS estimated that the sonic point occurs at a temperature $T_s \sim (0.16–0.33)T_{ch}$. If we adopt $T_s \sim 0.25T_{ch}$ and require T_s to be several times the 4×10^5 K minimum for Compton heating, we obtain $T_{ch} \gtrsim 4.8 \times 10^6$ K, so that

$$\frac{L}{L_{cr}} \gtrsim 0.22\xi\left(\frac{1.3 \times 10^7}{T_{IC}}\right)^{3/2} \quad \text{(region B)} \quad (4.9)$$

from equation (4.3). Hence, for spectrum 1 ($T_{IC} = 1.3 \times 10^7$ K), much of Region B is not accurately described by the BMS theory. For spectrum 2 ($T_{IC} = 10^8$ K), however, very little of the parameter space we consider here is incompatible with Compton heating and cooling. Finally, we consider regions C and D. Here we find that the temperature is of order $0.1T_g = 0.1T_{IC}/\xi$ at distances $\sim R_0$ from the footpoint. This temperature is at least several times the critical temperature of 4×10^5 K only for $\xi \lesssim 1$ (spectrum 1) or $\xi \lesssim 10$ (spectrum 2). Hence, the analytic theory for region C should be useful only for spectrum 2.

The thin-disk approximation is only marginally valid for spectrum 1. The scale height of an isothermal corona is

$$H_c = \left(\frac{2kTR^3}{GM\mu}\right)^{1/2} = \left(\frac{2T\xi}{T_{IC}}\right)^{1/2} R . \quad (4.10)$$

For spectrum 1, the temperature at the base of the corona is $T_b \approx 1.7 \times 10^5$ K (Fig. 2a), which gives $H_c(T_b)/R \approx 0.16\xi^{1/2}$. Thus, the disk is not very thin even at $R \sim R_{IC}$, and it rapidly becomes thick at larger radii. However, the BMS theory does not rely on the thin-disk approximation in an essential way, so we do not expect the disk thickness to lead to significant errors.

Finally, we wish to note some other approximations made in BMS which, although less significant, may also contribute to a discrepancy between the numerical results and the theory. In order to make the general two-dimensional problem amenable to a one-dimensional analytic theory, BMS parameterized the shape of the flow geometry, as well as its orientation. BMS discussed a range of tube shapes and orientations and found that although certain quantities, such as the location of the sonic point, were sensitive to the details of the geometry, the mass flux density was rather insensitive. (In addition, we note that the flow geometry of our numerical results is not really represented by the parameterization of BMS; see § 5.) Consequently, any comparison with the BMS theory will necessarily focus on the prediction of the mass flux density.
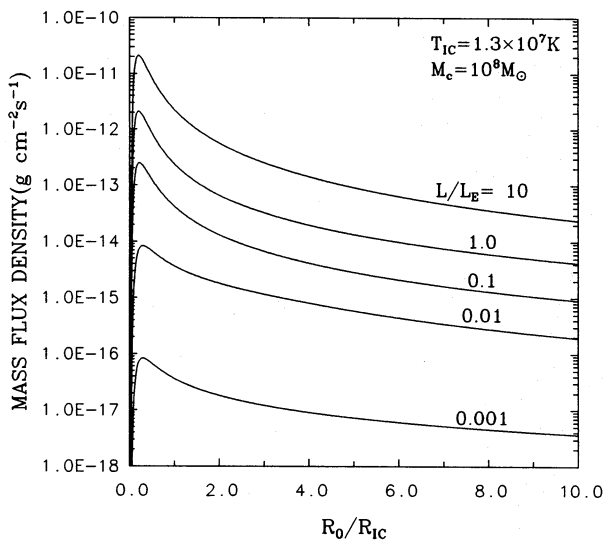

FIG. 6.—Theoretical prediction of the mass flux density from the disk surface as a function of radius (eq. [4.8]) for several different luminosities assuming a Compton temperature of 1.3×10^7 K and a mass of the central object of $M_c = 10^8 M_\odot$.

The predictions in BMS also involved the assumption that the heating time be either much larger (region C) or much smaller (region A, B) than the gravitational timescale. This ratio is a slowly varying function of radius and luminosity (eq. [4.7]). Thus, unless the parameters for our numerical models place them deep within a given region, we may well be sampling the transition from one solution to another, in which case we might not expect good agreement with the theory.

5. NUMERICAL RESULTS

The majority of our calculations have been performed using the standard AGN spectrum 1 with $T_{\rm IC} \approx 1.3 \times 10^7$ K). These models are discussed in § 5.1 and span a luminosity range $0.0025 \le L/L_{\rm E} \le 1$. A smaller set of models has been calculated using the ad hoc spectrum (spectrum 2 with $T_{\rm IC} \approx 10^8$ K). These models are presented in § 5.2 and compared with the lower Compton temperature models and the predictions of BMS.

5.1. $T_{\rm IC} \approx 1.3 \times 10^7$ K Models

5.1.1. Typical Model Result

We describe here a model calculation in which $L/L_{\rm E} = 0.3$ on a $5R_{\rm IC}$ square grid using spectrum 1 in Table 1. Given that $T_{\rm IC} \approx 1.3 \times 10^7$ K, the critical luminosity, $L_{\rm cr} \approx 0.08L_{\rm E}$ (eq. [4.4]), so that $L/L_{\rm cr} \approx 3.8$. From Figure 5, we expect the primary constituent of this model solution to be a heating-dominated wind. We have taken $R_{\rm sp} = 0.1R_{\rm IC} = R_{\rm hot}$ (standard values for our simulations, but see also § 6.1). The calculation was performed on a 200×200 coarse grid with one additional level of refinement by a factor of 4 in each dimension so that the maximum spatial resolution is 160 cells per Compton radius. The refinement is limited mainly to the disk/corona interface and near the rotation axis, since this is where the gradients are largest. In § 6.2 we discuss in greater detail the effects of spatial resolution on our calculations. For now, we regard this resolution to be adequate to identify the important characteristics of our models. Because our hydrodynamics are explicit, the time step in our calculations is controlled by the Courant condition $\Delta t(|v| + c_s)/\Delta X < 1$, where Δt is the time step, ΔX is the spatial resolution, and $v = v_R(v_Z)$ when $X = R(Z)$. The calculation is performed with a Courant number of 0.5 (as are most of our calculations), so that $\Delta t = 0.5\Delta X/(|v| + c_s)_{\rm max}$, where the subscript "max" signifies that we look for the largest signal propagation speed in the grid. There is also time step control associated with heating and cooling (see Appendix). As discussed in § 2, all our calculations are dimensionless. Since we are using an AGN spectrum, for presentation purposes we have converted the numerical results into dimensional form by assuming a mass of the central object of $M_c = 10^8 \, M_\odot$.

We dispense with a detailed discussion of the evolution, instead limiting ourselves to a qualitative description, for two reasons. First and foremost is the fact that our calculations produce, in the end, a wind pattern which is *basically* steady in time. A more precise definition of steadiness is given in § 6.2. Second, given that there is nothing particularly unique about our initial conditions, there seems little reason to describe in detail its evolution to a steady state.

The development of a wind proceeds almost immediately in our simulations. As noted in § 3, the static initial conditions in the corona do not always satisfy radial momentum

(region I of Fig. 4a); this provides an immediate impetus for the wind. The coronal material being accelerated radially draws cooler disk material upward, where it is then heated and accelerated due to the overpressure. The material at large heights (region II of Fig. 4b) begins to cool slowly because it is out of thermal equilibrium. However, this material is eventually pushed out of the grid by the rising material from the disk wind. For the material which leaves the grid at low heights and large radii, the final flow pattern is established rather quickly compared with the time it takes for the entire flow pattern to develop. The flow emanating from near the origin which travels upward along the rotation axis is the last to reach a steady state. This is to be expected, since this material has to overcome the largest gravitational potential in order to escape from the system. Eventually, the simulation tends to a steady state. The time-scale on which this occurs depends on the spatial extent of our grid and the luminosity. For this particular model, the mass flux density coming off the disk surface is within about a factor of 2 of the final result by $t \approx 10t_{\rm C}$, while the overall structure is fairly well established in the wind by $t \approx 25t_{\rm C}$. The results shown have been evolved to $t \approx 65t_{\rm C}$.

Figure 7 shows the steady state total density, total gas pressure, Mach number, and temperature distribution of this simulation. Superimposed on these figures are velocity vectors giving an indication of both the magnitude and direction of the flow. The boxes shown in this figure outline the regions for which we have allowed mesh refinement to take place.[11] The refinement has been confined primarily to the disk/corona interface and along the rotation axis, since it is there that we expect the largest gradients. In the final configuration, the flow leaves the grid supersonically everywhere along the upper boundary, even along the rotation axis (the dark solid line in the Mach number plot indicates the location of the adiabatic Mach surface). Whether or not supersonic flow is achieved along the rotation axis is ultimately governed by the flow geometry. It is well known that the flow geometry must be diverging for a flow, with no external momentum source, to go through an adiabatic sonic point (e.g., BMS). The flow along the rotation axis in our simulations tends to be well collimated; consequently the divergence is weak and the adiabatic sonic point occurs at large height. In general, the flow at large heights tends to a constant velocity. But the Mach number continues to rise with height due to the drop in temperature from adiabatic losses. The most interesting feature is the location of the adiabatic sonic surface ($M \equiv v/c_s = 1$) as a function of radius. Excluding the flow very close to the rotation axis, the bulk of the flow within about $R_0 \lesssim 0.2R_{\rm IC}$ goes super-sonic at a height $\sim R_{\rm IC}$. This behavior was in fact predicted by BMS for the nearly isothermal corona (region E, Fig. 5).

---

[11] Occasionally the contours appear discontinuous at coarse/fine interfaces, especially when the contours are oriented nearly parallel to the interface. Some of this discontinuity is real in the sense that the contour location will be predicted more accurately in the fine cells than in the coarse ones. However, most of the discontinuity is a function of the method of plotting patches. The coarse cells overlying the fine cells are "blacked out"; thus, in plotting the coarse data the contouring routine must extrapolate from the center of the last coarse cell to the interface. If the quantity plotted varies primarily in the direction normal to the surface, this extrapolation is poor, and an apparent discontinuity is seen. If the variation is primarily parallel to the interface, i.e., contours oriented normal to it, then the extrapolation is accurate and the apparent discontinuity is minimized. We thank the referee for bringing this problem to our attention.
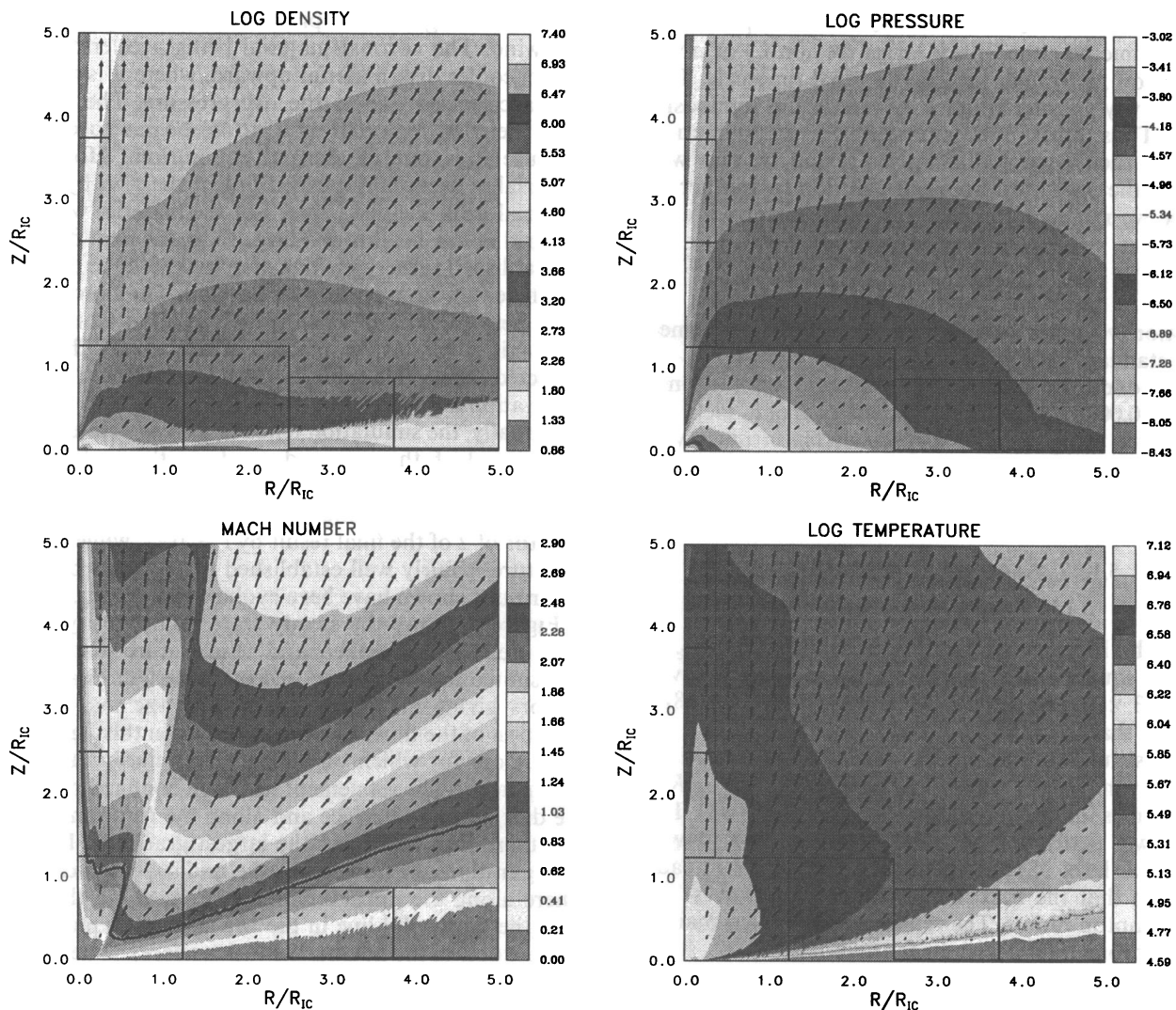
FIG. 7.—Contours of log of total number density (*top left*) log total pressure (*top right*), Mach number ($M = v/c_s$, where $c_s = (\gamma p/\rho)^{1/2}$ is the adiabatic sound speed; *bottom left*), and log temperature (*bottom right*) of the final state of the calculation with $L/L_E = 0.3$ using spectrum 1 in Table 1. The dark line corresponds to the adiabatic sonic surface $M = 1$. Boxes indicate areas in which refinement has taken place. Velocity vectors have been superimposed on all plots.

For $R_0 \gtrsim 0.3R_{IC}$, the flow goes supersonic at a much lower height. The height then increases almost linearly with radius. This distinct change in the solution topology is seen in all our models. As such, it is tempting to associate this near discontinuity in the location of the sonic surface with the transition from a gravitationally bound corona with a weak wind to a vigorous wind. For this particular model, this is justified, but in the lower luminosity models we find such a distinction inappropriate. It is interesting, however, that we see no signature of this discontinuity when looking at the mass flux density, as we will see shortly.

The final pressure distribution has changed significantly from the initial state (Fig. 4a) at large heights due to the effects of flow. The pressure gradient in the final state is now primarily in the Z-direction, whereas initially it was in the R-direction. Also, the minimum pressure along the rotation axis is more than an order of magnitude smaller in the final equilibrium than in the initial state. This is because of a combination of two effects associated with the flow: (1) the final temperature is smaller due to adiabatic losses, thus producing smaller gravitational scale heights; (2) at large heights, where gravity is unimportant, the pressure declines

from conservation of $p + \rho v^2$ as the nearly vertical flow goes supersonic. For $R_0 \gtrsim 0.2R_{IC}$, the final pressure distribution looks similar to the initial state up to a height of $\sim 0.5R_{IC}$ because the flow is very subsonic.

The temperature distribution when the wind develops is vastly different from the initial static state, except near the origin, where the low velocities and rapid heating rates are able to keep the temperature nearly isothermal at approximately the Compton temperature. The flow can cause the transition from disk to corona (i.e., the transition region) to become spatially extended when flow times become comparable to heating times. Also, the adiabatic losses from the flow serve to keep the maximum temperature along a streamline well below the Compton temperature as the wind goes supersonic. For this particular model, the disk interface is typically a discontinuous change in density and temperature. However, at $R_0 \gtrsim 3.5R_{IC}$, the disk interface becomes irregular because of the slowing of the heating rate. At small radii the heating rates are fast and the transition to coronal temperatures takes place over a single cell. Conversely, at very large radii the heating rates are slow and the transition region is spread over many spatial cells (examples

of this will be shown for lower luminosities). It is at intermediate resolution that the disk interface starts to take on this irregular appearance. In addition, the flow from $R_0 \gtrsim 3.5R_{IC}$ also exits the grid subsonically (see Fig. 9). Thus, there could be a possible feedback from the boundary conditions on this part of the flow leading to some instability (Nakagawa & Steinolfson 1976). We have verified this by performing the calculation on a larger grid, and we found similar, but slightly reduced, structure in the disk interface.

Figure 8 shows the velocity vectors for a small region $0.5R_{IC}$ on a side around the origin. The transition between the gravitationally bound corona and wind is apparent near $R_0 \approx 0.2R_{IC}$. It is interesting that there is such a marked division between these two regimes. We find this division to be rather insensitive to R_{sp} and R_{hot} for R_{sp}, $R_{hot} \lesssim 0.1R_{IC}$. Also, once this region is well resolved, we see little movement in this division as a function of spatial resolution. In fact, the division location appears to be insensitive to luminosity for $L/L_E \lesssim 0.1$. Given the rather large velocity shear between the weak coronal wind and the large heating dominated wind, it was not a foregone conclusion that the solution would be hydrodynamically stable to the Kelvin-Helmholtz instability. However, as stated before, our simulations tend to a steady state with no evidence of hydrodynamic instabilities.

In Figure 9 we show the streamlines and adiabatic sonic surface of the final configuration. Also shown in this figure is the location of the disk surface defined by the contour $T = T_{c,max}$. An important feature of the flow geometry is the immediate turning of the streamlines from vertical to radial upon reaching temperatures above $T_{c,max}$. This is a result of the radial pressure gradient becoming important. At disk temperatures, radial force balance involves primarily gravity and rotation. Upon being heated, the pressure gradient becomes large and the flow turns radial and becomes compressed. The pressure at $T_{c,max}$ will go roughly at R^{-2} if the flow velocity is small because it will satisfy the condition $\Xi = F/cp = \Xi_{c,max}$ with the flux going as R^{-2} for our optically thin calculations. The net acceleration due to gravity and centrifugal force is $g_{net} \approx (GM_c/R^2)(1 - y^{-1})$, where $(y - 1)R_0$ is the distance along a streamline (BMS).

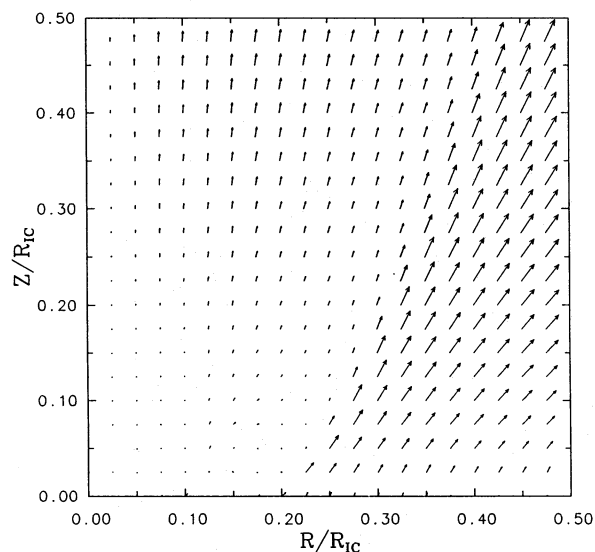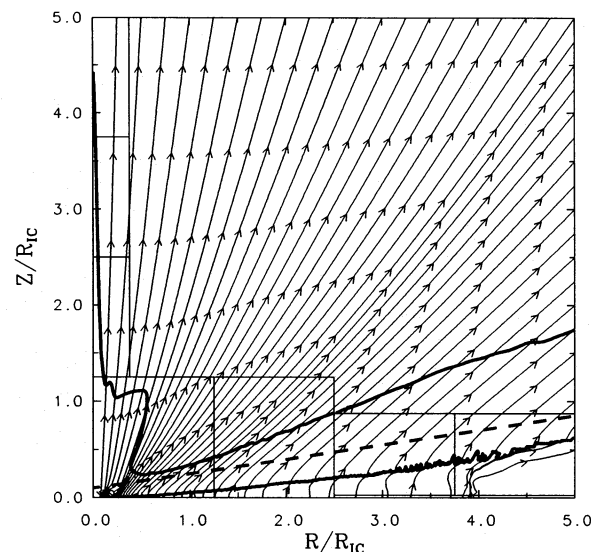FIG. 9.—Streamline plot for the model in Fig. 7. The upper solid line is the adiabatic sonic surface. The dashed line is a fiducial surface along which the mass flux density presented in Fig. 12 is measured. The lower solid line is the $T = T_{c,max}$ isotherm indicating the disk surface.

The ratio of the pressure gradient to the net gravitational acceleration is then

$$\frac{\partial p/\partial R}{\rho g_{net}} = -\frac{2p/R}{(\rho GM_c/R^2)(1 - y^{-1})} = -\frac{H_c^2}{R^2}\frac{y}{y - 1}, \quad (5.1)$$

where the scale height H_c is given in equation (4.10). The two forces balance at $y - 1 \sim H_c^2/R^2 = 2T^*\xi \equiv 2T/T_g$. Therefore, we expect significant outward motion once the temperature approaches the Keplerian value $T_g \equiv GM_c \mu/(R_0 k)$. As a result, it is possible for the area of a flow tube at the sonic point to actually be smaller than it is at the base of the transition region (i.e., at $T_{c,max}$). This parameter range of flow tube geometries was not explored in BMS.

We turn now to the prediction of the mass flux density as a function of radius. The mass flux density along the disk surface is shown in Figure 10 along with the analytical
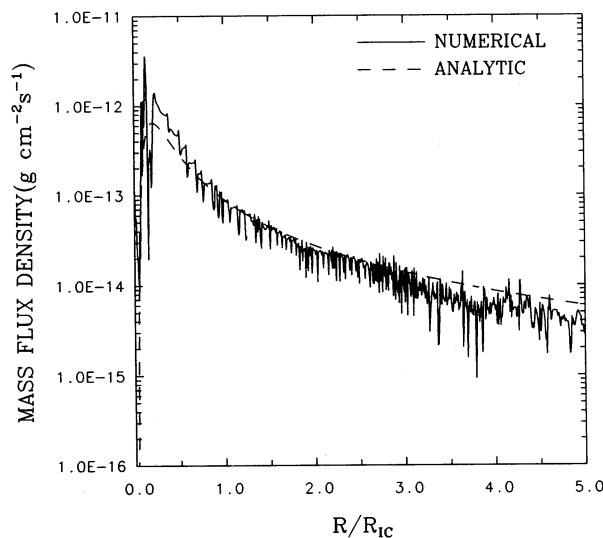

FIG. 8.—Velocity vectors of the inner $0.5R_{IC}$ region for the model in Fig. 7. Note the sharp increase in velocity near $R = 0.2R_{IC}$.

FIG. 10.—Mass flux density (solid line) as a function of radius for the model in Fig. 7 measured along the $T = T_{c,max}$ isotherm depicted in Fig. 9. The small-scale oscillations arise from the unresolved structure of the disk/corona interface. See text for detailed discussion. The dashed line is the analytic prediction from eq. (4.8).

prediction of § 4. Again, for our purposes we define the disk surface to be $T = T_{c,\max}$ (but see also footnote 8). Ignoring for the moment the fine-scale oscillation, overall there is excellent agreement with the analytic prediction, although there may be a systematically lower prediction of the mass flux density for $R \lesssim 3.5R_{IC}$. This is certainly a striking result considering that there were no adjustable parameters in the analytic theory to scale it to our numerical results. Given the caveats discussed in § 4 on the differences between the numerical simulations and the analytic theory of BMS, it is a little surprising that there is such good agreement. This lends support to the assertion of BMS that the mass flux density is a rather robust quantity. At small radii there appears to be an exponential rise, but the amplitude of the oscillations has increased there, making it difficult to discern.

The small-scale oscillations are basically stationary in time, i.e., they are spatial, not temporal oscillations. The oscillations are a result of the finite resolution of the disk/corona interface; that is, when the transition from disk to corona is spatially unresolved, the disk interface is represented by a sequence of stair steps. Each stair step induces clockwise vorticity, much like flow over a corner. On the inner edge of the step, the induced vorticity accelerates the overall wind flow pattern, while on the outer edge of the step the vortex serves to inhibit the flow, causing the mass flux density to oscillate across the step. As evidence of this vortex, Figure 11 shows the velocity vectors for the inner $0.3R_{IC}$ region with the magnitudes all normalized. Obvious vortex structures are seen which are associated with steps in the disk/corona interface. There is no evidence of any such vortex structures at radii greater than about $0.2R_{IC}$, where the vigorous wind begins. Vorticity is being produced by the steps at larger radii, but the magnitude of the overall flow pattern is larger, thus masking the vorticity pattern from the step. This also explains why the magnitude of the oscillations in Figure 10 is so much larger at small radii; namely, the vortical structures produce velocities which are of the order of the weak flow pattern in this gravitationally bound region.
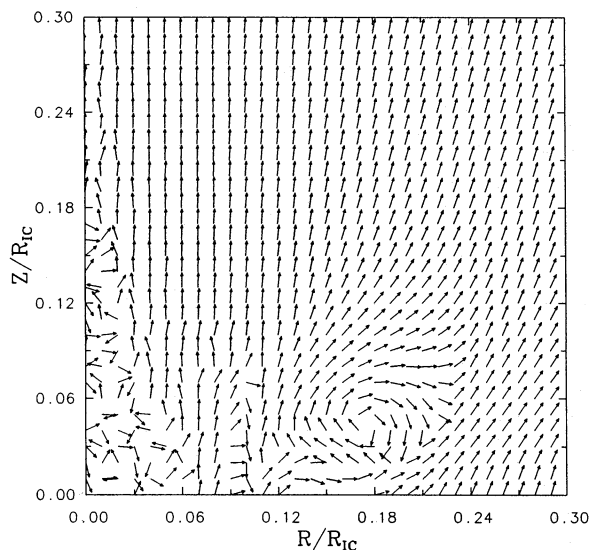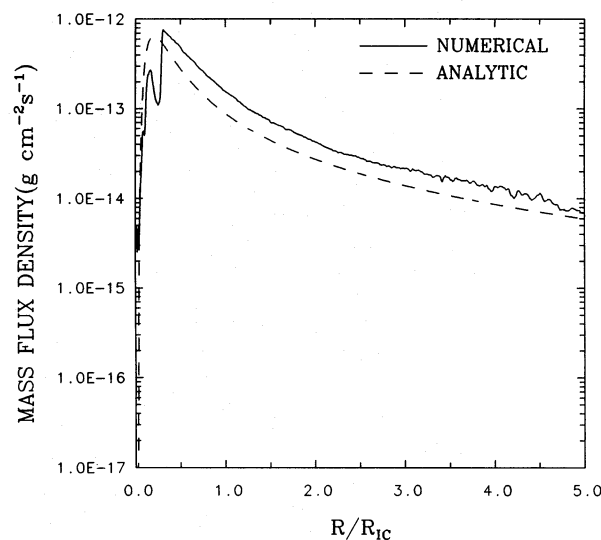

FIG. 12.—Mass flux density measured along the fiducial surface depicted by the dashed line in Fig. 9. This surface is far enough above the disk interface that the mass flux is smooth here.
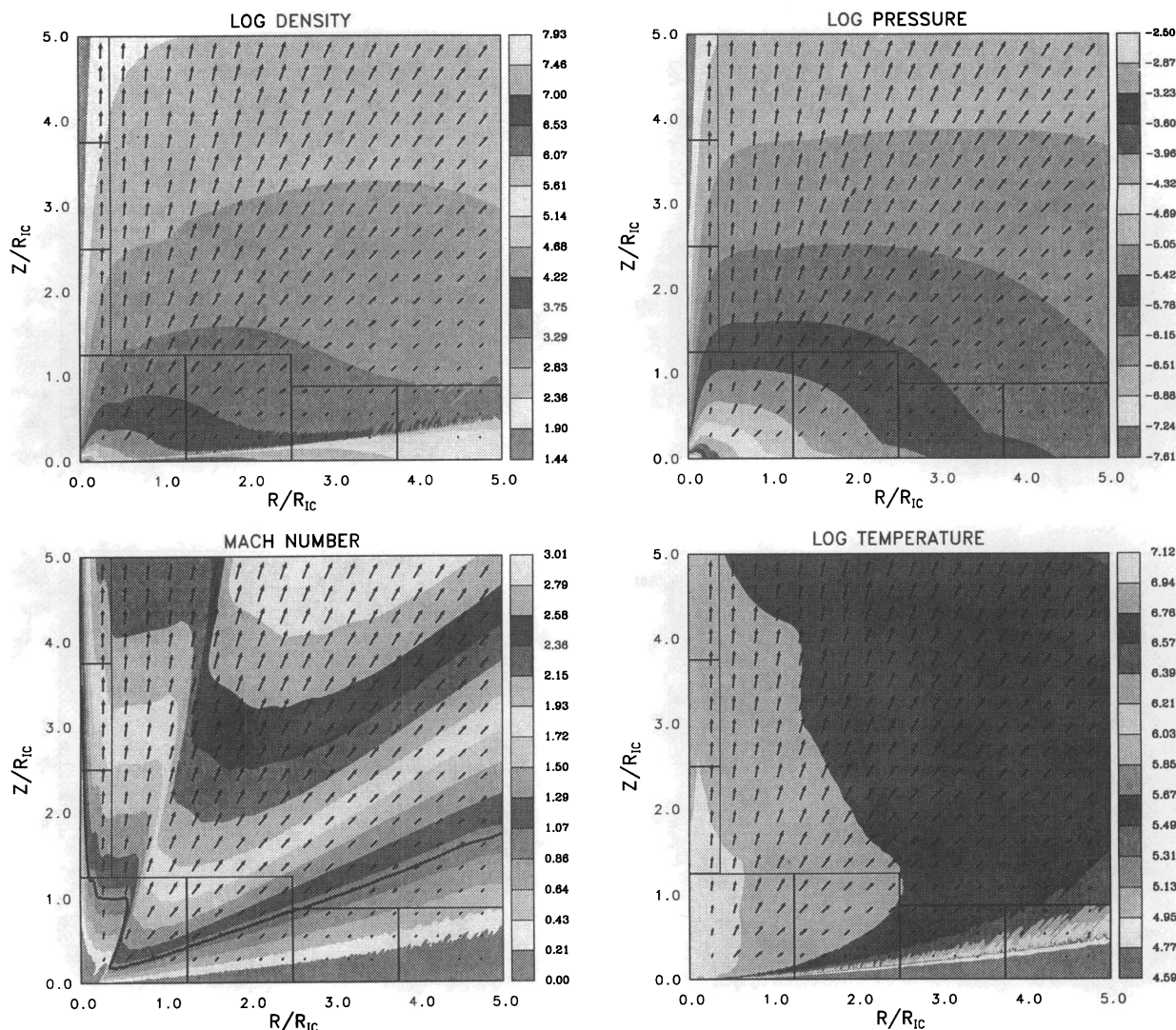
As further evidence that the oscillations are strictly a disk interface phenomenon, we have measured the mass flux density as a function of radius along an arbitrary surface slightly above the disk. This surface is represented by the dashed line in Figure 9. The mass flux density (Fig. 12) is much smoother than that measured near the disk, indicating that the effect of the vortexes dies out rather quickly with height. The slight increase in graininess for $R \gtrsim 3R_{IC}$ arises both because the measuring surface closes back in on the disk/corona interface so that vorticity effects become important, and because the disk interface takes on a more irregular structure. At small radii there is clearly evidence of an exponential rise, but there is a large dip near $0.2R_{IC}$ due to the large vortex structure pictured in Figure 11. Because of the weakness of the wind in the inner corona, the vorticity produced from the disk interface extends to larger heights. Notice that the magnitude of the flow no longer agrees as well with the analytic curve for $R \gtrsim 0.5R_{IC}$. The mass flux density measured along this new surface must be adjusted since (1) the flow tubes have been compressed since leaving the disk, and (2) the mass flux is plotted as a function of its present location in R, not its original location R_0 (Fig. 9). Thus, in order to compare the mass flux density along this new surface with the analytic results, the magnitude should be reduced by the amount of flow tube compression and shifted to smaller radii. The combination of these effects would then bring it back into agreement with the overall behavior of the mass flux density in Figure 10.

Finally , we can add one more argument in favor of our interpretation of the oscillations in the mass flux density: the behavior as a function of luminosity. Given our hypothesis, we would expect in the low-luminosity cases, where the heating time and length scales are larger, that the disk/corona interface can be spatially resolved, and the oscillations should disappear. We find this to be true (§ 5.1.2), and therefore we are confident in our conclusion as to the origin of the oscillations.

5.1.2. Luminosity Dependence
5.1.2.1. Overall Structure

We present calculations for $L/L_E = 1.0$, 0.08, and 0.01, which for $T_{IC} = 1.3 \times 10^7$ gives $L/L_{cr} \approx 13$, 1.0, and 0.13,

FIG. 11.—Velocity vector plot of the inner $0.3R_{IC}$ region with all vectors normalized to unity so that they only indicate direction. Note the large vortex structure centered at a radius of $\approx 0.18R_{IC}$.

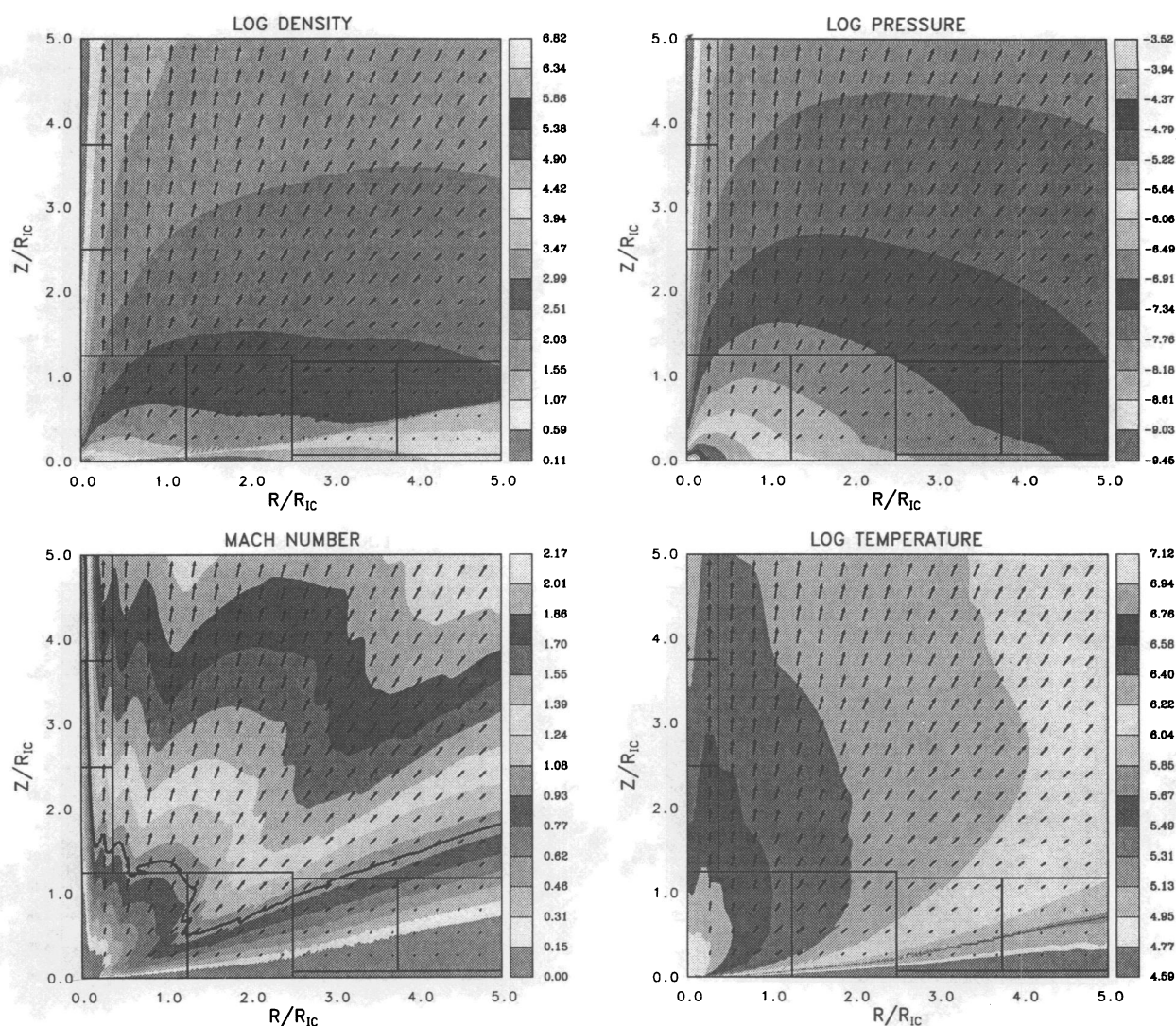FIG. 13.—Same as Fig. 7 for the case of $L/L_E = 1.0$

respectively. The hope here is to be able to identify the three different wind regimes depicted in Figure 5. The three calculations presented in this section were performed with a maximum spatial resolution of 160 cells per Compton radius;[12] we assume $R_{sp} = 0.1R_{IC} = R_{hot}$.

Consider the high-luminosity case, $L/L_E = 1.0$. This simulation is inaccurate due to our neglect of radiation pressure, but we discuss the results to identify the behavior in the high luminosity regime. (Note that for spectrum 2 in which $T_{IC} = 10^8$ K, a similar value of L/L_{cr} would exist for $L \approx 0.35L_E$, in which case radiation pressure effects would be less important.) The steady state structure is shown in Figure 13. Qualitatively, the density, pressure, and Mach number are very similar to those in Figure 7. Quantitatively, the densities and pressures are higher approximately in proportion to the increased luminosity. The maximum Mach number is 3 for this calculation compared to 2.9 for $L/L_E = 0.3$; the maximum velocity is ≈ 930 km s^{-1} compared to ≈ 720 km s^{-1} in Figure 6. The maximum Mach number in this simulation is smaller than the simple

increase in velocity would dictate because of the larger temperature associated with the enhanced heating rate in the $L/L_E = 1.0$ model. For $L/L_E = 1.0$, there is a much larger region which is nearly isothermal at about the Compton temperature. Also, the irregular fine-scale structure along the disk/corona interface is not apparent until a larger radius in the present model. Given the identical spatial resolution of the two models, this is to be expected because of the larger heating rate. The adiabatic sonic surface is very similar in shape to the $L/L_E = 0.3$ case, especially in predicting a weak flow originating from $R_0 \lesssim 0.25R_{IC}$, which goes supersonic at a height $\sim R_{IC}$.

In Figure 14 we present the results for $L/L_E = 0.08(L/L_{cr} \approx 1)$. The most notable difference between this calculation and previous models is the shape of the adiabatic sonic surface. The sonic surface is much noisier, since the vortices associated with the stair step representation of the disk interface have a more noticeable effect on a weaker overall flow pattern (maximum velocity ≈ 484 km s^{-1}). Another important difference is that the sonic surface for flow from small radii ($R_0 \lesssim 0.5R_{IC}$) is at even larger heights than the previous models. This is consistent with the BMS prediction that in changing over from a nearly isothermal corona to a nonisothermal corona (i.e., going from region E

---

[12] This resolution is sufficient for adequately viewing the overall structure. A discussion of the spatial convergence as related to the mass flux density is given in §6.2.

FIG. 14.—Same as Fig. 7 for the case of $L/L_E = 0.08$

to region D in Fig. 5), the height of the sonic point would increase with decreasing luminosity. In addition, the location of the minimum height of the sonic surface has moved outward in radius. The dramatic increase in velocity at low heights seen in previous models between $0.2R_{IC} \lesssim R_0 \lesssim 0.3R_{IC}$ is now located between $0.5R_{IC} \lesssim R_0 \lesssim 0.75R_{IC}$. For flow from $R_0 \gtrsim 0.75R_{IC}$, the adiabatic sonic surface is basically at the same height as the previous two models. The temperature throughout most of the wind region is cooler than in the higher luminosity models, and the hot, nearly isothermal corona ($T \gtrsim 10^7$ K) extends to less than $0.5R_{IC}$ above the disk. Between $4R_{IC} \lesssim R \lesssim 5R_{IC}$, the disk/corona interface has become noticeably smoother, a result of the heating scale heights being spatially resolved. As we will see shortly, the mass flux density from this region also becomes noticeably smoother.

Finally, in Figure 15 the results for a low-luminosity model $L/L_E = 0.01 (L/L_{cr} \approx 0.13)$ are shown. This calculation is performed on a larger grid ($12R_{IC} \times 12R_{IC}$) because the maximum height of the sonic surface keeps increasing with decreasing luminosity. This calculation has a coarse grid of 120×120 zones with two additional levels of refinement, each with a factor of 4 (i.e., maximum resolution of 160 cells per R_{IC}). According to Figure 5, the inner part of

the wind should represent a gravity-inhibited wind (region C), while the outer part is a steadily heated, free wind (region B). The height of the sonic surface is greatly increased for streamlines emanating from $R_0 \lesssim 2R_{IC}$. From other calculations, we find that for $L/L_E \lesssim 0.02$, the sonic surface height increases approximately as L^{-1} for flow from small radii. The minimum in the sonic surface height occurs at $R_0 \approx 3R_{IC}$. Given that the near discontinuity in the height of the sonic surface has moved to large radii for this low-luminosity model, it seems inappropriate to identify it as the transition between corona and wind (although such as identification is appropriate for $L/L_E \gtrsim 0.1$). Instead, this feature indicates the transition from a gravitationally inhibited flow, which only goes supersonic at large heights, to a vigorous free wind which goes supersonic at low heights. This identification is consistent with the prediction of BMS at low luminosities (Fig. 5). For $R_0 \gtrsim 3.5R_{IC}$, the adiabatic sonic surface is similar to the higher luminosity models, i.e., height increasing almost linearly with radius. The maximum velocity within the grid is ≈ 230 km s^{-1}. Thus, the wind speed in the nearly constant velocity regime scales roughly as $L^{-1/3}$. The temperature throughout the wind region is much cooler than in previous models. In fact, the flow from the vigorous free wind region $R_0 \gtrsim 3.5R_{IC}$ reaches
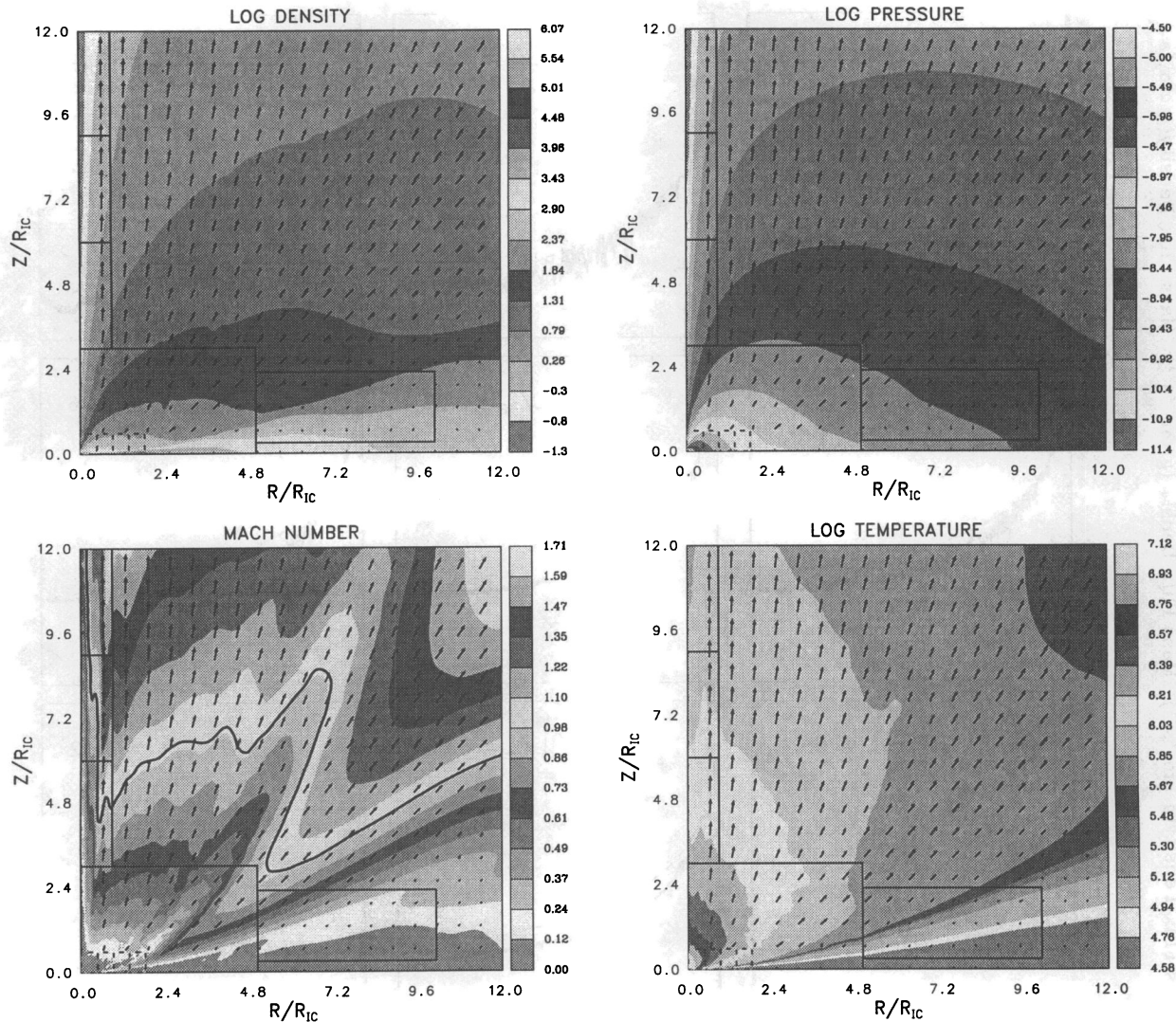
FIG. 15.—Same as Fig. 7 for the case of $L/L_E = 0.01$. The dashed-line boxes shown near the R-axis for $R < 2R_{IC}$ is the region for which a third level of refinement has been used.

a maximum temperature of less than 10^6 K. The disk interface at these radii is spatially well resolved and extended. This, combined with the fact that the temperatures are only marginally larger than $T_{c,max}$, makes, it difficult to define where the disk ends and the corona/wind begins.

5.1.2.2. Mass Flux Density

The primary quantitative prediction from our models is the mass flux density as a function of radius. We report here on an extensive grid of models as a function of luminosity covering the range $0.0025 \leq L/L_E \leq 1.0$ which, given $L_{cr} \approx 0.08 L_E$, corresponds to $0.03 \lesssim L/L_{cr} \lesssim 13$. All of the computations reported in this section are on a larger spatial grid ($20R_{IC}$ square grid) than the previously discussed calculations. This is necessary to better identify the slope of the mass flux density at large radii and to try to pinpoint the transitions (if any) between the different regimes. Even with AMR, it is necessary to reduce the maximum spatial resolution down to 40 cells per R_{IC} because of the long timescales involved in arriving at a steady state. In comparing our results with the higher resolution calculations, we find this resolution to be insufficient to measure accurately the exponential rise of the mass flux density at small radii

($R_0 \lesssim 0.2R_{IC}$). However, at large radii the coarser resolution seems to have a minimal effect on the magnitude of the mass flux density, except, of course, for the small-scale oscillations (see also § 6.2). As such, the discussion here will focus primarily on the solution in the wind region $R \gtrsim 0.5R_{IC}$. In Figure 16 the mass flux density as a function of radius is presented for selected luminosities. The mass flux density is measured along the disk/corona interface given by the $T = T_{c,max}$ surface. Also, we have plotted for reference in this figure the analytic prediction for Compton-heated winds from § 4 (eq. [4.8]), although non-Compton heating and cooling are expected to be significant at low luminosities and large radii.

Before discussion the overall shape of the curve, consider the behavior of the small-scale oscillations. At large luminosities, the small-scale oscillations are pronounced at all radii in our simulations. As the luminosity is decreased, the amplitude of the oscillations decreases. Smooth curves exist at large radii for $L \lesssim 0.1L_E$. This is the result of spatially resolving the transition region due to increased heating scale lengths. Thus, the luminosity dependence of the mass flux density supports our contention that the small-scale spatial oscillations are the result of vortices set up by insufficient resolution of the disk/corona interface.
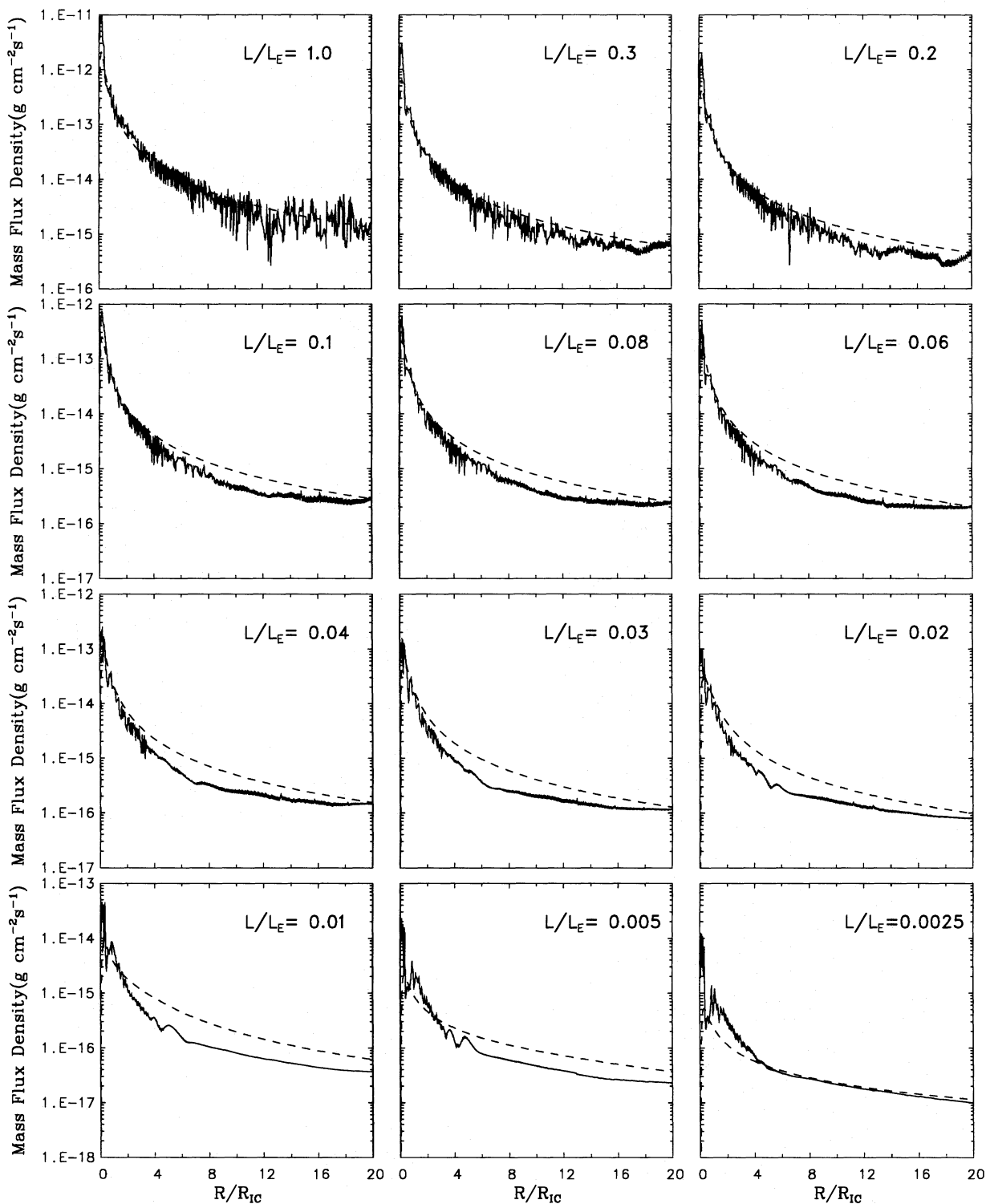
FIG. 16.—Mass flux density as a function of radius for the low-T_{IC} case (spectrum 1 in Table 1). All calculations were performed on a $20R_{IC} \times 20R_{IC}$ grid with a maximum resolution of 40 cells per R_{IC}. Models span a luminosity range of $0.0025 \leq L/L_E \leq 1.0$. The dashed line is analytic prediction of the mass flux density given by eq. (4.8).

As for the overall shape of the mass flux density, least-squares fits to our results indicate two regimes. At high luminosity, the mass flux density is well described by $\dot{m} \propto R_0^a$, where a is in the range $-1.9 \gtrsim a \gtrsim -2.0$. At low luminosities, a two-component fit is more appropriate with $-1.9 \gtrsim a \gtrsim -2.0$ for $R \lesssim R_{tr}$ and $-1.0 \gtrsim a \gtrsim -1.2$ for $R \gtrsim R_{tr}$, where R_{tr} is the radius representing the transition between these two solutions. The shallower slope solution is evident only for $L/L_E \lesssim 0.1$. R_{tr} decreases with decreasing

luminosity for $L/L_E \gtrsim 0.01$ and is nearly constant for $L/L_E \lesssim 0.01$. Because this transition is not always sharp, our estimate of R_{tr} is, of course, approximate. The slope of the mass flux density for $R_0 \gtrsim R_{tr}$ is somewhat uncertain due to the limited dynamical range of the region, and because the flow at large radii leaves the grid subsonically. By computing models on different size grids, we have found the slight rise in mass flux density in the range $18R_{IC} \lesssim R_0 \lesssim 20R_{IC}$ to be a boundary condition effect, most likely

associated with the exit of material subsonically. The mass flux density varies rather simply with luminosity; $\dot{m} \propto L$ is a fairly good approximation to our results (although for $L/L_E \gtrsim 0.1$, $\dot{m} \propto L^{0.85}$ is a more accurate representation). We can summarize our results through a fit of the mass flux density of the form

$$\dot{m} = C_0 \frac{L}{L_E} \left(\frac{R_0}{R_{IC}}\right)^{-2} f(L)g(R_0)$$

$$\times \exp\left\{\frac{-[1 - (1 + 0.25 R_{IC}^2/R_0^2)^{-1/2}]^2}{2 R_0/R_{IC}}\right\}, \quad (5.2a)$$

where the functions f and g are given by

$$f(L) = \begin{cases} 1, & \text{for } L/L_E \leq 0.1, \\ (0.1 L_E/L)^{0.15} & \text{for } L/L_E \geq 0.1, \end{cases} \quad (5.2b)$$

$$g(R_0) = \begin{cases} 1, & \text{for } R_0 \leq R_{tr}, \\ R_0/R_{tr} & \text{for } R_0 \geq R_{tr}, \end{cases} \quad (5.2c)$$

and the transition radius, R_{tr}, is given by

$$\frac{R_{tr}}{R_{IC}} = \begin{cases} 6 + 5.4 \log\left(\frac{L/L_E}{0.01}\right) + 4.1\left[\log\left(\frac{L/L_E}{0.01}\right)\right]^2 \\ \qquad\qquad\qquad\qquad\qquad \text{for } L \geq 0.01 L_E, \\ 6, \qquad\qquad\qquad\qquad \text{for } L \leq 0.01 L_E. \end{cases} \quad (5.2d)$$

A value of $C_0 = 5 \times 10^{-13}$ g cm^{-2} s^{-1} provides the best fit to the data in Figure 16 to within $\sim 25\%$ (ignoring the small-scale oscillations). However, as we will discuss in § 6.2, there is some variation in the mass flux density with spatial resolution. The calculations presented are rather coarse (a maximum of 40 cells per R_{IC}). Based upon convergence studies, we extrapolate that in the limit of excellent resolution

$$C_0 \approx 3 \times 10^{-13} \text{ g cm}^{-2} \text{ s}^{-1} \quad (5.2e)$$

(see § 6.2). As for the exponential term in equation (5.1a), we have found this form, suggested by Shields et al. (1986), to be consistent with our data. In the limit of small radii, it yields $\dot{m} \propto \exp(-0.5 R_{IC}/R_0)$, reflecting the influence of gravitational stratification in the nearly hydrostatic corona.

As described in § 4, a direct comparison with BMS is not appropriate for many of these low Compton temperature models because of our inclusion of additional heating/cooling mechanisms which are important at the low temperatures reached along streamlines at large radii or low luminosities. However, we discuss some of the global comparisons of these solutions. The first point is that the numerical results agree to within a factor of 3 over all luminosities studied. This is a striking result considering there were *no* adjustable parameters to the theory by which to scale the results. For large luminosities ($L/L_E \gtrsim 0.3$), our numerical results agree very well with BMS. As the luminosity decreases, disagreement begins to appear first at large radii. At $L/L_E = 0.1$, we can begin to see the R_0^{-1} behavior in the numerical results at large radii ($R_0 \gtrsim 14 R_{IC}$). This solution works its way inward with decreasing luminosity until at $L/L_E = 0.01$ it is at $R_0 \approx 6 R_{IC}$. This point ($L/L_E = 0.01$, $R_0 \approx 6 R_{IC}$) represents the maximum disagreement between our models and the analytic results of BMS. From Figure 5 we see that at this luminosity the gravity-inhibited wind (region C) extends out about $4 R_{IC}$. The BMS theory predicts that the mass flux density in this region goes

as R_0^{-1}, whereas the numerical results indicate a slope in this region of roughly R_0^{-2}, thus leading to the BMS theory predicting a larger mass flux density than what is indicated in our numerical results. Conversely, at larger radii ($R_0 \gtrsim 6 R_{IC}$), the numerical results show a mass flux density with a radial dependence of R_0^{-1}. In the BMS theory the wind is in the steadily heated, free-wind regime (region B) with a mass flux density of $R_0^{-5/3}$. Thus, for $R_0 \gtrsim 6 R_{IC}$ the two solutions close back in on each other with increasing radius.

Finally, consider the lowest luminosity model $L/L_E = 0.0025$. The BMS theory predicts that the wind is gravity inhibited (region C) out to about $64 R_{IC}$ with the mass flux density going as R_0^{-1}. For $R_0 \lesssim 5 R_{IC}$, the numerical results are higher than that of BMS because the mass flux density is going as R_0^{-2}. However, for $R_0 \gtrsim 5 R_{IC}$ the agreement is exceptional, with both the numerical and the analytic going as R_0^{-1}. However, we believe this extraordinary agreement to be fortuitous based upon their luminosity dependences. That is, the mass flux density of BMS has a luminosity dependence of L^2, which is different from our numerical results which go roughly as L. We suspect that at lower luminosities the BMS prediction will yield a smaller mass flux density than our numerical result at these radii. However, we could not verify this computationally because of the large computational time required of the low-luminosity models based on the need for a large problem space and long evolution time.

To summarize, then, the mass flux density of our numerical models agrees best with the predictions of BMS at large luminosities. This is not surprising, since it is at large luminosities that the effects of the additional heating and cooling mechanisms included in our numerical models will be least important. In addition, we have found that in the outer part of region B ($R_0 \gtrsim R_{tr}$), the mass flux density goes as R_0^{-1}, where R_{tr} is given by equation (5.2d). Although this radial dependence is characteristic of region C, the gravity-inhibited wind, we are confident that the solution in the outer region is not gravity inhibited for two reasons. First of all, the movement of this region with luminosity is inconsistent with the prediction of BMS for region C. That is, it shows up first at large radii for intermediate luminosities ($L/L_{cr} \approx 1$) and moves inward with decreasing luminosity. Contrast this to region C in Figure 5. Second, the wind in this region possesses a low sonic point location ($\approx 0.6 R_0$), whereas the region C sonic point should lie at large heights. In addition, as we will see in § 5.2, this region does not exist in the high T_{IC} case. Therefore, we conclude that this region is attributable to the additional heating and cooling mechanisms included, and/or to the fact that the maximum temperatures are not much larger than $T_{c,max}$. We would not have expected BMS to have predicted this behavior.

5.1.2.3. Radius-Luminosity Parameter Space

We now present a radius-luminosity parameter space plot of our simulations similar to that of BMS shown in Figure 5. In order to discuss the transitions between the various corona and wind solutions, we need a few working definitions. We begin by defining a coronal solution using the following criteria: (1) the flow velocities must be predominantly subsonic throughout the region, going supersonic only at large heights (i.e., $s_{sonic}/R_0 \gg 1$, where s_{sonic} is the distance measured along the streamline from the base of the transition region to the adiabatic sonic point), and (2) the maximum temperature along a streamline should be at

least $T_{h,\min}$ (see Fig. 2). Using these two criteria, the corona is found to extend out to about the same radius independent of luminosity, the mean radius being roughly $0.25R_{IC}$. As mentioned earlier, the nearly constant radial extent of the corona is a prediction of BMS and is related to the dominant heating term in the corona being Compton heating, which regulates the temperature in terms of the *quality* of the spectrum (i.e., T_{IC}) rather than the *quantity* (i.e., L). For $L/L_{cr} \gtrsim 2$, it is criterion (1) which sets the coronal boundary, while for $L/L_{cr} \lesssim 2$ criterion (2) is the relevant constraint. We find, in fact, that for $L/L_{cr} \gtrsim 2$ the shape of the adiabatic sonic surface is nearly independent of luminosity. For $L/L_{cr} \lesssim 2$, the height at which the flow goes supersonic and the radial extent of the subsonic region increase with decreasing luminosity. However, the flow from $R_0 \gtrsim 0.25R_{IC}$ for $L/L_{cr} \lesssim 2$ does not reach a temperature of $T_{h,\min}$, and as such it is not considered part of the corona. We label this instead as the gravity-inhibited wind region. Similarly, in order to identify the transition between an isothermal (region E) and nonisothermal corona (region D), we use the criterion that a region is isothermal if the temperature at the isothermal sonic point is larger than $0.5T_{IC}$. Using the same definition, we can also separate out the isothermal wind solution (region A) from the steadily heated wind solution. Finally, for the gravity-inhibited wind (region C), we identify it through the location of the sonic point. That is, the transition from region B to region C is taken to be the radius at which the adiabatic sonic surface makes the quick transition from a low sonic point to a high sonic point.

Given these definitions, we can now summarize our models in terms of the radius-luminosity plot shown in Figure 17. It should be remembered that the divisions drawn in this figure are approximate. We concentrate initially on the coronal regions. The corona is divided into an isothermal and nonisothermal part. The division in luminosity between these two regions is uncertain due to a lack of models; however, we estimate it to be at about $L/L_{cr} \approx 2$. There is plenty of uncertainty in the form of the mass flux
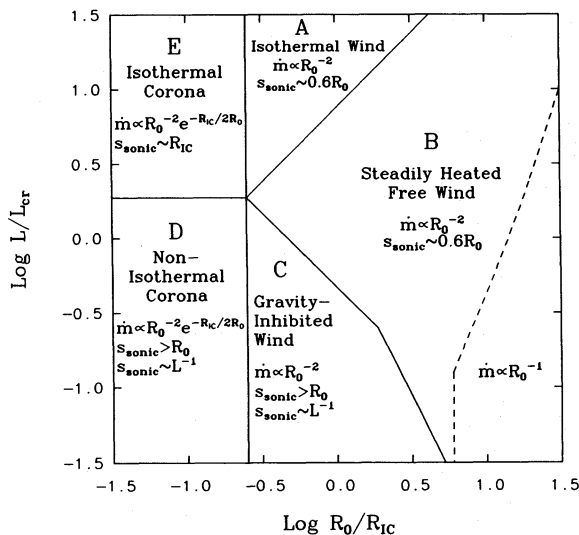
density in the corona due to the softening radius and the effect of the vortexes from the stair step representation of the disk interface. However, our results seem consistent with a mass flux density at small radii of the form $\dot{m} \propto R_0^{-2} \exp(-0.5R_{IC}/R_0)$. Note that this form provides a peak in the mass flux density at $R_0 = 0.25R_{IC}$, which is reasonably consistent with our data. Within the corona the sonic point lies at a height of $\sim R_{IC}$ in the approximately isothermal corona, whereas the sonic point height increases with decreasing luminosity as roughly L^{-1} in the non-isothermal corona. Many of these characteristics are in agreement with those predicted by BMS. This seems reasonable since the additional heating/cooling mechanisms included in our models are unimportant in the corona in which Compton heating and cooling dominate. Two noticeable exceptions to this rule are that the analytic prediction of the corona/wind interface is at $0.1R_{IC}$, and the sonic point height in the nonisothermal corona should be proportional to L^{-2}. As for the location of the corona/wind interface, this is not a major discrepancy, since it was mainly a qualitative prediction. As we mentioned in § 4, the original version of BMS placed this interface at R_{IC} based upon the simple interpretation of the Compton radius. However, we have moved it into $0.1R_{IC}$ because the mass flux formulae of BMS show that there can be an appreciable wind at this radius. Thus, there is considerable uncertainty about where the interface should lie, and it is not surprising that the particular definition of the corona we have chosen (a very reasonable definition) might result in a different location. Also, BMS indicated that their analysis is most uncertain in the range $0.1R_{IC} \lesssim R_0 \lesssim R_{IC}$. However, their decision to extrapolate wind solutions in from R_{IC} down to $0.1R_{IC}$ seems to have been appropriate and provides the best agreement. On the second point, since the location of the sonic point in the nonisothermal corona is governed by the details of the flow geometry, it is not surprising that the predicted sonic point location differs from our numerical results. In addition, in the nonisothermal regime more of the flow is at temperature significantly below the Compton temperature, where the additional heating/cooling mechanisms may have a significant effect.

In the wind regime ($R_0 \gtrsim 0.25R_{IC}$), we have identified the three primary solutions identified by BMS, namely, the isothermal wind, the steadily heated free wind, and the gravity-inhibited wind. At large luminosity (region A), the wind is nearly isothermal at the Compton temperature out to the isothermal sonic point, with a mass flux density varying as R_0^{-2}, and the adiabatic sonic point located at low heights (typically $0.6R_0$). By comparison with Figure 5, we see that the boundary between regions A and B (R_{AB}) is virtually identical to that predicted by BMS, with $R_{AB} \propto L$. Of course, a different criterion would have yielded an altered location for the A–B boundary. For example, if we had chosen the criterion that the temperature at the isothermal sonic point be larger than $e^{-1}T_{IC}$, then the boundary would have been shifted downward in luminosity but still given by $R_{AB} \propto L$. Thus, the correct slope for this boundary appears to be a fairly robust result. At large radii for all luminosities, we find the steadily heated free wind (region B) solution. The wind here is characterized by a low sonic point ($s_{sonic} \approx 0.6R_0$) and a mass flux density going as R_0^{-2}. These characteristics compare favorably with the predictions of BMS. For region B, BMS find that $\dot{m} \propto R_0^{-5/3}$. This difference is probably not significant, but it does help explain why the numerical results tend to show a smaller mass flux density

FIG. 17.—Radius-luminosity parameter space plot for the numerical solutions to the low-T_{IC} (1.3×10^7 K) models. The luminosity is scaled relative to the critical luminosity (eq. [4.4]) which for this spectrum yields $L_{cr} \approx 0.08L_E$. The dashed line outlines that part or region B for which the mass flux density changes from $\dot{m} \propto R_0^{-2}$ to $\dot{m} \propto R_0^{-1}$. See text for details.

than the analytic prediction in region B, especially for $L/L_{cr} \lesssim 1$. We have outlined with a dotted line (see eq. [5.2d]) that part of region B for which $\dot{m} \propto R_0^{-1}$, as described earlier. We feel that although the functional dependence of the mass flux density has changed, the wind solution is still part of the steadily heated regime. The position of the sonic point is still at $s_{sonic} \approx 0.6R_0$. The non-Compton heating and cooling mechanisms, as well as the fact that the peak temperature in this part of the wind is not significantly higher the disk temperature $T_{c,max}$, may have a hand in producing the altered form for the mass flux density, since we do not find this behavior in the higher T_{IC} case (see § 5.2, where we address this question in greater detail). Finally, at low luminosity and intermediate radii, we have found the gravity-inhibited wind (region C). This solution is characterized by a sonic point at large heights, the location of which increases with decreasing luminosity. Also, the mass flux density is proportional to R_0^{-2}. Comparison with Figure 5 shows that there are some differences between the analytic predictions of BMS in the spatial extent of region C as a function of luminosity. In addition, the mass flux density is inconsistent with the region C prediction of BMS of $\dot{m} \propto R_0^{-1}$. Given that the BMS theory may not be applicable at low luminosities for these low

Compton temperature models, these differences are not surprising. This is further evidenced by the fact that the higher Compton temperature models (§ 5.2) show a B–C boundary which is closer to the prediction of BMS. However, we still find in the higher Compton temperature models that the mass flux density in region C tends to favor a R_0^{-2} dependence, although this is somewhat uncertain due to the large spatial fluctuations of our numerical results in the gravity-inhibited regime. Overall, we can say that where we expect the numerical results to be applicable to the theory of BMS, the results compare quite favorably.

5.2. $T_{IC} = 10^8$ K Models

We now present results using spectrum 2 in Table 1. As mentioned earlier, spectrum 2 ($T_{IC} \approx 10^8$ K, $L_{cr} \approx 0.03L_E$) provides a better approximation to the conditions assumed in BMS because much of the wind region is dominated by Compton heating and cooling, and the temperatures are appreciably larger than $T_{c,max}$. Overall, these models are very similar to the lower Compton temperature models for high luminosities ($L/L_{cr} \gtrsim 1$) but do show differences at low luminosities ($L/L_{cr} \lesssim 1$). Most notably, we do not find an $\dot{m} \propto R_0^{-1}$ solution at low luminosities and large radii, as we did in the low Compton temperature models.
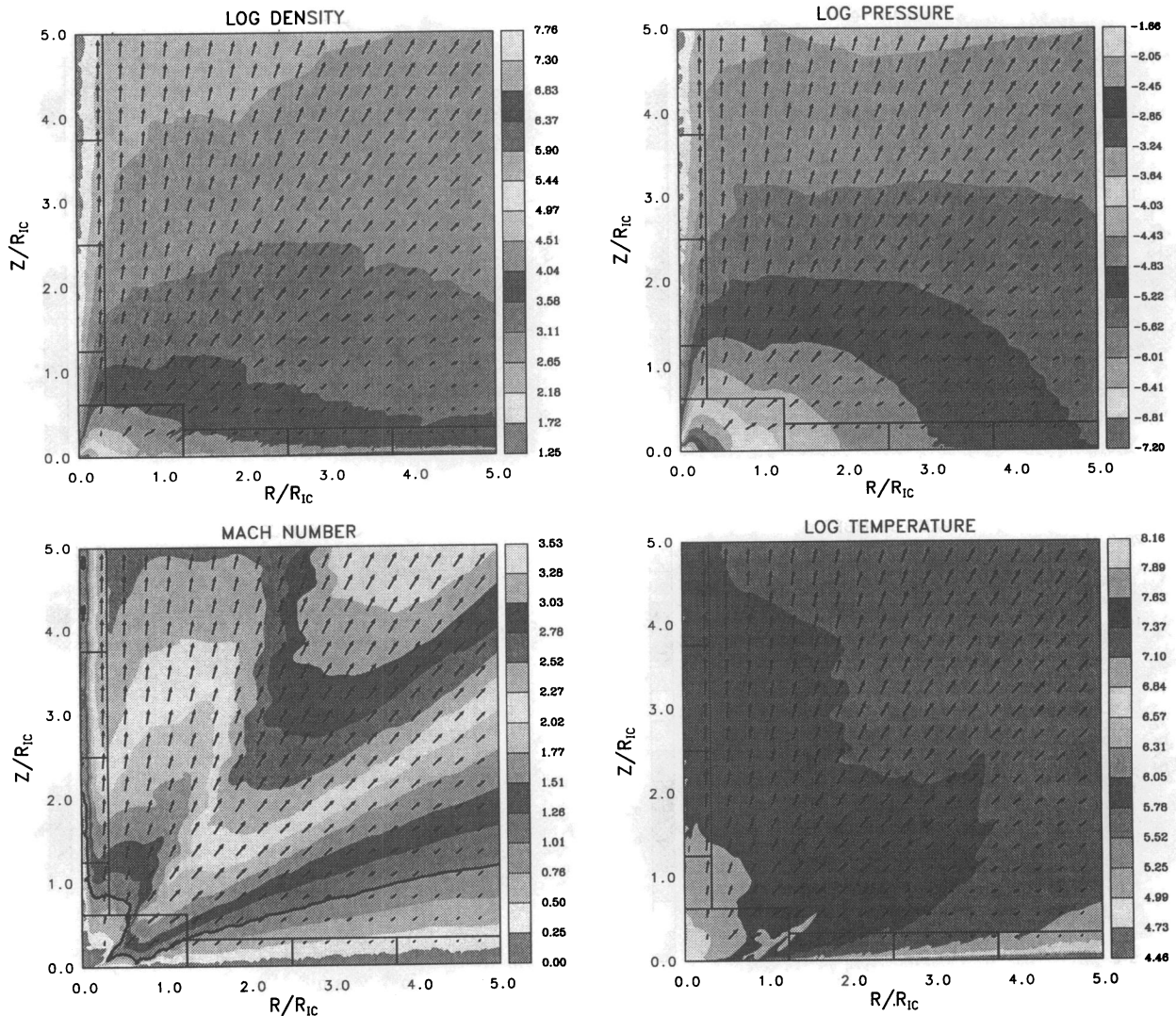

FIG. 18.—Same as Fig. 7 for the high-T_{IC} (10^8 K) case with $L/L_E = 0.1$

In Figure 18 we present the steady state structure obtained for $L/L_E = 0.1$ (i.e., $L/L_{cr} \approx 3$) on a $5R_{IC}$ square grid. This calculation employed a grid of 200 coarse cells in each direction and one level of refinement by a factor of 4 (i.e., maximum resolution of 160 cells per R_{IC}). This model is compared with a similar L/L_{cr} model in the low-T_{IC} case ($L/L_E = 0.3$; Fig. 7). The Mach surface possesses the same general shape as in the lower T_{IC} model. That is, at small radii $R_0 \lesssim 0.25R_{IC}$, the flow goes supersonic at a height R_{IC} above the disk, while at $R_0 \gtrsim 0.25R_{IC}$ the Mach surface rises nearly linearly with radius. The Mach number contours show more noise than in the lower T_{IC} case, for flow emanating from $R_0 \lesssim R_{IC}$. This is because of the stronger vortical structures produced from the larger density jump at the disk interface owing to the higher Compton temperature. We note also that the disk is thinner in the higher T_{IC} model. This is a result of the smaller gravitational scale heights in the disk. At small heights, the hydrostatic drop in pressure behaves like a Gaussian with a scale height $H^2 \propto T R^3$. Thus, the scale height measured in Compton radii goes as $H/R_{IC} \propto (T/T_{IC})^{1/2}(R/R_{IC})^{3/2}$ (eq. [4.10]). The thinner disk is a result not only of the Compton temperature being raised, but also of the fact that the temperature in the disk is lower ($T_{c,max} \approx 5 \times 10^4$ K). The

maximum velocity in the wind is ≈ 2000 km s^{-1}, which is up by the square root of the Compton temperature ratio, as one would expect based upon the velocity scaling (eq. [2.6]). The maximum Mach number is slightly larger in the higher T_{IC} case because the temperature at large heights increased less than linearly in T_{IC}, due to the enhancement of adiabatic losses from the higher velocities.

Figure 19 shows the steady state structure of the wind for $L/L_E = 0.005$ (i.e., $L/L_{cr} \approx 0.17$). The calculation was performed on a $20R_{IC}$ square grid with a 100×100 coarse grid and two additional levels of refinement, both employing a refinement factor of 4 (i.e., maximum resolution is 80 cells per R_{IC}). This model is best understood when comparing it with the lower T_{IC} model of $L/L_E = 0.01$ ($L/L_{cr} \approx 0.13$) in Figure 15. Other than the thinner disk, the most noticeable difference is in the shape of the Mach surface. For the higher T_{IC} model, the Mach surface shows appreciable variation in the flow from small radii. More importantly, the minimum in the Mach surface location is not reached until $R_0 \approx 6R_{IC}$, as can be seen in Figure 20, where the streamlines are plotted. In general, we find for low luminosities that the radius of the minimum height of the Mach surface (R_{min}) goes roughly as $L^{-4/3}$. This is in contrast to the low-T_{IC} case, where we found it to go roughly as $L^{-1/2}$ for $L/L_E \lesssim 0.02$.
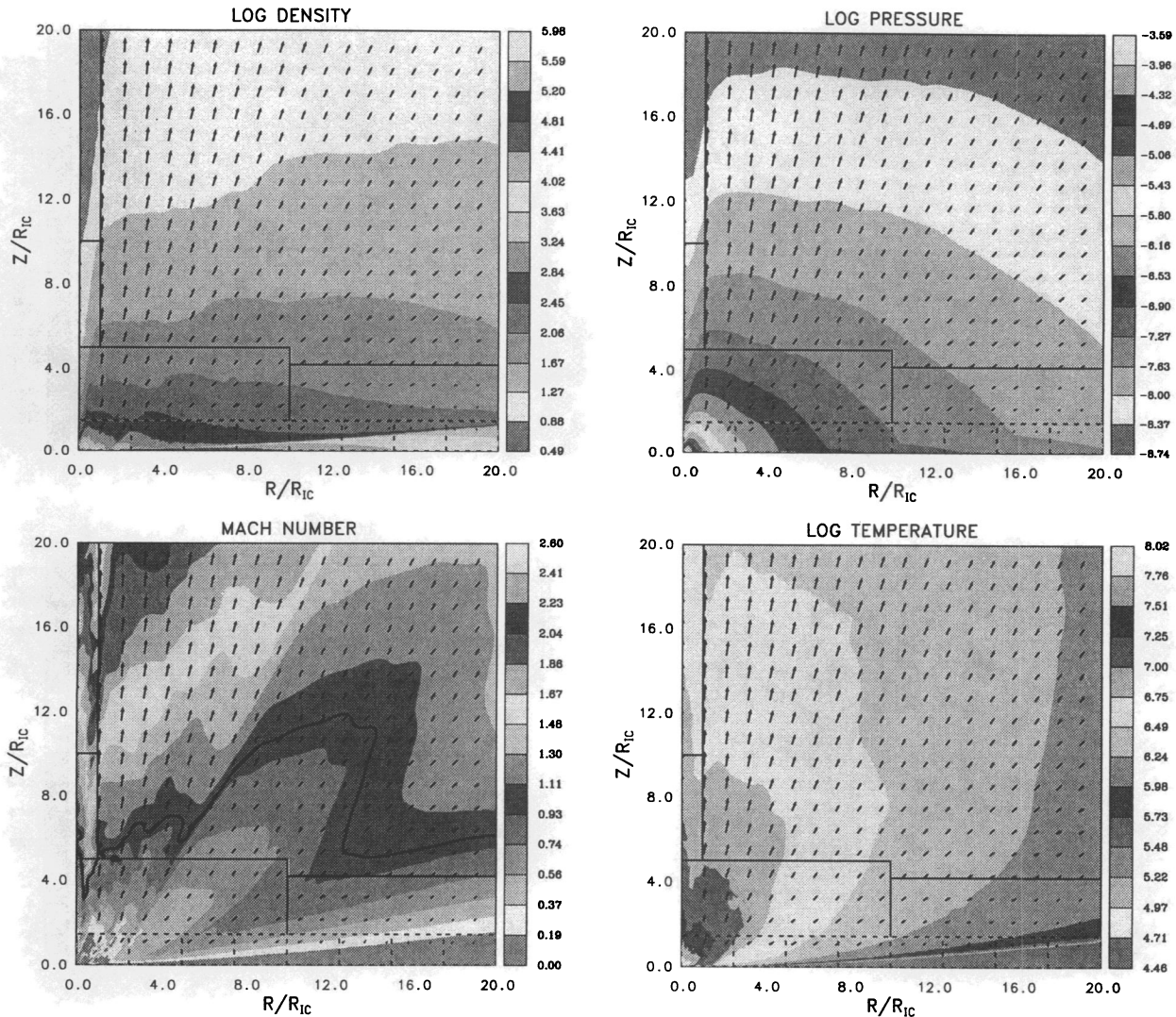

FIG. 19.—Same as Fig. 18 for the case of $L/L_E = 0.005$. The dashed-line boxes indicate the regions for which a third level of refinement has been used.
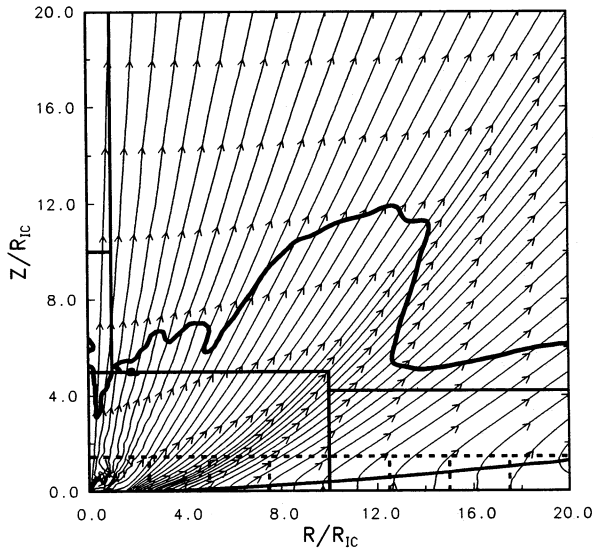
FIG. 20.—Streamline plot for the model in Fig. 19. The upper solid line is the sonic surface. The lower solid line is the $T = T_{c,max}$ isotherm indicating the disk surface.

FIG. 22.—Streamline plot for the low-T_{IC} (1.3×10^7 K) model with $L/L_E = 0.01$. Note the large flare in the disk at large radii. This is typical of the behavior in the low-T_{IC} case, where the gravitational scale heights can become large at large radii.

The maximum velocity reached at large heights is 720 km s^{-1}, again consistent with the $T_{IC}^{1/2}$ scaling. Perhaps the most significant difference is in the shape of the mass flux density curve (Fig. 21). A least-squares fit shows that $\dot{m} \propto R_0^{-2}$ for $R_0 \lesssim 6R_{IC}$ and $\dot{m} \propto R_0^{-1.7}$ for $R_0 \gtrsim 6R_{IC}$. An important point here is that we see no region at large radii in which $\dot{m} \propto R_0^{-1}$, as we did in the low-T_{IC} case. A closer examination reveals the reason for this change. At the sonic point, both the high- and low-T_{IC} models show a radial dependence of $(\rho v)_{sonic} \propto R_0^a$, with a in the range $-1.4 \gtrsim a \gtrsim -1.5$. Thus, the different radial dependence $\dot{m}$ must be a flow geometry issue. That is, the ratio of the area at the sonic point to the area at the base differs appreciably between the two models. Taking the area ratio to vary as R_0^b, we find that b is in the range $-0.3 \gtrsim b \gtrsim -0.4$ for the higher T_{IC} model, and $0.3 \lesssim b \lesssim 0.4$ in the lower T_{IC} model. For comparison, we show in Figure 22 the streamlines for the case of $L/L_E = 0.01$ with $T_{IC} = 1.3 \times 10^7$ K on a $20R_{IC}$

square grid. Note the large flare in the disk due to the gravitational scale heights becoming large at large radii. An artifact of the pronounced flare is that the flow pattern is not essentially vertical below the disk interface at $T = T_{c,max} \approx 1.7 \times 10^5$ K. Consequently, the radius at which we are measuring the mass flux does not coincide with the radius from which the flow is emerging and the area of the flow tube does not match the area of the flow tube at the point at which the flow enters our grid through the bottom boundary. This fact can lead to an additional ambiguity in comparing the mass flux densities between the high- and low-T_{IC} models. Ideally, one could remedy this problem by simply measuring the mass flux density along the bottom boundary. However, this turns out to be impractical, since we would have to evolve the problem long enough for the flow pattern *inside* the disk to have settled down to a steady state, i.e., a few flow times. The flow inside the disk is at such low velocities that this takes a very long time. In general, we find the computational requirements for this criteria to be prohibitive.[13] So we are limited to measuring the mass flux density at the disk interface, i.e., along $T = T_{c,max}$. We emphasize here that although the flow measured along the bottom boundary is not yet in a steady state, the flow measured at the disk interface is basically steady in time. This is because the conditions in the wind are determining the mass flux density at the disk interface, while the disk itself serves only as a mass source.

We can understand the change in the flow pattern in Figure 22 from vertical to radial before reaching the disk interface by comparing the magnitude of the radial pressure gradient and the gravitational attraction. Evaluating the ratio at the disk interface and using the fact that $p_{c,max} = L/(c4\pi R^2 \Xi_{c,max})$, we can write

$$\frac{\partial p_{c,max}/\partial R}{-\rho_{c,max}\, G_0 M_c/R^2} = 2 \frac{T_{c,max}}{T_{IC}} \frac{R}{R_{IC}} . \qquad (5.3)$$
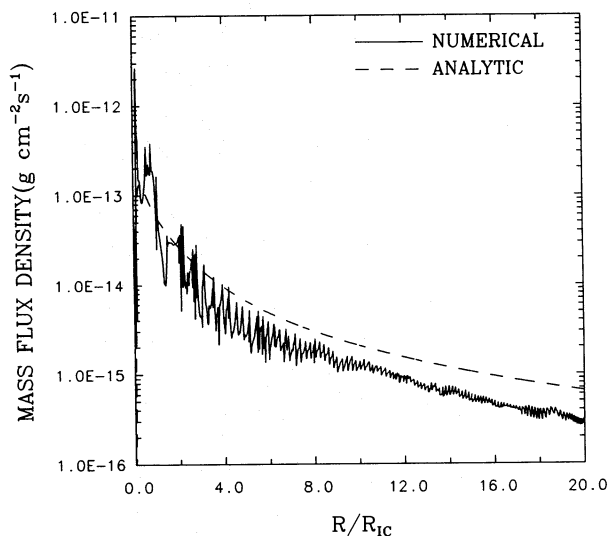

FIG. 21.—Mass flux density as a function of radius for the model in Fig. 19 (*solid line*) measured along the $T = T_{c,max}$ isotherm depicted in Fig. 20. Dashed line is the theoretical prediction from eq. (4.8).
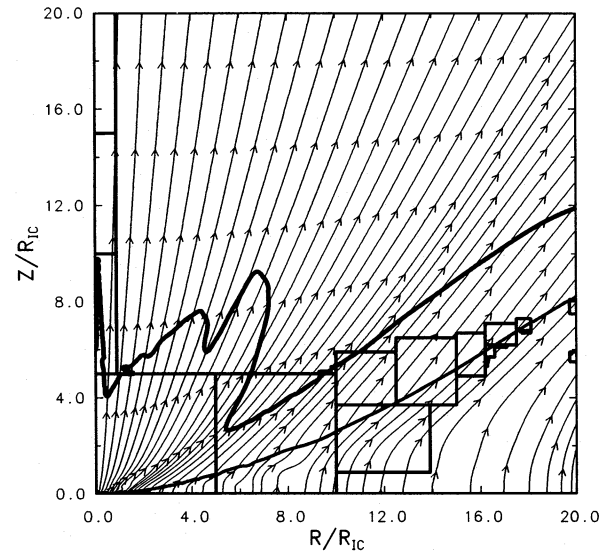
[13] We have performed one such calculation for a high-T_{IC} case, and indeed the mass flux density measured along the bottom bounary is in fact comparable to that measured at the disk interface.

Of importance here is the increase in pressure gradient force relative to gravity with radius. Thus, at large enough radii, the radial pressure gradient dominates and the flow turns radial. Since $T_{c,max}/T_{IC} \approx 0.01$ for the low-T_{IC} case, we see that the ratio is unity at $R \approx 50R_{IC}$, although the flow in fact turns radial at smaller radii because of rotation. Another important point concerning equation (5.3) is that in the higher Compton temperature models the pressure gradient force is reduced not only because T_{IC} is higher, but also because $T_{c,max}$ is reduced. Thus, we expect the flow in the disk to remain essentially vertical up to the disk interface (as is seen in Fig. 20). However, above the disk interface the temperature increases greatly, thus increasing the radial pressure gradient (relative to gravity) and causing the flow to turn radial.

Regardless of the mechanism, the significance of a radial dependence in the ratio of the area at the sonic point to that at the base should not be overlooked. It implies, given that the sonic point height scales linearly with the radius, that the tube *shapes* are changing with radius. In other words, the flow tubes are not homologous. For the high-T_{IC} case in which the area ratio decreases with radius, the flow tube compression at the sonic point increases with increasing radius. For the low-T_{IC} case, the tubes are also not homologous, as evidence by the fact that the flow tubes could turn radial before even reaching the disk surface ($T = T_{c,max}$ isotherm). Thus, an accurate description of the flow topology would involve not just a single description for the divergence of a flow tube, but rather must include a parameterization which changes with radius.

Figure 23 shows the mass flux density as a function of radius for the high-T_{IC} case for luminosities in the range $0.002 \le L/L_E \le 0.3$. These models were all calculated with the same resolution (maximum 40 cells per R_{IC}) on a $20R_{IC} \times 20R_{IC}$ grid, with the exception of the lowest luminosity case ($L/L_E = 0.002$), which was calculated on a $40R_{IC} \times 40R_{IC}$ grid with a maximum of 20 cells per R_{IC} resolution. As in Figure 16, we have also plotted the analytic prediction for Compton-heated winds from § 4 (eq. [4.8]). In general, the mass flux density shows greater small-scale oscillation for the higher T_{IC} case because the density jumps at the disk interface are larger, thus enhancing the production of vorticity. In comparing with the analytic theory, we find even better agreement than in the low T_{IC} case, as we might have expected. Typically the mass flux density (ignoring the small-scale oscillation) agrees to within about a factor of 2, with the worst agreement occurring for the lowest luminosity models. In performing least-squares fits to our results, we find that $\dot{m} \propto R_0^{-2}$ is a good fit for $R_0 \le 20R_{IC}$ for $L/L_E \gtrsim 0.03 \approx L_{cr}/L_E$. At low luminosities, the mass flux density shows an $\dot{m} \propto R_0^{-2}$ dependence at small radii ($R_0 \le R_{BC}$) and $\dot{m} \propto R_0^{-1.7}$ at large radii ($R_0 \ge R_{BC}$), where R_{BC} is the radius of the minimum height of the Mach surface which we take to be the division between regions B and C. We note that this differs from the low-T_{IC} case in which the radius at which there was a change in the mass flux density (R_{tr}, eq. [5.2]) did not correspond with the B/C interface. We can describe the fit to the mass flux density with the same form as the low-T_{IC} case using equation (5.2a), only now the functions $f(L)$ and $g(R_0)$ are given by

$$f(L) = \begin{cases} (0.03 L_E/L)^{1/2} & \text{for } L/L_E \le 0.01 \,, \\ 1 & \text{for } L/L_E \ge 0.01 \,, \end{cases} \quad (5.4a)$$

$$g(R_0) = \begin{cases} 1 & \text{for } R_0 \le R_{BC} \,, \\ (R_0/R_{BC})^{0.3} & \text{for } R_0 \ge R_{BC} \,, \end{cases} \quad (5.4b)$$
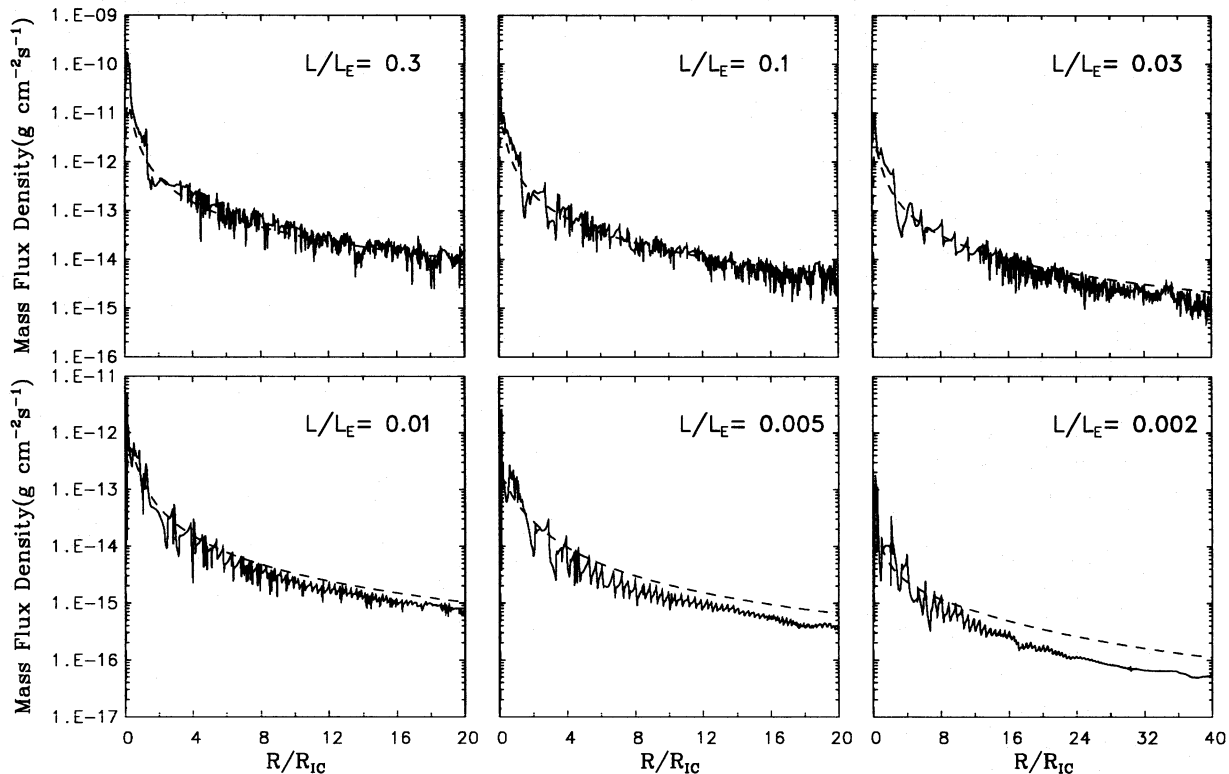

FIG. 23.—Mass flux density as a function of radius for the high-T_{IC} (10^8 K) case. All calculations were performed on a $20R_{IC} \times 20R_{IC}$ grid (with the exception of the $L/L_E = 0.002$, case which is calculated on a $40R_{IC}$ square grid) with a maximum resolution of 40 cells per R_{IC}. Models span a luminosity range of $0.002 \le L/L_E \le 0.3$. The dashed line is the analytic prediction given by eq. (4.8).

and the transition radius, R_{BC}, can be represented by

$$R_{BC}/R_{IC} = \begin{cases} 0.25(0.05L_E/L)^{1.3} & \text{for } L \leq 0.05L_E , \\ 0.25 & \text{for } L \geq 0.05L_E . \end{cases} \quad (5.4c)$$

The best fit to the data is provided by $C_0 = 1.4 \times 10^{-11}$ g cm^{-2} s^{-1}. Again, we find that the mass flux density does decrease somewhat with spatial resolution (see § 6.2). We estimate, based upon convergence studies, that the appropriate value in the limit of excellent resolution would be

$$C_0 \approx 10^{-11} \text{ g cm}^{-2} \text{ s}^{-1} . \quad (5.4d)$$

There is an exception to this fit for the lowest luminosity model, $L/L_E = 0.002$, which shows a slightly reduced slope ($\dot{m} \propto R_0^{-1.6}$) for $R_0 \leq R_{BC}$. Thus, our analytic fit somewhat overpredicts the mass flux density at small radii for this model, but the fit is accurate at large radii ($R_0 \geq R_{BC}$).

Comparing our results with the analytic prediction of BMS, the main discrepancy appears to be in the gravity-inhibited wind. Assuming this solution regime is bounded in radius by the minimum in the Mach surface height at low luminosities (i.e., R_{BC}, eq. [5.4c]), we find that $\dot{m} \propto R_0^{-2}$ at $L/L_E = 0.005$. whereas theory predicts $\dot{m} \propto R_0^{-1}$. However, at this luminosity region C is restricted to such a narrow range of radii that the BMS theory may not be valid. Therefore, we consider a lower luminosity, $L/L_E = 0.002$, at which region C spans over a decade in radius, with $R_{BC}/R_{IC} = 14$. Again we find a discrepancy in the slope, $\dot{m} \propto R_0^{-1.6}$. For $R_0 > R_{IC}$, this difference in slope is small enough that the numerical results agree with the theory to within about a factor of 2. At smaller radii, the difference between our results and the theory is larger, approaching an order of magnitude at $0.25R_{IC}$. Both the theory and our numerical results are uncertain in this region: the theoretical estimate of the mass flux density is based on an interpolation of the theory developed for $R_0 > R_{IC}$, and that for $R_0 < 0.1R_{IC}$, whereas the numerical results are subject to large-amplitude fluctuations arising from the vortices just above the disk interface. Because of the large computational demands of the low-luminosity problems, it is not feasible at the present time to provide the very high-resolution simulations that would be needed to determine an accurate value for the mass loss in this case. It would be of some interest to do so, since the higher mass-loss rate we find could have important observational consequences.

At large radii ($R_0 \gtrsim R_{BC}$), the numerical results possess a slope similar to what is predicted by the analytic results ($\sim R_0^{-5/3}$), but the magnitude is smaller in the numerical result; it is down by about a factor of 2 for $L/L_E = 0.002$. This is not surprising at low luminosities since equation (4.9) indicates that for this model non-Compton processes should be important in the heating the cooling outside of $\approx 7R_{IC}$.

In Figure 24 we present the luminosity-radius parameter space plot for these high Compton temperature models. We have used the same criteria as in the low-T_{IC} case in distinguishing the different solution regimes. We find the characteristics of the coronal region to be practically identical to that of the lower T_{IC} case. The width of the coronal region is again a constant with luminosity at about $0.25R_{IC}$, and the transition from isothermal to nonisothermal corona is near $L/L_{cr} \sim 2$. The isothermal wind region (region A) occupies the same location in parameter space as the lower T_{IC} models, with the boundary radius increasing with lumi-
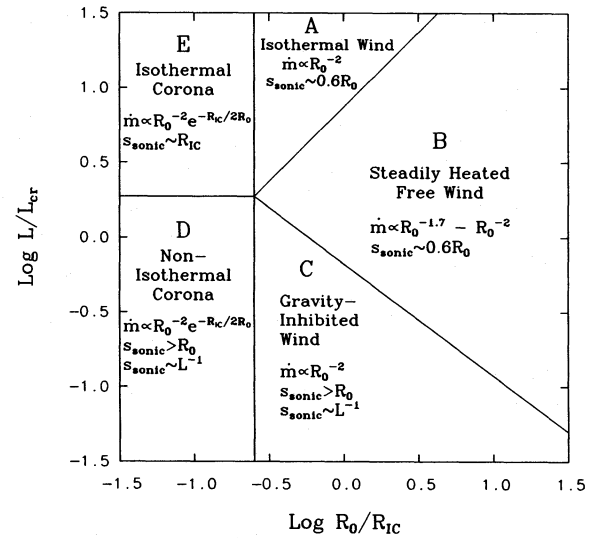

FIG. 24.—Radius-luminosity parameter space plot for the numerical solutions to the high-T_{IC} (10^8 K) models. The luminosity has been scaled relative to the critical luminosity (eq. [4.4]) which for this spectrum is given by $L_{cr} \approx 0.03L_E$. Note that this figure is similar to the analytic prediction shown in Fig. 5. See text for detailed discussion.

nosity. These two results are an important confirmation of the BMS theory, in that when Compton processes dominate, the solution characteristics scale in a predictable manner as a function of Compton temperature. The primary difference between the high and low Compton temperature models is in regions B and C. In region B we do not find the $\dot{m} \propto R_0^{-1}$ solution at large radii in the high-T_{IC} case; this is consistent with BMS. Also, for $L/L_{cr} \lesssim 1$, the region B mass flux tends to favor $\dot{m} \propto R_0^{-1.7}$, in agreement with the BMS prediction of $R_0^{-5/3}$, although the significance of this result can be debated given the similarity of the $R_0^{-5/3}$ to R_0^{-2}. As for region C, the spatial extent is larger in the high-T_{IC} case. The B/C boundary is given by equation (5.4c) with $R_{BC} \propto L^{-4/3}$. Contrast this to the low-T_{IC} case in which $R_{BC} \propto L^{-1}$ for $L/L_E \gtrsim 0.02$, and $R_{BC} \propto L^{-1/2}$ for $L/L_E \lesssim 0.02$. Although still not in agreement, the high-T_{IC} case is closer to the analytic prediction of $R_{BC} \propto L^{-2}$. Still, the overall similarity of Figure 24 to the prediction of BMS in Figure 5 is quite striking.

To summarize the high-T_{IC} models, at high luminosity ($L/L_{cr} \gtrsim 1$) the results scale in a predictable manner with the low-T_{IC} models and agree extremely well with the predictions of BMS over all radii. At low luminosities, the high-T_{IC} results do not show the $\dot{m} \propto R_0^{-1}$ dependence at large radii seen in the low-T_{IC} case; instead, $\dot{m} \propto R_0^{-1.7}$. Also, the radius at which the transition from gravity-inhibited wind to free wind (i.e., R_{BC}) increases with decreasing luminosity faster in the high-T_{IC} case than in the low-T_{IC} case. The agreement between the analytic mass flux density and the high-T_{IC} results becomes worse with decreasing luminosity, presumably because of the influence of non-Compton processes in the heating and cooling. Still, the analytic mass flux density of BMS is typically within a factor of 2 over the range of luminosities and radii studied in our models. The most significant difference between the analytic theory and the high-T_{IC} models appears to be the form of gravity-inhibited solution (region C). Here we find that the scaling of the mass loss with radius ($\dot{m} \propto R_0^{-1.6}$–$R_0^{-2}$) is consistent with that found in the low-T_{IC} case but is much steeper than predicted by theory ($\dot{m} \propto R_0^{-1}$).

This difference in slopes results in a significant difference in the value of $\dot{m}$ only inside R_{IC}, where our numerical results are subject to large fluctuations. We leave it to future calculations to determine whether the high mass-loss rates indicated by our numerical results for these small radii are valid; if so, accretion disk winds from low-luminosity X-ray binaries should be more readily observable than previously thought. We note also that the discrepancy between our results and the theory in region C may be attributable to the ratio of the gravitational timescale to heating timescale being a slowly varying function of luminosity. Thus, the transition to the gravity-inhibited wind may not be attained until a lower luminosity than has been sampled so far. The slight decrease in the measured slope of region C for our lowest luminosity model is suggestive along these lines.

6. DISCUSSION

6.1. *Effects of R_{sp} and R_{hot} at Small Radii*

All the calculations presented in this paper have assumed the values of $R_{sp} = 0.1 R_{IC} = R_{hot}$, where R_{sp} is the radius inside of which the gravitational potential is softened, and R_{hot} is the radius inside of which the cold disk drops out of the computational domain so that there is only hot coronal material. Here we comment on the effect of these parameters upon our solutions. We present the results of two calculations for which $T_{IC} = 1.3 \times 10^7$ K and $L/L_E = 0.3$, which differ only in their value of $R_{sp}(0.1 R_{IC}$ and $0.05 R_{IC})$. Both calculations are performed on a spatial grid which is $5 R_{IC} \times 5 R_{IC}$ with a 100×100 coarse grid and two levels of refinement, both a factor of 4 (i.e., maximum resolution of 320 cells per R_{IC}). Figure 25 shows the mass flux density as a function of radius measured along a surface slightly above the disk/corona interface, as we did in Figure 12. We have chosen this surface for comparing the mass flux density because the effect of the vortices near the disk is reduced, allowing us to get a much clearer picture of the mass flux density at small radii. Notice that when the softening radius is reduced by a factor of 2, we are able to obtain a much better delineation of the exponential rise of the mass flux density because it is occurring over the inner $0.1–0.2 R_{IC}$. In

theory, we would like to be performing all our calculations with a softening radius at least this small. However, in practice, this is not always feasible for several reasons. First of all, there is the need to have sufficient spatial resolution to resolve adequately the smaller gravitational scale heights induced by using a smaller softening radius. Second, and what seems to be more important, the smaller softening radius produces a highly evacuated region near the rotation axis. This region is a source of numerical difficulty because small perturbations from denser regions become amplified as they travel into the rarefied region, thus yielding strong shocks which heat the region and slow down the calculations through the Courant condition. To understand the source of the evacuated region, consider the solution to the vertical stratification in an isothermal hydrostatic atmosphere. The vertical momentum equation yields

$$\frac{\partial \ln p^*}{\partial Z^*} = \frac{-1}{T^*}\frac{d\Phi^*}{dZ^*}, \tag{6.1}$$

so that

$$p^*(Z^*) = p(0) \exp\left\{-[\Phi^*(Z^*) - \Phi^*(0)]/T^*\right\}. \tag{6.2}$$

Evaluating this expression along the rotation axis and taking the temperature equal to the Compton temperature (i.e., $T^* = 1$) and using equation (2.21) for the gravitational potential, we have the expression

$$\rho^*(Z^*)/\rho^*(0) = \exp\left\{[(Z^* + Z_{disk}^*)^2 + R_{sp}^{*2}]^{-1/2} - (Z_{disk}^{*2} + R_{sp}^{*2})^{-1/2}\right\}. \tag{6.3}$$

Evaluating equation (6.3) at large heights and using the fact that $R_{sp}^* \gg Z_{disk}^*$, the minimum density in the evacuated region at large heights is

$$\rho^*(Z^* \to \infty)/\rho^*(0) \approx \exp\left(-1/R_{sp}^*\right). \tag{6.4}$$

Thus, the density contrast for $R_{sp}^* = 0.1$ is $e^{-10} \approx 4.5 \times 10^{-5}$, while for $R_{sp}^* = 0.05$ it is $e^{-20} \approx 2.1 \times 10^{-9}$. By simply reducing the softening radius by a factor of 2, the density in the evacuated region along the rotation axis has been reduced by another 4 orders of magnitude. This allows
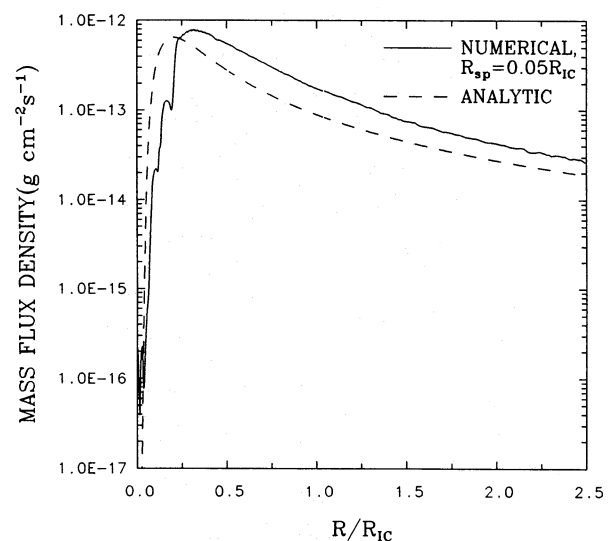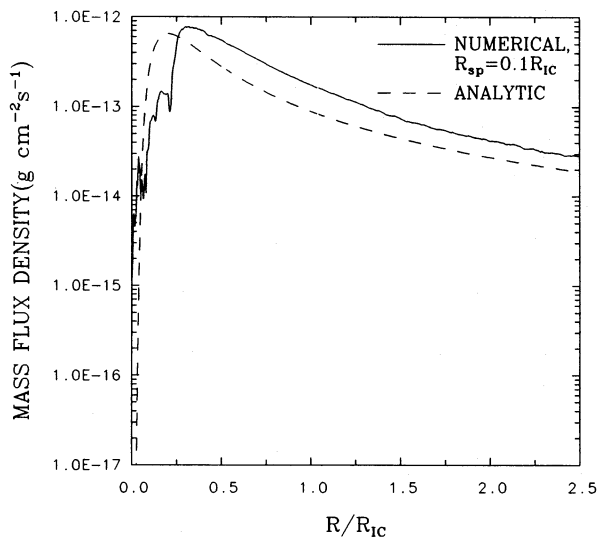

FIG. 25.—Mass flux density curves showing the effect of R_{sp}. Both models have identical model parameters ($L/L_E = 0.3$ using spectrum 1 with $R_{hot} = 0.05 R_{IC}$) and the same resolution. The mass flux density is measured above the disk surface (see Fig. 12) to show off the exponential rise, which is much better defined in $R_{sp} = 0.05 R_{IC}$.

lower amplitude sound waves propagating into this region to steepen into strong shocks, which end up heating this region to high temperatures. Although Compton cooling will attempt to cool the region back down to T_{IC}, it is vastly inferior to the strong shock heating. Therefore, in practice we find it necessary to keep $R_{sp}^* = 0.1$.

We find our calculations to be much less sensitive to the value of R_{hot}. R_{hot} controls the radius at which the cool disk enters the computational grid, and as such it indicates the radius at which vortices arising from the stair step configuration of the disk are induced in the calculation. If the mass flux at small radii is measured above the region (as was done in Fig. 25), then changing this radius has a fairly minimal effect on the calculations outside of this region. Consequently, it was only necessary to keep R_{hot} large enough so that the gravitational scale heights in the cool disk did not become too small. Typically, we have set $R_{hot} = R_{sp}$ to keep the area of influence for this parameter of the same size as the softening potential.

6.2. Spatial Resolution and Time-dependent Behavior

We discuss here in more detail the effect of spatial resolution on our solutions and the significance of the statement that "our calculations produce, in the end, a wind pattern which is *basically* steady in time." In this section we make frequent references to the terms high, low, and intermediate resolution; they apply to our ability to spatially resolve the disk-corona transition region with the use of adaptive mesh refinement. Given that this is a function of radius and luminosity, we defer to these qualitative statements rather than endeavor to provide the exact resolution required.

Although we describe our final solutions as being in a steady state, there may be (depending upon resolution) some slowly evolving features. These features are usually confined to two regions. The first region we have identified previously; it is the disk interface at large radii as seen in Figure 7. For $R_0 \gtrsim 3.5 R_{IC}$, the disk interface changes slowly with time. We have verified that this is mainly a resolution issue. That is, this slow evolution occurs once the spatial resolution becomes, in a sense, intermediate. At low resolution, there is time-steady behavior in this region because the disk interface is represented by essentially a discontinuity in density. The Godunov hydrodynamics does an exceptional job at handling and maintaining the discontinuity. At high resolution, the transition region is resolved and once again there is no problem; the disk interface is stationary in time. This can be seen in Figure 14 for the case of $L/L_E = 0.08$ between $4 R_{IC} \lesssim R \lesssim 5 R_{IC}$ where, because of the reduced luminosity and therefore an increase in the heating timescale, the transition region is starting to become spatially resolved. Note coincidentally, we also see no evidence of fluctuations in the disk interface of the final state in this region. There are, however, some small fluctuations at slightly smaller radii where again the resolution has become intermediate. Experience has shown us that the fluctuations are larger when the intermediately resolved transition region occurs near the outer boundary condition. When it is situated well in the interior of the computational domain, the outer regions seem to provide a damping of the fluctuations. This is the basis for the earlier statement that the boundary conditions are providing a possible feedback in enhancing the fluctuations.

The second region which may show time-dependent behavior is the inner corona just above the disk interface. We isolate this time dependence from that described above because although it is related to spatial resolution, it is not associated with resolving the transition region. The transition region here is completely unresolved and is represented by a discontinuous surface which has a stair step appearance. We remarked earlier that the stair steps give rise to vortex structures which are easily seen in the inner corona due to the overall flow being weak from gravitational attraction. As long as these vortices are well separated in space, the flow will still be nearly stationary in time. However, as the spatial resolution is increased, the stair steps move closer together, and the vortices start to interact with each other, resulting in nonstationary behavior. Thus, the inner corona has the rather interesting behavior that as the spatial resolution is increased, the weak wind of the inner corona can become time varying. This would continue until the resolution becomes large enough to start to resolve the transition region in the inner corona. For the case of $L/L_E = 0.3$, the inner corona is limited to $R \lesssim 0.25 R_{IC}$. To spatially resolve this region requires a spatial resolution which is orders of magnitude higher than what is currently feasible given our computational resources, even with AMR.[14] We find that the time dependence of the inner corona begins at a lower spatial resolution as the luminosity is decreased because of the slower overall flow velocities. In addition, the extent of the time-dependent region increases as the luminosity is decreased as a result of the increasing domain of the gravity-inhibited wind.

We wish to emphasize here that time-dependent behavior in the final state of our calculations is *numerical*, not *physical*. This is of importance because there has recently been a series of papers by Melia and coworkers (Melia et al. 1991; Melia & Zylstra 1992; Melia, Zylstra, & Fryxell 1992) in which, in modeling the inner corona of a disk typical of X-ray binaries, they found extreme time-dependent behavior. Our calculations differ from theirs in several ways. First, their calculation is performed for only the extreme inner corona. Their outer boundary is at a distance of 5×10^8 cm which, given their Compton temperature of 2×10^7 K, corresponds to $0.01 R_{IC}$. Thus, their entire grid is contained within just a few of our innermost zones. Second, they have included flux-limited radiative diffusion in their calculation, whereas we have assumed optically thin radiative heating and cooling. Third, and most importantly, the material is injected upward from the disk with highly supersonic velocities (Mach 27 in the corona). Melia and coworkers do not include any of the disk inside the computational domain but rather use it as a boundary condition. This contrasts greatly from our model, in which we do not specify the velocity in the Z-direction at all but rather have it determined self-consistently by the hydrodynamic evolution. As we mentioned in § 3, this is the appropriate boundary condition if the flow is rising subsonically. Given that our computation includes the disk in which we can safely assume that flow to be subsonic, our boundary condition is the appropriate one. Melia and coworkers are correct in prescribing the velocity normal to the interface for all time, provided it is supersonic. The question then comes down to

---

[14] It is really the Courant time requirement of the inner zones which makes this calculation prohibitive. The number of zones used in resolving the transition region is tolerable, but the number of time steps taken will be prohibitively large.

whether or not the highly supersonic boundary condition should be believed. The large velocity (Mach 27) they use arises from making the incorrect argument that most of the incident flux at the disk comes out as kinetic energy of material rising from the disk. This is completely inappropriate, since most of the radiation is either directly scattered or absorbed and reradiated at other wavelengths (Basko & Sunyaev 1973; Basko et al. 1977; London & Flannery 1982; Tavani & London 1993). Thus, the injection velocity they use is greatly overestimated. This large injection velocity results in the presence of a high-density, optically thick sheath above the disk as the material slows down due to gravity.[15] The time-dependent behavior they find results from the radiation presssure force on this unphysical high-density sheath and is therefore suspect.

Let us turn briefly to a different aspect of time dependence: the assumed constancy of the luminosity of the central source. In our calculations, we have evolved the wind to a steady state from an initially static condition assuming the luminosity to be constant. If the luminosity varies on timescales less than the characteristic flow time $t_C = 5700 \, M_{c8}$ yr (for the typical case of $T_{IC} = 1.3 \times 10^7$ K), the variations will be averaged out, and our results should

be applicable. Similarly, if the variations occur on large timescales, then our results show that the flow reaches a steady state and our results apply again. For example, the mass flux density is within about a factor of 2 of the final result after about $10t_C$ for the case of $L/L_E = 0.3$ (see § 5.1.1). Thus, for variations in the luminosity longer than about $10t_C$, we expect this model to be applicable. Without carrying out the calculation, we cannot say what the effect of variations of the luminosity on a timescale of order $1-10t_C$ would be. We note, however, that Shields et al. (1986) showed that the flow should be stable except in the unlikely case that the mass loss in the wind is substantially greater than the accretion rate.

Finally, we should address the question of spatial convergence in our models. For our purposes, we will measure convergence through the mass flux density at the disk interface. In Figure 26 we show the mass flux density as a function of radius for four different models ($L/L_E = 0.1$ and $T_{IC} \approx 1.3 \times 10^7$ K) which differ only in their spatial resolution (40, 80, 160, and 320 cells per R_{IC}). Also shown in this figure for reference is the fit (eqs. [5.2a]–[5.2d]) with $C_0 = 5 \times 10^{-13}$ g cm^{-2} s^{-1}, the adopted value for the spatial resolution of 40 cells per R_{IC} over a wide range of luminosities. Note that the increased resolution provides a better depiction of the exponential rise in the mass flux density at small radii, thus providing confidence in our fit at

---

[15] Although the velocity is high, at radii less than about 2×10^8 cm it is still gravitationally bound.
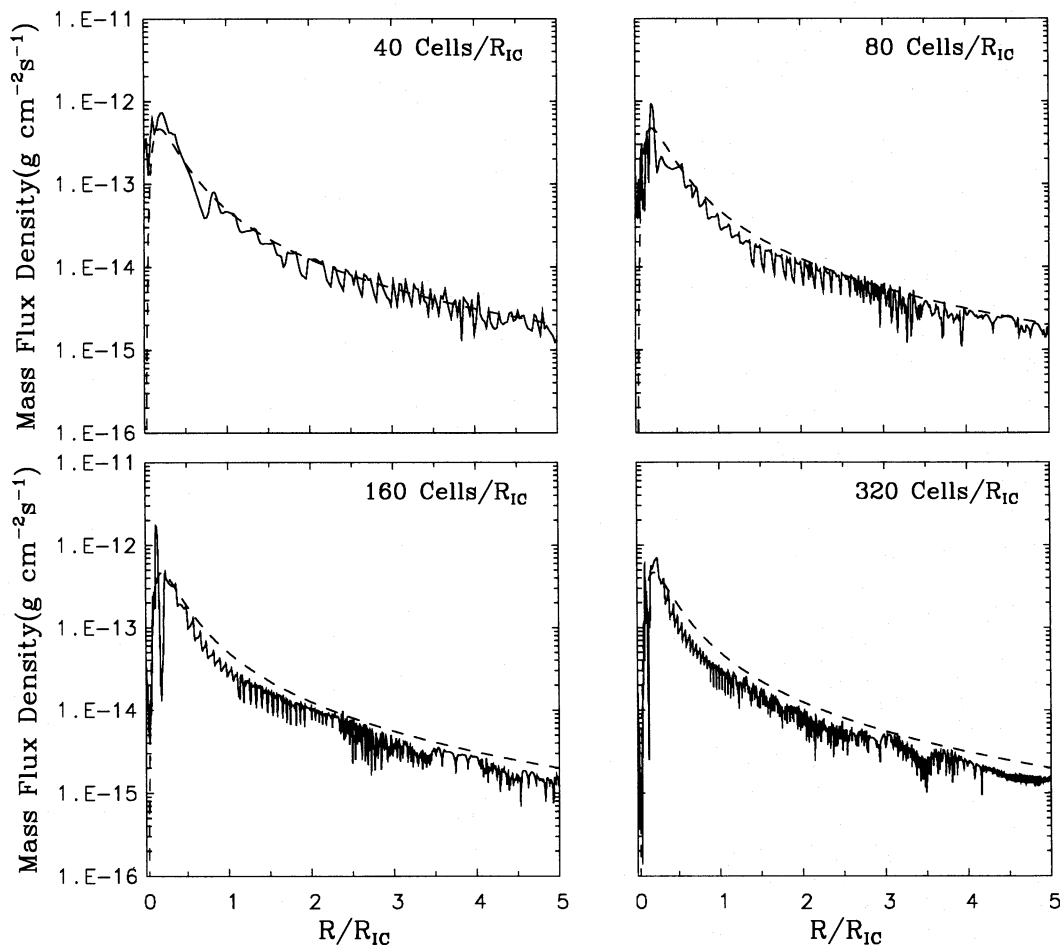

FIG. 26.—Mass flux density as a function of radius for the identical problem ($L/L_E = 0.1$ using spectrum 1) calculated on four different spatial resolutions from 40 to 320 cells per R_{IC}. The dashed line is the numerical fit (eqs. [5.1a]–[5.1d]) with the fitting coefficient assumed to have the best-fit value $C_0 = 5 \times 10^{-13}$ g cm^{-2} s^{-1}. Note the overall decrease in mass flux density with increasing resolution. Also note that as the resolution increases, the exponential rise at small radii becomes better defined.
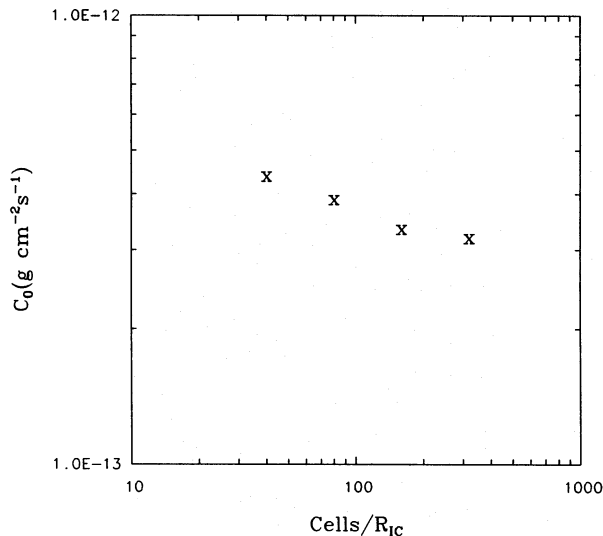
FIG. 27.—Convergence plot showing the change in the mass flux density fitting coefficient C_0 with spatial resolution. The curve is "turning over" for large numbers of cells. In the limit of infinite resolution, we predict a value of $C_0 \approx 3 \times 10^{-13} \, \mathrm{g \, cm^{-2} \, s^{-1}}$.

small radii. From this figure, we see that there is a reduction in the mass flux density as the spatial resolution is increased. It is not large, but it is noticeable. We have fitted each of the curves to the functional form in equations (5.2a)–(5.2d) and tabulated the values for C_0 in Figure 27. We see that although C_0 is decreasing with resolution, the result is converging. A rough estimate indicates that $C_0 = 3 \times 10^{-13} \, \mathrm{g \, cm^{-2} \, s^{-1}}$ is probably a better estimate of the mass flux density in the limit of infinite resolution. Meanwhile, for the case of $T_{\mathrm{IC}} \approx 10^8$ K, we estimate that $C_0 = 10^{-11} \, \mathrm{g \, cm^{-2} \, s^{-1}}$ is probably a better estimate in the limit of infinite resolution than the value $1.4 \times 10^{-11} \, \mathrm{g \, cm^{-2} \, s^{-1}}$ found for the models with a resolution of 40 cells per R_{IC}.

6.3. Optically Thin Approximation

Now we examine the validity of the optically thin assumption in our calculations. The primary sources of opacity in our models are electron scattering and bound-free absorption. We consider first the electron scattering contribution. In Tables 2–4 we show the optical depth from Thomson scattering for the three models shown in Figures 7, 14, and 15 ($L/L_{\mathrm{E}} = 0.3$, 0.08, and 0.01, respectively). The Thomson depth has been computed for rays originating from the origin with different inclination angles relative to

TABLE 2
ELECTRON COLUMN DENSITY ($L/L_{\mathrm{E}} = 0.3$)

Angle	N_e (cm^{-2})[a]	$f(r < R_{\mathrm{sp}})$	$f(r > R_{\mathrm{IC}})$
5.0......	9.1 (22)	0.94	0.02
15.0......	1.0 (23)	0.87	0.04
30.0......	1.4 (23)	0.75	0.05
45.0......	1.9 (23)	0.65	0.07
70.0......	3.5 (23)	0.57	0.06
75.0......	4.0 (23)	0.53	0.07
80.0......	4.5 (23)	0.52	0.09
82.0......	4.7 (23)	0.50	0.10
84.0......	5.7 (23)	0.42	0.21
86.0......	1.8 (24)	0.22	0.46

[a] $a(b) = a \times 10^b$.

TABLE 3
ELECTRON COLUMN DENSITY ($L/L_{\mathrm{E}} = 0.08$)

Angle	N_e (cm^{-2})[a]	$f(r < R_{\mathrm{sp}})$	$f(r > R_{\mathrm{IC}})$
5.0......	2.4 (22)	0.94	0.02
15.0......	2.8 (22)	0.86	0.05
30.0......	3.7 (22)	0.73	0.08
45.0......	5.3 (22)	0.63	0.09
70.0......	1.0 (23)	0.53	0.10
75.0......	1.1 (23)	0.49	0.11
80.0......	1.3 (23)	0.47	0.13
82.0......	1.7 (23)	0.46	0.15
84.0......	2.8 (23)	0.36	0.26
86.0......	6.3 (23)	0.23	0.41

[a] $a(b) = a \times 10^b$.

TABLE 4
ELECTRON COLUMN DENSITY ($L/L_{\mathrm{E}} = 0.01$)

Angle	N_e (cm^{-2})[a]	$f(r < R_{\mathrm{sp}})$	$f(r > R_{\mathrm{IC}})$
5.0......	3.1 21)	0.93	0.02
15.0......	3.5 (21)	0.84	0.08
30.0......	4.9 (21)	0.69	0.13
45.0......	7.4 (21)	0.58	0.16
70.0......	1.5 (22)	0.46	0.20
75.0......	1.7 (22)	0.41	0.23
80.0......	2.4 (22)	0.31	0.35
82.0......	3.0 (22)	0.25	0.44
84.0......	4.2 (22)	0.18	0.56
86.0......	7.8 (22)	0.10	0.70

[a] $a(b) = a \times 10^b$.

the rotation axis. As expected, the optical depth is smallest for rays nearly parallel to the rotation axis and largest for rays nearly tangent to the disk surface. The large jump in optical depth at large inclination angles is from rays actually intersecting the disk. For example, for $L/L_{\mathrm{E}} = 0.3$, this occurs near $4R_{\mathrm{IC}}$ ($2R_{\mathrm{IC}}$) for a ray inclined at $84°$ ($86°$) to the rotation axis. We have also computed in these tables the quantity $f(r > R_{\mathrm{IC}})$, which represents the fraction of the total scattering optical depth which results from distances greater than R_{IC} from the origin. For $L/L_{\mathrm{E}} = 0.01$, there is a large contribution from $r > R_{\mathrm{IC}}$ for smaller inclination angles because of the extended nature of the disk in this calculation. We have also tabulated in Tables 2–4 the fraction of the scattering optical depth which comes from radii inside the softening radius, $f(r < R_{\mathrm{sp}})$. Since our models are inappropriate inside R_{sp}, it is only the contribution outside R_{sp} which should be treated with confidence. Inside the softening radius, the flow is gravitationally bound and nearly hydrostatic, in which case analytic models such as those of Ostriker et al. (1991) would give a more accurate prediction of the structure than our models. However, we note that the optical depths we obtain from inside the softening radius are of the right order. Using our model parameters ($L/L_{\mathrm{E}} = 0.3$ and $T_{\mathrm{IC}} \approx 1.3 \times 10^7$ K) in the analytic work of Ostriker et al., we find the vertical optical depth at the softening radius ($R = R_{\mathrm{sp}} = 0.1R_{\mathrm{IC}}$) to be ≈ 0.07. Our numerical results give an optical depth for a nearly normal ray (inclination angle of $5°$) of 0.06. Certainly this degree of agreement is fortuitous, but we note that the model calculation performed with $R^*_{\mathrm{sp}} = 0.05 = R^*_{\mathrm{hot}}$ gives an optical depth for a nearly normal ray of 0.07. Thus, there

appears to be some precedent for the normal optical depths being relatively insensitive to the softening radius.

The optical depths in Tables 2–4 tend to scale approximately with L, as one would expect from equations (2.5) and (2.10). Also, although the models discussed assume $M_c = 10^8 \, M_\odot$, the optical depths are independent of the mass scaling. Thus, it appears that the optically thin approximation at least for Thomson scattering, is valid in the wind region of our models using the AGN spectrum with $L/L_E \leq 0.3$. The approximation is debatable in the corona inside the softening radius and in the disk itself, but even then it is only questionable for the high luminosity models ($L/L_E > 0.3$).

The other source of opacity to consider is bound-free absorption from species which have not been completely stripped of their electrons. To estimate this opacity, we have used our simulations to obtain the run of density and temperature as a function of distance along rays inclined at different angles to the rotation axis. We then use CLOUDY to calculate the ionization stages of the different species along the ray and sum up the results to obtain the total bound-free opacity. In Figure 28 we show the bound-free optical depth as a function of photon energy for two of our models ($L/L_E = 0.3$ and 0.01; Figs. 7 and 15, respectively). Each curve in this figure represents a ray with a different inclination. The sequence of inclination angles is exactly the same as that listed in Table 2, with the highest optical depth corresponding to the largest inclination angles. We note that the only rays for which there is appreciable optical depth are those which intersect the disk (i.e., inclination angles less than $\approx 84°$ for $L/L_E = 0.3$ and $\approx 80°$ for $L/L_E = 0.01$). Thus, in the wind region the material is sufficiently ionized and/or of small enough column density to present little optical depth. The fact that there is large bound-free opacity inside the disk, especially at photon energies between 10^2 eV and 10 keV, is not unexpected since the material is denser and cooler. Most of the opacity is caused by incompletely stripped stages of C, N, and O for photon energies between 100 eV and 1 keV and of Fe at around 10 keV. The dashed line in Figure 28 shows the bound-free optical depth obtained by ignoring the contribution inside

of the softening radius. The importance of the region inside the softening radius is rather minimal except at small inclination angles, where most of the material is located at small heights. For the rays which intersect the disk, the contribution from inside the softening radius is insignificant, so that the dashed lines lie right on top of the solid lines.

To summarize, then, it appears that the optically thin assumption is valid for all our models in the corona/wind region outside the softening radius. This is acceptable, since we do not claim validity for our models inside the softening radius. We would also predict that the wind and outer corona ($R^* > 0.1$) will not be seen in continuum absorption. Bound-free absorption is important in the disk, as one would expect.

To this point, we have concentrated on the opacity seen by the central X-ray flux; however, it is also important to consider whether the lines which provide the collisional cooling are effectively thin. It was pointed out by London, McCray, & Auer (1981) for the case of X-ray–illuminated stellar atmospheres that when the lines are effectively thick so that line photons will be collisionally quenched before escaping the system and can no longer provide a net cooling, the thermal equilibrium curve can be altered drastically. One example cited by London et al. exhibits a change in the pressure at the bottom of the transition region ($p_{c,\text{max}}$ in our notation) by a factor of 5 depending upon whether the line losses were included in the optically thin limit or ignored as is appropriate in the effectively thick limit. This change in base pressure can directly affect the magnitude of the mass flux generated by the wind.

Let $\epsilon = n_e C_{ul}/(A_{ul} + n_e C_{ul})$ represent the probability per absorption that a line photon is thermalized through a collisional de-excitation, where C_{ul} is the collisional deexcitation rate coefficient and A_{ul} is the spontaneous emission rate. Taking τ_0 to be the line center optical depth, then we say that if $\epsilon \tau_0 \gg (\ll)1$, then the line is effectively thick (thin). The optical depth at line center can be written as

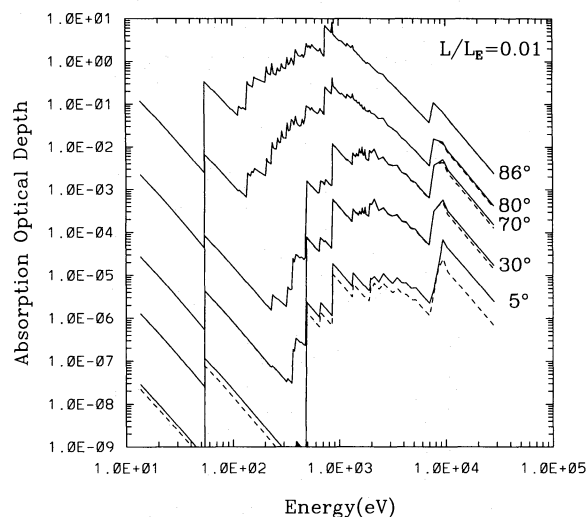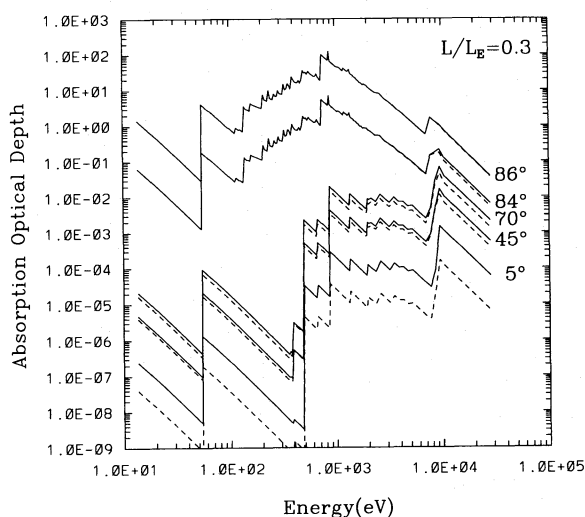$$\tau_0 = \frac{\pi^{1/2} e^2 f_{lu}}{m_e c \, \Delta v_D} N_l , \qquad (6.5)$$

FIG. 28.—Bound-free opacity as a function of energy along different rays for the case of $L/L_E = 0.3$ and $L/L_E = 0.01$ (both spectrum 1). Each curve is labeled by its inclination angle as given in Tables 2 and 4. The largest opacity rays have the largest inclination angles relative to the rotation axis. The dashed line is the contribution excluding the material inside of the softening radius, $R_{sp} = 0.1 R_{IC}$.

where f_{lu} is the oscillator strength, Δv_D is the Doppler width, and N_l is the column density of atoms in the lower state l. Using the expression $C_{ul} = 8.63 \times 10^{-6} \Omega/(\omega_u T^{1/2})$ cm^3 s^{-1}, where ω_u is the statistical weight of the upper state, and Ω is the collision strength, then

$$\epsilon\tau_0 = 1.29 \times 10^{-7} \frac{n_e \Omega}{A_{ul} \omega_u T^{1/2}} \frac{f_{lu}\lambda_0}{(2kT/m)^{1/2}} N_l , \quad (6.6)$$

where we have assumed $n_e C_{ul} \ll A_{ul}$ (a good approximation for the lines of interest here). Also, in equation (6.6) we have written the Doppler width as $\Delta v_D = v_{therm}/\lambda_0$, where λ_0 is the wavelength of the transition, and $v_{therm} = (2kT/m)^{1/2}$ is the thermal velocity of the ion in question.

We evaluate equation (6.6) for an important line, selecting conditions appropriate to the bottom boundary of our computational grid in order to assess the ability of the disk to trap this line. Along the bottom boundary, the ionization parameter is constant and given by $\Xi = \Xi_{c,max} e^{-0.5} \approx 24$. In thermal equilibrium under the optically thin approximation, the equilibrium temperature is $T \approx 4 \times 10^4$ K for the case of $T_{IC} = 1.3 \times 10^7$ K. For these conditions, line cooling is dominated by a resonant transition of O VI located at 1035 Å contributing approximately 48% of the total cooling. Taking $A_{ul} = 4.1 \times 10^8$ s^{-1}, $\Omega = 5.05$, $\omega_u = 6$, and $\omega_l = 2$, the oscillator strength $f_{lu} = A_{ul} \lambda_0^2 \omega_u/(0.667\omega_l) = 0.198$, and equation (6.6) becomes

$$\epsilon\tau_0 = 4.2 \times 10^{-30} \frac{n_e N_l}{T/4 \times 10^4} . \quad (6.7)$$

Given the definition of the ionization parameter $\Xi = F/cp$, the electron density in the disk along the bottom boundary can be written as

$$n_e = 2.99 \times 10^6 \left(\frac{T_{IC}}{1.3 \times 10^7}\right)^2 \left(\frac{L}{L_E}\right) \left(\frac{R}{R_{IC}}\right)^{-2}$$
$$\times \left(\frac{T}{4 \times 10^4}\right)^{-1} \left(\frac{\Xi}{24}\right)^{-1} M_{c8}^{-1} \text{ cm}^{-3} . \quad (6.8)$$

Let us consider the model shown in Figure 7 in which $L/L_E = 0.3$ and $T_{IC} = 1.3 \times 10^7$ K. Evaluating equation (6.8) at a radius of $4R_{IC}$, the electron density at $T = 4 \times 10^4$

K and $\Xi = 24$ is 5.6×10^4 cm^{-3}. In estimating the column density N_l, we consider a vertical column in the disk (contribution from corona and wind to the line opacity is negligible) and assume that all the oxygen is in the ground state of O VI with an abundance relative to hydrogen of 8.51×10^{-4}. The height of the disk is $h \approx 0.4R_{IC}$ (Fig. 7), so that $N_l \approx n_{O VI} h \approx 1.2 \times 10^{20}$ cm^{-2}. From equation (6.7), we see that $\epsilon\tau_0 \approx 2.8 \times 10^{-5} \ll 1$, so the disk is effectively thin in this important radiator. Both n_e and N_l are functions of radius, and therefore so is $\epsilon\tau_0$. If we take the height of the disk to be a constant fraction of the gravitational scale height, then $h \propto R^{3/2}$ (see eq. [4.10]), and $\epsilon\tau_0 \propto R^{-2.5}$. Therefore, the disk becomes increasingly thicker to lines at smaller radii. In fact, $\epsilon\tau_0 \approx 1$ for $R \approx 0.06R_{IC}$, which is inside the softening radius of $0.1R_{IC}$. Therefore, we can be confident that our use of the optically thin line cooling in determining the net radiative loss is valid. However, given that $n_e \propto M_{c8}^{-1}$ and column density is independent of central object mass (see earlier discussion), a 1 $M_\odot$ object would possess $\epsilon\tau_0 \approx 2.8 \times 10^3 \gg 1$. Therefore, the disk would be effectively thick in the lines, significantly reducing the contribution from line cooling and increasing the base pressure from that determined in the optically thin limit.

6.4. Iron Kα Lines

It has been recently found in some AGNs that iron Kα emission is observed (see Koyama et al. 1989; Marshall et al. 1993; Ueno et al. 1994). We compute the column density of iron along rays to the central object which are inclined at different angles to the rotation axis. The calculation is performed by taking the density and temperature structure of the wind and using CLOUDY to perform ionization equilibrium calculations at every point in the model, assuming the radiation is unattenuated from the central source. We have performed this calculation assuming a solar abundance of iron of 4.68×10^{-5} (Grevesse & Anders 1989). Column densities are calculated for two models with $T_{IC} = 1.3 \times 10^7$ K, $L/L_E = 0.3$ (Fig. 7) and $L/L_E = 0.01$ (Fig. 15). No attempt has been made to extrapolate a contribution to the column density from regions outside the computational domain. The results are summarized in Figure 29, where we show the column density as a function of ionization state for
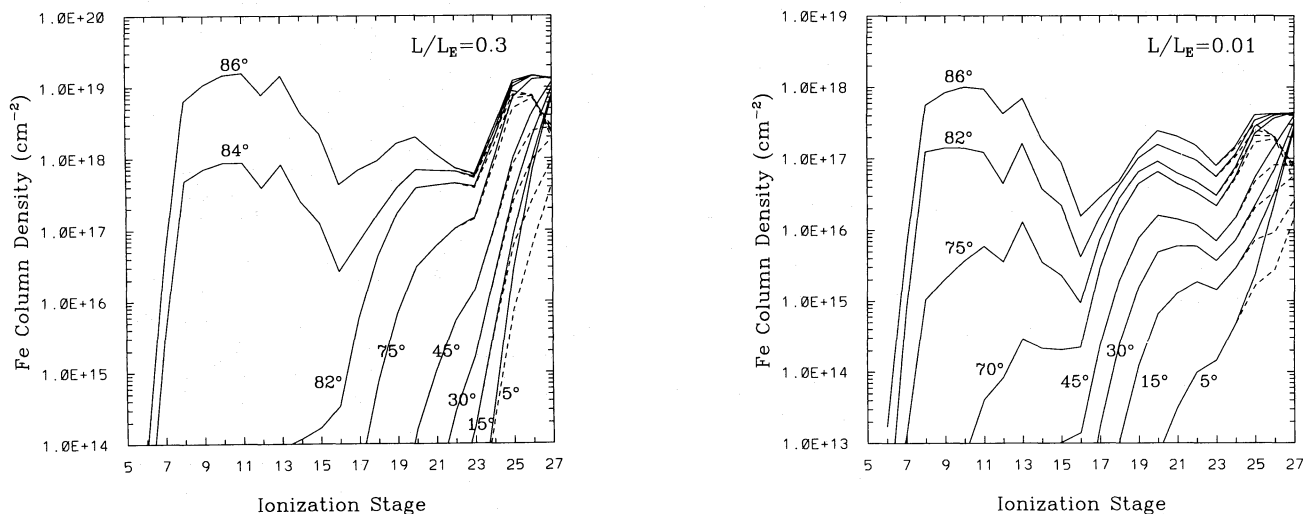

FIG. 29.—Column density of different ionization stages of iron for $L/L_E = 0.3$ (see also Fig. 7), and $L/L_E = 0.01$ (see also Fig. 15). Each curve is labeled by its inclination angle as given in Tables 2 and 4. The dashed lines show the column density excluding the region inside the softening radius, $R_{sp} = 0.1R_{IC}$.

rays with various angles of inclination. We find that the column density of the highly ionized ions depends critically on the density structure at small radii. Given that our results must be considered suspect at small radii due to our use of the softening radius for the gravitational potential, it is necessary to identify the magnitude of our uncertainty. To delineate this region, we have also plotted in this figure (*dashed line*) the column density obtained when one ignores the contribution inside the softening radius. Thus, the results excluding the inner region can be viewed as lower limits to the true column density. Our results suggest that H-like and, to a lesser extent, He-like Fe are probes of the inner ($R \lesssim 0.1R_{IC}$) corona. Thus, we cannot make any predictions for these ions using our models. It appears, though, that for Li-like and above, the contamination from the inner corona is probably minimal, and our results should be valid.

At small inclination angles (i.e., looking nearly down the rotation axis), we see only the high ionization state material because most of the material is at the Compton temperature. As the inclination increases, contributions from lower ionization stages arise as the line of sight runs through the vigorous wind region. Finally, at large inclinations (i.e., 86° for $L/L_E = 0.3$ and $\gtrsim 75°$ for $L/L_E = 0.01$), the line of sight intersects the disk, giving rise to large column densities of low ionization state material.

Comparing the results from the two luminosities, we find that the column density of the high ionization stage material goes down nearly linearly with the luminosity. This is because the density at the base of the corona is proportional to the luminosity through the ionization parameter [i.e., $p = L/(4\pi r^2 \Xi_{c,\max})$]. The low-luminosity case also has an appreciable fraction of C-like and N-like material at intermediate inclinations. In particular, for an inclination of 45° there is an N-like column density of $\approx 2 \times 10^{16}$ cm^{-2} for $L/L_E = 0.01$, while it is only $\approx 2 \times 10^{14}$ cm^{-2} for $L/L_E = 0.3$. Thus, there is the potential for discerning information on the luminosity from the presence of N-like ions at low luminosity.

In theory, one would like to calculate line profiles from our models to make predictions of line shifts and/or asymmetries which would identify the presence of a wind. This is outside the scope of the present paper. We can, however, make some simple predictions. First of all, since the K-shell photoionization cross section is roughly 2×10^{-20} for Li-like through Na-like ions of Fe (Band et al. 1990), the column densities predicted are insufficient to produce a noticeable K-edge in the spectrum. A possible exception to this statement may be the H-like and He-like ions at small radii, $R \lesssim R_{sp} \approx 0.1R_{IC}$. Another prediction to consider is that of Kα emission lines which Band et al. have shown to arise from not only fluorescence following a K-shell ionization, but also from resonant scattering of the continuum from the central source. The line center cross section is $\pi^{1/2}e^2 f_{lu}/(m_e c \Delta \nu_D)$, where f_{lu} is the oscillator strength and $\Delta \nu_D$ is the Doppler width. Assuming an oscillator strength of $f_{lu} = 0.4$ (Band et al. 1990) and a temperature of 10^7 K, one obtains a cross section for absorption of 2.3×10^{-17} cm^2. Thus, for column densities of order 4×10^{16} cm^{-2}, an ion will be an efficient scatterer of the continuum. Given our computed column densities, we see that there is ample depth for resonant scattering of the radiation from the central source for many ionization states. We will address the problem of predicting detailed line diagnostics for our models in a later paper.

7. SUMMARY

We have performed two-dimensional, axisymmetric hydrodynamical calculations of X-ray–heated winds from accretion disks for a range of luminosities. In our calculations we have used two spectra indicative of AGNs possessing Compton temperatures of 1.3×10^7 K and 10^8 K. Radiative heating and cooling is taken to be optically thin. We have provided detailed discussions of our solutions, particuarly in terms of the shape of the Mach surface and the mass flux density at the disk surface. Typically, the Mach surface is at large heights ($\gtrsim R_{IC}$) for flow emanating from small radii, indicative of gravitationally inhibited flow. At larger radii there is a nearly discontinuous change in the Mach surface to low heights ($\lesssim R_0$), which then increases linearly with radius; the details of this transition are a function of luminosity and Compton temperature (e.g., eq. [5.4c]). At high luminosities, both the high and low Compton temperature models yield a mass flux density which varies as R_0^{-2}, while at low luminosities there are differences between the two sets of models. For the higher (lower) Compton temperature case, $\dot{m} \propto R_0^{-1.7}$ ($\dot{m} \propto R_0^{-1}$) at large radii and low luminosities. We find that the flow geometry may play an important role in the difference between the high- and low-T_{IC} behavior. In addition, our definition of the disk interface (i.e., $T_{c,\max}$) may contribute to this difference, since for the low-T_{IC} case the maximum temperature reached along a streamline is only a few times $T_{c,\max}$ at low luminosities and large radii.

We have found the flow topology in the wind to be different than expected in that flow tubes could become compressed and turn radial at small heights above the disk. This is the result of increased importance of the radial pressure gradient at high temperatures. Because the magnitude of the radial pressure gradient relative to gravity increases with radius, we can see evidence of increased compression with radius. Thus, the flow geometry is not homologous in the sense that the flow at large radii cannot be represented through a simple rescaling of a tube at smaller radii.

We have compared our results to the analytic predictions of Begelman et al. (1983) for Compton-heated winds. We have provided in § 4 a slightly modified version of the BMS theory as represented by the radius-luminosity parameter space plot in Figure 5. The primary difference is that the boundaries between the different wind regimes are provided by a continuity of the mass flux density argument, rather than the simple physical arguments of BMS (namely, $T_{ch} = T_{IC}$ for the isothermal wind, and heating timescale equal to gravitational timescale for the gravity-inhibited wind). We have also provided a new mass flux density formula (eq. [4.8]) for the analytic theory which provides for rapid transition between the different solution regimes depicted in Figure 5. Because of our inclusion of non-Compton processes in the heating and cooling, and the implicit assumption of BMS that the coronal temperatures are significantly larger than the disk temperatures (i.e., $T_{c,\max}$), we found a direct comparison inappropriate for our low-T_{IC} model, except at high luminosities and small radii, while for the high-T_{IC} case the restrictions were much less severe.

We have constructed radius-luminosity parameter space plots of our numerical results similar to that in Figure 5 for both the high- and low-T_{IC} cases (Figs. 24 and 17, respectively). Overall, these plots compare quite favorably to the analytic predictions, especially the high-T_{IC} case. We feel that we have identified the five solution regimes dis-

cussed by BMS. For the high-T_{IC} case, there appear to be only three noticeable differences between our numerical results and the analytic prediction, namely, (1) the location of the corona/wind interface, (2) the boundary between region B (steadily heated free wind) and region C (gravity-inhibited wind), and (3) radial dependence of the mass flux density in region C. Of these three, the last is most significant, but there are several caveats to consider. Numerically, we find a radial dependence in region C of $\dot{m} \propto R_0^{-2}$, however, this is somewhat uncertain in the high-T_{IC} case because of the large amplitude of spatial oscillations in the mass flux density owing to the presence of vortex structures near the disk interface. The lowest luminosity models provide the largest baseline by which to measure the slope of this region; however, computational demands of low-luminosity models make a definitive calculation prohibitive at this time, even with adaptive mesh refinement. In addition, the lowest luminosity models allow the influence of non-Compton heating and cooling terms. So even if a lower luminosity model could be performed, it is not clear that the resulting mass flux density should agree with the analytic prediction of $\dot{m} \propto R_0^{-1}$. However, we note that in the low-T_{IC} models in which the extra heating and cooling terms are already operative, our results also favor a $\dot{m} \propto R_0^{-2}$ behavior. Finally, there is also the possibility that, due to the slow variation with luminosity of the ratio of gravitational timescale to heating timescale, the analytic prediction of region C may not be evident until much smaller luminosities than we have sampled. The slight change in slope to $\dot{m} \propto R_0^{-1.6}$ in our lowest luminosity model ($L/L_E = 0.002$) in region C is suggestive. As such, the numerical results at lower luminosities sampled in this work may still show the $\dot{m} \propto R_0^{-1}$ dependence predicted by BMS for region C.

We have provided numerical formulae for the mass flux density as a function of radius and luminosity (eqs. [5.2] and [5.4]). The total mass flux can be predicted by integrating over the surface of the disk, provided one knows the radial extent of the disk and assuming that edge effects associated with the truncation of the disk are unimportant so that smaller disks are approximated by our simulations. In comparing with the analytic prediction, we find excellent agreement in the mass flux density at large luminosities in both the high- and low-T_{IC} cases. The agreement becomes worse as the luminosity is decreased. Even still, over our range of luminosities ($0.3 \geq L/L_E \geq 0.002$) we typically find the numerical result to be within about a factor of 2 of the analytic prediction for the high-T_{IC} case. For the low-T_{IC} case, the agreement is a little worse but is still within about a factor of 3 for the luminosities studied ($1.0 \geq L/L_E \geq 0.0025$). This level of agreement for the low-T_{IC} case seems to indicate that the mass flux density is rather insensitive to the details of the heating and cooling mechanisms. We find also that the peak in the mass flux density occurs near a radius of $0.25R_{IC}$, which is near the corona/wind boundary and is very similar to the prediction of Shields et al. (1986) that it would occur at approximately $0.15R_{IC}$.

Finally, we emphasize that our models evolve to a steady wind pattern, in contrast to the work of Melia and coworkers. Their work suffers, however, from the use of an unphysical boundary condition whereby highly supersonic material is injected into the region in which the material is gravitationally bound and should be extremely subsonic. In either case, the instability they find is the result of radiative transfer effects (presumably shadowing) which have not been included in our model. However, in the work of Murray et al. (1995) we have also removed the optically thin approximation by including flux-limited radiative diffusion. These calculations of finite-size disks were made in order to make specific comparisons with low-mass X-ray binaries and showed no signs of radiative instabilities.

APPENDIX

We describe in this Appendix some of the features of our numerical method used in solving the system of equations (2.14)–(2.21). We utilize a two-dimensional second-order Godunov method which employs local adaptive mesh refinement. To this two-dimensional hydro scheme we have added the effects of rotation, gravity, and heating and cooling. Since including source terms in a Godunov method can be rather involved, we discuss below some of the aspects of the hydrodynamical method and our prescription for including momentum and energy sources. We also describe briefly some of the test problems to which we have applied our code.

A1. ADAPTIVE MESH REFINEMENT

Owing to the hyperbolic nature of the equations of hydrodynamics, it is possible to solve these equations in one part of the grid, which could be finely zoned, nearly independent of the solutions in other parts of the grid, which could be coarsely zoned. Recently, Berger & Colella (1989) have developed a method known as adaptive mesh refinement (AMR) that takes advantage of this finite propagation speed of the characteristics. This method has recently been implemented for astrophysics by Klein et al. (1990, 1994) and is used in our calculations. By using AMR, we can focus in on arbitrary regions to obtain unprecedented detail while keeping the total computation time at manageable levels. The first part of the algorithm establishes the criteria for grid refinement using a Richardson-type error estimation of the local truncation error. The results on a given grid are first coarsened in space to form a grid with cells twice as large as the original grid. The larger cells are then advanced one time step, which is twice as large as that taken on the original grid. These results are then compared to those obtained on the original grid by integrating two time steps. Those cells which are deemed to be poorly resolved are tagged,

and a boxing algorithm is employed to form efficient rectangular grids encompassing the tagged cells. A new set of grids is then generated through conservative interpolation on to n_{ref}^2 new fine cells for each coarse cell, where n_{ref} is the refinement factor in a given spatial direction.

The advancement of a coarse time step for the entire grid can be described as follows. First, all the cells on the coarsest level are advanced one time step. The next level grids are then advanced n_{ref} time steps using the current boundary value data that exist at that time. Once the fine cells have been advanced to the same time as the coarser cells, some fix-ups are performed on the coarser mesh. That is, those coarse cells which overlie finer cells have their values replaced by the conservative average of the finer cells. This then destroys conservation across a coarse/fine interface, since the flux across this interface was not the same on both levels. Using the fine-level data, the conservatively averaged flux on the coarse level across the coarse/fine interface is then computed, and the correction to bordering coarse cells is applied to maintain conservation. The same procedure can then be applied recursively to finer levels.

Typically, in our calculations three levels are employed with a refinement factor between levels of $n_{ref} = 4$ in each linear dimension. This means that there are 256 level 3 cells for each level 1 cell that is refined. Since the time step goes down because of the Courant condition with each refinement, there are n_{ref}^2 level 3 time steps required to advance each level 1 cell one time step. Consequently, there are 4096 level 3 cell advancements required of a single coarse cell time advancement, for $n_{ref} = 4$. Obviously, it is imperative to keep the level 3 cell count to a minimum in order to provide both reasonable time and memory limits for the calculation.

There is a word of caution to using AMR on our particular problem which should be discussed. This has to do with the existence of the intermediate-temperature stable equilibrium solution in Figure 2. Since AMR must at times introduce finer solutions from coarser solutions through conservative linear interpolation, there could be times when performing refinement around the disk/corona interface will produce temperatures in the finer cells corresponding to the stable intermediate solution in Figure 2. When the disk/corona interface is much smaller than a fine cell (i.e., at small radii in the static corona), this can lead to a spurious result. What happens is that an intermediate temperature is initially assigned to a cell because of the interpolation process which may be close to the intermediate stable equilibrium. As a result, the numerical solution will tend to stay at this intermediate solution rather than going to either the cool disk temperature or the Compton temperature, which a more accurate means of interpolating on to the finer mesh would have ensured. To prevent this from happening, we make it a rule to always refine the inner parts of the disk/corona interface from start of the calculation. This allows us to assign the correct temperature to these fine cells without relying on an interpolation procedure.

A2. HYDRODYNAMICS

The two-dimensional hydrodynamics is solved using the time-splitting technique of Strang (1968). That is, we perform one-dimensional explicit hydrodynamics in each direction separately in a given time step and then reverse the order in the next time step. This provides second-order accuracy in time when the two time steps are equal. To facilitate the discussion of our method for including sources in the hydrodynamics, we will necessarily describe some of the aspects of the Godunov method. The advantage of the Godunov method is in its ability to preserve jump conditions around shocks without diffusing the jump over many computational cells. More detailed discussions can be found in Van Leer (1979), Colella & Woodward (1984), and Colella & Glaz (1985). The discussion below applies only to the solution of the hydrodynamic equations (2.14)–(2.18) excluding the source terms on the right-hand sides of these equations.

The essence of the Godunov technique is to advance volume-weighted averages of the conserved quantities (i.e., mass, momentum, and energy densities) by conservatively differencing fluxes located at cell interfaces which represent accurate values at the half–time step. The unique part of this technique is in the method by which the fluxes at the cell interfaces are determined. The state of the gas at a zone edge at the half–time step is obtained from the solution of a Riemann problem in which the left- and right-hand states are determined from "appropriate" averages over the time step. These states require the construction of piecewise linear interpolants (second-order; the piecewise parabolic method [PPM] constructs parabolic interpolants). The slopes for the linear interpolants are calculated using values from nearby cells to construct a central difference approximation which is fourth-order accurate in regions of smooth flow. The slopes are also subjected to monotonicity constraints (Van Leer 1979) to help reduce numerical ringing near points of local maxima and minima. The effective left and right states for the Riemann problem are constructed by averaging the quantities over the spatial domains which can interact with a zone edge over a given time step. In an Eulerian calculation, the number of characteristics which intersect a zone edge from a given side can range from zero to three, depending on the flow velocity. Following Colella & Woodward (1984) and Colella & Glaz (1985), we have included the corrections to properly account for only those characteristics which cross a zone edge in a given time step. The Riemann problem is solved using the approximate Riemann solver described by Colella & Glaz (1985). Once the interface values are computed from the Riemann solution, the fluxes and pressure gradient force are differenced conservatively to advance the conserved quantities to the next time step.

In the spit version of the two-dimensional problem, the one-dimensional sweep ignores those terms which involve differencing in the orthogonal direction. That is, during an $R(Z)$ sweep all terms involving $\partial/\partial Z*(\partial/\partial R*)$ are ignored. Thus, the momentum equation for the orthogonal components in a given one-dimensional sweep is simple advection. The rotation equation (eq. [2.17]) is correctly handled then (except for the source term) by simple advection in the direction of each sweep.

A3. INCLUSION OF MOMENTUM AND ENERGY SOURCES

We experimented with a number of different methods for including the source terms in the momentum and energy equations. These source terms arise from rotation, gravity, and various heating and cooling mechanisms. The simplest way to treat these terms is to split them off from the rest of the hydrodynamics. That is, perform an R-sweep followed by a Z-sweep

ignoring the source terms, then update the momentum and energy densities by the source terms using a second-order method such as a simple predictor-corrector scheme. On the next time step, the order is reversed with the updating of the source terms performed first followed by the hydrodynamical sweeps in the Z and R directions. This is the simplest method to implement, but unfortunately it can yield undesirable results in both our test problems and the real problem. We discuss the comparison of our numerical simulations to test problems below, but we note from our experience that the rotation source terms do not in general present a problem, except in trying to obtain accurate solutions near the rotation axis. That is, they appear to work equally well whether or not they are split off from the hydrodynamics.

A3.1. *Gravity*

Including gravity accurately was found to be difficult, particularly when a goal of our numerical solution is to have a region which is in near hydrostatic balance between the outward pressure gradient and the inward gravitational acceleration. Given this fact, it was necessary to include the effects of gravity in the same hydrodynamic sweep which was computing the pressure gradient. There are a number of different ways one could do this, including that discussed by Colella & Woodward (1984). However, we have chosen a slightly simpler procedure which seems to work well for our problem. First we calculate the gravitational acceleration at cell centers for a given one-dimensional sweep. Slopes are then computed across each cell following the same procedure we use for the hydrodynamic variables, i.e., using fourth-order central differences. Then we include gravity for the prediction of the pressure of the left-hand state of the interface between the j and $j + 1$ cell by adding the quantity $0.5 \Delta t \rho_j c_j \{g_j + \Delta g_j [1 - \max (v_j + c_j, 0) \Delta t / (2 \Delta x_j)]\}$, where the time step is Δt, v_j is the velocity in the direction of the one-dimensional sweep, c_j is the adiabatic sound speed, g_j is the cell-centered gravitational acceleration in the direction of the sweep, Δg_j is the computed slope of the gravitational acceleration, and Δx_j is the width of the cell in the direction of the sweep. Similarly, for the right-hand state we add the term $-0.5 \Delta t \rho_{j+1} c_{j+1} \{g_{j+1} - \Delta g_{j+1} [1 + \max (v_{j+1} - c_{j+1}, 0) \Delta t / (2 \Delta x_{j+1})]\}$. Since the primary requirement is that the addition of the source term be included in a way that will satisfy the characteristic equations ($du \pm dp/\rho c = g \, dt$; see Colella & Woodward 1984) at the half–time step, we could have added the gravity to either the velocity or the pressure prediction. We chose to include the gravitational source in the pressure in a desire to obtain hydrodynamic solutions which would be nearly hydrostatic in regions in which the gravitational force was strong. However, as we discuss below, we have also tried putting the gravity in the velocity prediction and have found comparable results. Gravity must also be included in the corrector step where the fluxes of the mass, momentum, and energy densities at cell interfaces at the half–time step are differenced. Therefore, we increment the momentum density by the quantity $\Delta t \rho_j^{n + 1/2} g_j$, where $\rho_j^{n + 1/2}$ is the cell-centered density at the half–time step. Here again we have some freedom in that the $\rho_j^{n + 1/2}$ can be obtained to second-order accuracy by space averaging the cell edge densities at the half–time step obtained from the Riemann solution or time averaging the densities at cell center. We have tried both but have found the time averaging of the densities at cell center to give noticeably better results near the disk interface.

Finally, we note that since we have defined the total energy density by including the gravitational potential, there is no gravitational source term for the energy equation. Including the gravitational potential in the total energy density can, however, lead to numerical problems in regions in which the gravitational energy is dominant over thermal energy. This is particularly true with the adaptive mesh refinement capability of our code. If during the course of a calculation a fine mesh must be generated from a coarse mesh in a region in which gravitational energy dominates, the thermal energy density may be poorly determined, leading to spurious results. Therefore, we required that in this region the finest mesh exist from the beginning of the simulation.

A3.2. *Rotation*

The rotation source terms in the R and ϕ momentum equations have been included in the Godunov method. However, unlike the gravitational term, we have found that splitting off the rotational terms works nearly as well as including them in the Godunov method directly. As such, the precise manner in which they are added is less important. For reference, we have followed the same procedure as we did for gravity, where we replace the force term g_j with $-v_{\phi j}^2 / R_j$ for the R-momentum equation and $-v_{R j} v_{\phi j} / R_j$ for the ϕ-momentum equation. The propagation speed is the advection velocity, rather than $v \pm c$. The predictor part is added to the left- and right-hand states of the pressure rather than the velocity. This preference is based upon wanting to achieve a balance between rotation and gravity in the cool disk. In adding the source term to the corrector step, we update the density first and multiply the time-averaged density at cell center by the time-averaged centrifugal and centripetal force terms in the R- and ϕ-momentum equations. It is best again to avoid the space averaging in the corrector because of the problems produced around the disk interface when two cells can differ by orders of magnitude in the density. Finally, we note that the ϕ-momentum equation could have been cast in an angular momentum form and avoided the necessity of worrying about a source term. We have found that this formulation produced inferior results near the rotation axis. We believe this is caused by piecewise linear interpolants formed of the conserved quantities. When the quantity is $R v_\phi$, this indicates that v_ϕ is really approximated by a zeroth-order function. This can be a very poor approximation near the rotation axis, where v_ϕ may be changing rapidly with radius. Thus, it is best to treat the ϕ-momentum equation in the form shown in equation (2.17).

A3.3. *Energy*

The heating and cooling are split off from the hydrodynamics in the following sense. First, the hydrodynamics is solved, without heating and cooling, first in the R-direction, followed by the Z-direction. Then we perform an energy update by computing the change in the thermal energy density due to heating and cooling for each cell. On the next time step, the order is reversed with energy addition performed first, then the hydrodynamics is computed in the Z-direction, followed by the R-direction. Over two equal time steps, this provides a second-order accurate method of incorporating the energy addition. In

the energy addition step, it is only the thermal energy density which is allowed to change. Thus, the version of equation (2.18) which is actually solved during this step is

$$\frac{dT^*}{dt^*} = \left(\frac{2}{3}\right)\rho^*[\Gamma^*(\Xi^*, T^*) - \Lambda^*(\Xi^*, T^*)] \,, \tag{A1}$$

where we have used the fact that ρ^* is constant during the energy update. We solve this energy equation implicitly to correctly handle the stiffness one expects at both disk and Compton temperatures, where the heating and cooling can balance to high degrees. We perform a backward Euler integration and solve the nonlinear finite difference equation using a Newton iteration. As described in § 2, the heating (Γ) and cooling (Λ) functions are taken from CLOUDY. As such, we tabulate these terms as functions of ionization parameter and temperature. We use piecewise bicubic Hermite polynomials to perform interpolation in the table and to calculate the partial derivatives required in the Newton iteration. In theory, the backward Euler solution of equation (A1) need not be solved on the same time step as the hydrodynamics. Rather, we have the option to solve, if necessary, this equation on a finer timescale. We have experimented by subdividing the energy update into a sequence of smaller steps to improve accuracy. We find this improvement to be negligible for our simulations; therefore, we routinely take the time step here to be the same as the hydrodynamic time step. (In other words, changes in the thermal energy density are usually small over a hydrodynamic time step.) Another way of guaranteeing an accurate energy solution is to institute control over the entire time step (i.e., hydro plus energy update) associated with the fractional change of the thermal energy density. However, given that we usually end up refining around regions which are changing quickly and therefore have smaller time steps, this control usually does not come into play.

A4. TEST PROBLEMS

We have compared our code to three different test problems, the first of which is a quantitative comparison, while the other two problems are more of a qualitative test. The first problem tests the addition of rotation in our code by comparing our results with the similarity solutions of Low (1985) for adiabatic, axisymmetric, rotating gases. Low has found a class of solutions based on the similarity variable $\zeta = r/F(t)$, where r is the spherical radius and $F(t)$ is the evolutionary function $F(t) = [c(t - t_0)^2 + \alpha/c]^{1/2}$, where c, α, and t_0 are constants. Interpretation of the similarity solutions indicates that the constant c controls the magnitude of the late-time (asymptotic) speed, while α dictates the radial acceleration of the flow. For $\alpha, c > 0$, t_0 represents the point of maximum compression. For $t < t_0$ ($t > t_0$), the flow is radially inward (outward). (See Low for a more detailed discussion of these parameters.) In testing our code, we have focused on a particular subset of the solutions described by Low, namely, the case of solid-body rotation and uniform-entropy density (i.e., the entire flow is characterized by a single value of the entropy density). The solid-body rotation description applies to the rotational velocity in terms of the similarity variable. Assuming an angular velocity ω_0, the azimuthal velocity is given by

$$v_\phi = \omega_0 R/F^2(t) \,,$$

where R is the cylindrical radius coordinate. Note that this implies that the rotation is solid body at any given instant in time but that the magnitude changes with time due to the evolutionary function $F(t)$. Because $F(t)$ is a minimum at $t = t_0$ for α, $c > 0$ (the parameter regime investigated here), at the time of maximum compression the gas is spinning fastest, and $v_\phi \to 0$ at $t \to \pm \infty$. After some manipulation, the solution of Low can be converted to cylindrical coordinates and nondimensionalized to elicit the essential parameters to the problem. This solution has the form[16]

$$v_\phi^* = R^* F^{-2}(t^*) \,, \tag{A2}$$

$$v_R^* = R^* c^* (t^* - t_0^*) F^{-2}(t^*) \,, \tag{A3}$$

$$v_Z^* = Z^* c^* (t^* - t_0^*) F^{-2}(t^*) \,, \tag{A4}$$

$$\rho^* = \left\{ F^2(0)F^{-2}(t^*) + 0.6\chi \frac{(\alpha^* - 1)}{F^2(0)F^2(t^*)} \left[1 - \frac{F^2(0)}{F^2(t^*)} \left(R^{*2} + \frac{Z^{*2}\alpha^*}{\alpha^* - 1} \right) \right] \right\}^{3/2} \,, \tag{A5}$$

$$p^* = \left\{ F^2(0)F^{-2}(t^*) + 0.6\chi \frac{(\alpha^* - 1)}{F^2(0)F^2(t^*)} \left[1 - \frac{F^2(0)}{F^2(t^*)} \left(R^{*2} + \frac{Z^{*2}\alpha^*}{\alpha^* - 1} \right) \right] \right\}^{5/2} \,, \tag{A6}$$

where the spatial coordinates have been scaled relative to the fiducial radius R_0; time is scaled relative to the rotation time $T_0 = \omega_0^{-1}$; velocity is scaled relative to the rotation velocity at R_0, i.e., $v_0 = R_0 \omega_0$; density and pressure have been scaled relative to their value at the fiducial radius R_0, i.e., ρ_{R_0} and p_{R_0}, respectively, and χ is a parameter representing the ratio of rotational kinetic energy to thermal energy density at the fiducial R_0, i.e., $\chi = [(1/2)\rho_{R_0} R_0^2 \omega_0^2]/[(3/2)p_{R_0}]$. The evolutionary function $F(t^*)$ is now given by

$$F(t^*) = [c^*(t^* - t_0^*)^2 + \alpha^*/c^*]^{1/2} \,, \tag{A7}$$

where $c^* = c/\omega_0^2$, and $\alpha^* = \alpha/\omega_0^2$. The constant $t_0^* = t_0/T_0$ is set by the specification of the velocity v_{R_0} at the fiducial radius R_0,

---

[16] There appear to be typographical errors in this paper: equations (33) and (34) for uniformly rotating, isentropic flow should be of the form $P = 2/5 s_0^{-3/2}[(a_0 - W)/2]^{5/2}$ and $D = s_0^{-3/2}[(a_0 - W)/2]^{3/2}$, respectively.

so that

$$t_0^* = \frac{-v_0}{2v_{R_0}} \left\{ 1 \pm \left[1 - \left(\frac{2v_{R_0}}{v_0} \right)^2 \frac{\alpha^*}{c^{*2}} \right]^{1/2} \right\}. \tag{A8}$$

Note that if $v_{R_0} < 0$ ($v_{R_0} > 0$), then $t_0^* > 0$ ($t_0^* < 0$), and the point of maximum compression is in the future (past). There are two solutions for t_0^* because a given velocity can occur at late time as the overall flow slows down, or near the point of maximum compression. Thus, we find that the similarity solution given by equations (A2)–(A8) is completely specified by the four parameters $\alpha^*, c^*, v_{R_0}^* = v_{R_0}/(R_0 \omega_0)$, and χ. We note that for $\alpha^* > 1$ the density and pressure contours form ellipses, while for $\alpha^* < 1$ they appear as hyperbolae.

   As a test of our code, we have performed a simulation whereby the initial conditions are given by equations (A2)–(A8) at time $t^* = 0$. The calculation is performed in cylindrical coordinates using reflecting boundary conditions along the R and Z axes and the similarity solution as the outer boundary conditions. In Figure 30a we present the measured error from a calculation in which $\alpha^* = 4, c^* = 1, \chi = 0.5$, and $v_{R_0}^* = -0.01$. We have chosen the plus sign in equation (A8) so that $t_0^* \approx 100$. The error plotted in Figure 30 is for the five conserved quantities, namely, $y = (\rho, \rho v_R, \rho v_z, \rho \epsilon, \rho v_\phi)$. The quantity plotted is a relative error given by

$$\text{Error } [y(t)] = \left\{ \sum_{i=1}^{N} [y_i^{\text{num}}(t) - y_i^{\text{anal}}(t)]^2 \right\}^{1/2} \bigg/ y_{\text{max}}(t) ,$$

where the sum is over the N cells of the calculation, and y_{max} is the maximum absolute value of that quantity over the grid. Admittedly this underestimates the error somewhat, but it gives a better measure of the accuracy than summing relative errors, since near the rotation axis the radial and azimuthal velocities become small. This calculation was performed on a 50×50 grid. We see that the agreement is exceptional, especially for the density. The worst component, as expected, is ρv_ϕ, where the error is fairly constant in time and several orders of magnitude higher, but still acceptable. This model has been evolved up until the point of maximum compression ($t^* \approx 100$). Over this time, density has grown by over 5 orders of magnitude, while ρv_ϕ has increased by over 8 orders of magnitude. Thus, we seem to provide good accuracy over a large dynamic range. There is a problem, however, during the expansion phase. An example of this is shown in Figure 30b, where we have let $v_{R_0}^* = 0.1$ and $t_0^* \approx -9.6$ (all other parameters are as they were in Fig. 30a). For this model, the point of maximum compression is in the past and the gas is now in its expansion phase. Note that the errors are again very small and are fairly constant with time except for the error in ρv_ϕ which, although small, is growing in time. This appears to be a general problem in the expansion phase. That is, regardless of whether the rotational source term is split off from the rest of the hydrodynamics or is incorporated into the Godunov package, the error in ρv_ϕ grows in time during this part of the calculation. Different implementations of the rotation inside the Godunov hydrodynamics package all seemed to show growth in the error of ρv_ϕ, although the magnitude of the error varied among our various attempts. An important characteristic of our best models is the manipulation of the rotational source term (right-hand side of eq. [2.17]) included in the predictor and corrector parts of the Godunov method. Some simple analysis has shown, and our numerical results agree, that we obtain superior agreement if the $1/R$ part of the source term is written as $(1/R)_{k+1/2} = R_k R_{k+1}/R_{k+1/2}^3$, where $R_{k,k+1}$ are the locations of the cell interfaces, and $R_{k+1/2} = (R_k + R_{k+1})/2$ is the midpoint of the cell. Although this implementation reduces significantly the error in ρv_ϕ over
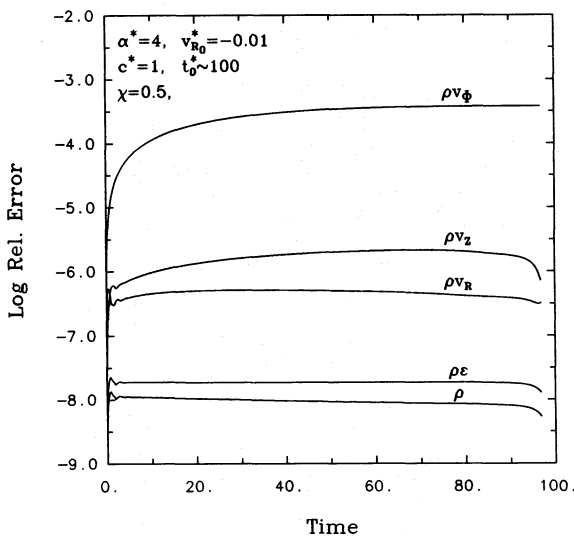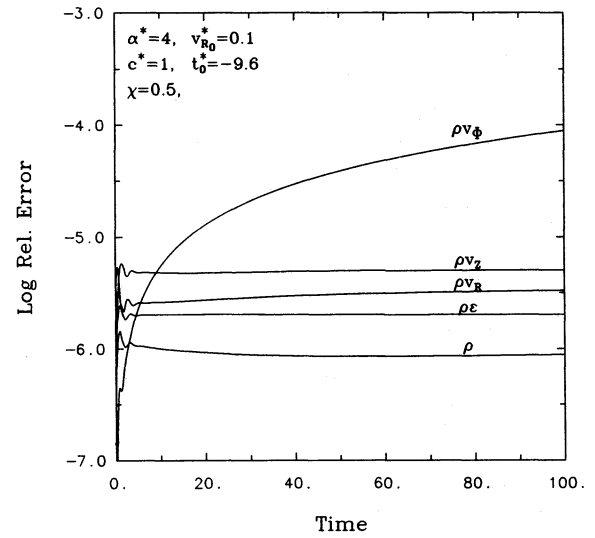

FIG. 30.—Logarithm of the relative error between our numerical results and the analytic prediction of Low (1985) as a function of time (in scaled units) for each of the five conserved quantities; namely, density, three components of momentum density, and energy density. Both models assume $\alpha^* = 4, c^* = 1$, and $\chi = 1$. (a) The compression phase with $v_{R_0}^* = -0.01$ and the point of maximum compression in the future at $t_0^* \approx 100$ is shown. (b) The expansion phase with $v_{R_0}^* = 0.1$ and the point of maximum compression in the past at $t_0^* = -9.6$ is shown. After initial transients, all errors are relatively constant with time except for ρv_ϕ in the expansion phase. See text for discussion.

other more simplified treatments, it still grows in time during the expansion phase. We believe it is because of the fact that the numerical solution is worse near the rotation axis. During the expansion phase, the inferior solution is then advected outward as the gas expands, thus causing the error to grow in time. Although our implementation is unsatisfactory from this point of view, it seems to be a general characteristic of the expansion phase. We have also learned from our experience with this problem that the results near the rotation axis are better if we consider the rotation equation in the form shown in equation (2.17), rather than a conservation of angular momentum form, even though the latter form does not have a source term. Given the difficulty of this problem, we believe it to be well suited for the testing of hydrodynamic codes. Even though our results are unsatisfactory for the expansion phase, we do not believe it to be an important issue with our wind solutions, since they have tended toward a stable equilibrium.

The second problem tests gravity and the stability of the code by asking it to calculate the structure of a gravitationally stratified, isothermal sphere. This is a rather simple but important test to verify that the method will behave correctly in near-static situations. That is, given the inherent nature of the Godunov method, it is vital to verify that a static object with density and pressure gradients (such as the gravitationally stratified ball) will not generate significant velocities. We find that the velocities generated are very subsonic and do not grow in time after the initial transients, provided we use a softening radius in the gravitational potential. The magnitude of the softening radius required depends upon the resolution. It is necessary that the softening radius be well resolved ($\gtrsim 8$ cells) to keep the velocities very subsonic (typically Mach numbers of less than 10^{-2}).

Finally, the third test is to start with an isothermal, constant-density ball with a large overpressure relative to the ambient medium and watch the evolution under the influence of gravity. The point of this exercise is twofold. First, one can watch the initial shock wave traveling out to see if it remains spherical. We found this to be true always. Second, a shock travels inward as the ball collapses due to the lack of pressure gradient support (ball is constant density and isothermal to start). This shock then rebounds when it hits the center. An important test is to see again if the rebounded shock still possesses spherical symmetry. We found this particular test to be particularly sensitive to the use of the softening radius in guaranteeing the sphericity of the rebounded shock. This is to be expected, since without a softening radius the emergence of the rebound shock is dominated by the results of one cell, which would tend to put a square on the rebounded shock.

None of the tests described above included any aspects of the heating and cooling. However, some simple observations can be made as to the accuracy of our incorporation of the heating and cooling terms from our model results. First of all, we find the final evolutionary state of the low corona to be very similar to the prescribed initial condition that the gas should be in thermal equilibrium. Second, tests utilizing the time step for energy advancement (which may be subcycled relative to the hydrodynamics) indicate that we are solving the equations accurately. That is, we have subdivided the energy time step by up to a factor of 10 relative to the hydrodynamic time step and found no discernible differences in either the overall structure or the mass flux density coming off the disk surface. Thus, we believe our solution procedure for including the energy source terms to be adequate.

REFERENCES

Antonucci, R. R. J., & Miller, J. S. 1985, ApJ, 297, 621
Balsara, D. S., & Krolik, J. H. 1993, ApJ, 402, 109
Band, D. L., Klein, R. I., Castor, J. I., & Nash, J. K. 1990, ApJ, 362, 90
Basko, M. M., Hatchett, S., McCray, R., & Sunyaev, R. A. 1977, ApJ, 215, 276
Basko, M. M., & Sunyaev, R. A. 1973, Ap&SS, 23, 117
Begelman, M. C., & McKee, C. F. 1983, ApJ, 271, 89
———. 1990, ApJ, 358, 392
Begelman, M. C., McKee, C. F., & Shields, G. A. 1983, ApJ, 271, 70 (BMS)
Berger, M., & Colella, P. 1989, J. Comput. Phys., 82, 64
Colella, P., & Glaz, H. M. 1985, J. Comput. Phys., 59, 264
Colella, P., & Woodward, P. R. 1984, J. Comput. Phys., 54, 174
Collin-Souffrin, S. 1987, A&A, 179, 60
Collin-Souffrin, S., & Dumont, A. M. 1990, A&A, 229, 292
Czerny, M., & King, A. R. 1989a, MNRAS, 236, 843
———. 1989b, MNRAS, 241, 839
Dumont, A. M., & Collin-Souffrin, S. 1990a, A&A, 229, 302
———. 1990b, A&A, 229, 313
Eggum, G. E., Coroniti, F. V., & Katz, J. I. 1987, ApJ, 323, 634
Ferland, G. J. 1991, OSU Internal Rep. 91-01
Fukue, J. 1989, PASP, 41, 123
Grevesse, N., & Anders, E. 1989, in AIP Conf. Proc. 183, Cosmic Abundances of Matter, ed. C. J. Waddington (New York: AIP), 1
Hubeny, I. 1990, ApJ, 351, 632
Kaisig, M. 1989a, A&A, 218, 89
———. 1989b, A&A, 218, 102
Kley, W. 1989, A&A, 208, 98
———. 1991, A&A, 247, 95
Kley, W., & Lin, D. N. C. 1992, ApJ, 397, 600
Klein, R. I., McKee, C. F., & Colella, P. 1990, in ASP Conf. Ser. 12, Evolution of the Interstellar Medium, ed. L. Blitz (San Francisco: ASP), 117
———. 1994, ApJ, 420, 213
Ko, Y., & Kallman, T. R. 1991, ApJ, 374, 721
Koyama, K., Inoue, H., Takano, S., Tanaka, Y., Ohashi, T., & Matsuoka, M. 1989, PASJ, 41, 731
Krolik, J. H., McKee, C. F., & Tarter, C. B. 1981, ApJ, 249, 422
London, R. A., & Flannery, B. P. 1982, ApJ, 258, 260

London, R., McCray, R., & Auer, L. H. 1981, ApJ, 243, 970
Low, B. C. 1985, ApJ, 293, 44
Marshall, F. E., et al. 1993, ApJ, 405, 168
Mathews, W. G., & Ferland, G. J. 1987, ApJ, 323, 456
McKee, C. F., & Begelman, M. C. 1990, ApJ, 358, 375
Melia, F., & Zylstra, G. J. 1992, ApJ, 398, L53
Melia, F., Zylstra, G. J., & Fryxell, B. 1991, ApJ, 377, L101
———. 1992, ApJ, 396, L27
Miller, J. S., & Goodrich, R. W. 1990, ApJ, 355, 456
Mobasher, B., & Raine, D. J. 1990, MNRAS, 244, 652
Murray, S. D., Castor, J. I., Klein, R. I., & McKee, C. F. 1994, ApJ, 435, 631
Murray, S. D., Woods, D. T., Castor, J. J., Klein, R. I., & McKee, C. F. 1995, ApJ, 454, L133
Nakagawa, Y., & Steinolfson, R. S. 1976, ApJ, 207, 296
Ostriker, E. C., McKee, C. F., & Klein, R. I. 1991, ApJ, 377, 593
Raymond, J. C. 1993, ApJ, 412, 267
Rybicki, G. B., & Lightman, A. P. 1979, Radiative Processes in Astrophysics (New York: Wiley)
Sawada, K., Matsuda, T., & Hachisu, I. 1986a, MNRAS, 219, 75
———. 1986b, MNRAS, 221, 679
Sawada, K., Matsuda, T., Inoue, M., & Hachisu, I. 1987, MNRAS, 224, 307
Shakura, N. I., & Sunyaev, R. A. 1973, A&A, 24, 337
Shaviv, G., & Wehrse, R. 1986, A&A, 159, L5
Shields, G. A., McKee, C. F., Lin, D. N. C., & Begelman, M. C. 1986, ApJ, 306, 90
Shimura, T., & Takahara, F. 1993, ApJ, 419, 78
Shlosman, I., & Vitello, P. 1993, ApJ, 409, 372
Strang, W. G. 1968, SIAM J. Numer Anal., 5, 506
Takahara, F., Rosner, R., & Kusunose, M. 1989, ApJ, 346, 122
Tavani, M., & London, R. 1993, ApJ, 410, 281
Tuchman, Y., Mineshige, S., & Wheeler, J. C. 1990, ApJ, 359, 164
Ueno, S., Mushotsky, R. F., Koyama, K., Iwasawa, Kl, Awakin, H., & Hayashi, I. 1994, PASJ, 46, L71
Van Leer, B. 1979, J. Comput. Phys., 32, 101
Vitello, P., & Shlosman, I. 1988, ApJ, 327, 680
———. 1993, ApJ, 410, 815
Vrtilek, S. D., Soker, N., & Raymond, J. C. 1993, ApJ, 404, 696